JETP Letters, Vol. 77, No. 10, 2003, pp. 537–540. Translated from Pis'ma v Zhurnal Éksperimental'noĭ i Teoreticheskoĭ Fiziki, Vol. 77, No. 10, 2003, pp. 639–643.
Original Russian Text Copyright © 2003 by Murzina, Kapra, Rassudov, Aktsipetrov, Nishimura, Uchida, Inoue.

Magnetization-Induced Third Harmonic Generation in Magnetophotonic Microcavities

T. V. Murzina[1, *], R. V. Kapra[1], A. A. Rassudov[1], O. A. Aktsipetrov[1], K. Nishimura[2], H. Uchida[2], and M. Inoue[2]

[1] *Moscow State University, Vorob'evy gory, Moscow, 119992 Russia*
**e-mail: mur@shg.ru*
[2] *Toyohashi University of Technology, 441-8580 Toyohashi, Japan*
Received April 16, 2003

Magnetization-induced third harmonic generation was experimentally observed in thin films of bismuth-doped yttrium-iron garnet. The magnitude of magnetization-induced nonlinear optical response was enhanced through building-in a garnet film into a photonic-crystal microcavity. It was shown that the observed magnetization-induced variations in the third-harmonic intensity were caused by the internal homodyne of interfering weak magnetic and strong nonmagnetic polarization components of the cubic nonlinearity of the garnet. © *2003 MAIK "Nauka/Interperiodica".*

PACS numbers: 78.20.Ls; 42.65.Ky; 42.70.Qs

The magnetization-induced nonlinear optical effects predicted in [1] were observed in second-harmonic (SH) generation from thin films of yttrium iron garnet ($Y_3Fe_5O_{12}$) doped with bismuth (Bi:YIG) [2]. More recently, the nonlinear analogues of the magnetooptical Faraday and Kerr effects were observed for the SH generation in various magnetic structures: magnetic superlattices [3], nanograin films possessing giant magnetoresistance [4], magnetic interfaces [5], etc. However, the weakness of the magnetization-induced effects in SH generation, which was observed, as a rule, in the experiments, foretold considerable difficulties in the experimental observation of higher order nonlinearity magnetization-induced effects, e.g., of third- harmonic (TH) generation. This is likely the reason why publications on the experimental observation of magnetization-induced TH generation are lacking [6].

In recent years, enhancement of optical and nonlinear-optical processes in photonic crystals and microcavities has become the subject of extensive experimental studies. For example, the light-localization-induced giant intensity enhancement of the second and third harmonics in mesoporous silicon microcavities was recently observed in [7]. This phenomenon gives promise that the magnetization-induced TH generation can be observed in magnetophotonic crystals and microcavities based on them, the technology of which has recently been developed [8]. For such structures, one might expect the enhancement of the magnitudes of nonlinear magnetooptical contributions as a result of strong light localization in the ferromagnetic layer of a microcavity. Such an enhancement was demonstrated for the Bi:YIG-based magnetic microcavities in the magnetization-induced SH generation in the geometry of the polar magnetooptical Kerr effect [9, 10]. The enhancement of the magnetization-induced nonlinear-optical signal magnitude does not imply an increase in the magnetic response contrast, because the nonmagnetic also increases. At the same time, an increase in the TH contrast must be observed due to the internal homodyne effect, which has recently been demonstrated for the magnetization-induced SH [11].

This work reports the observation of magnetization-induced optical third harmonic generation in a magnetic microcavity with a thin bismuth-doped yttrium–iron garnet film as a spacer.

Samples of magnetophotonic microcavities were 190-nm-thick half-wave layers (with an optical thickness $\lambda/2$) of polycrystalline Bi:YIG surrounded by pairs of Bragg reflectors, each composed, in turn, of five pairs of alternating quarter-wave SiO_2 and Ta_2O_5 layers with thicknesses of 135 and 95 nm, respectively. When manufacturing magnetic MC, a one-dimensional photonic crystal SiO_2/Ta_2O_5 was grown at a fused silica substrate by magnetron sputtering. It played the role of a distributed Bragg reflector. Then, a Bi:YIG film of the required optical thickness was deposited. After subsequent annealing at a temperature of 725°C for 10 min, a polycrystalline ferromagnetic garnet layer was formed. At the final stage of structure preparation, a cap photonic-crystal reflector was deposited on the MC garnet layer. The SEM image of a cleavage of the layered structure of magnetophotonic MC is shown in the inset in Fig. 1a.

Experiments on the magnetization-induced optical second and third harmonic generation were conducted using YAG:Nd^{3+} laser radiation with a wavelength of

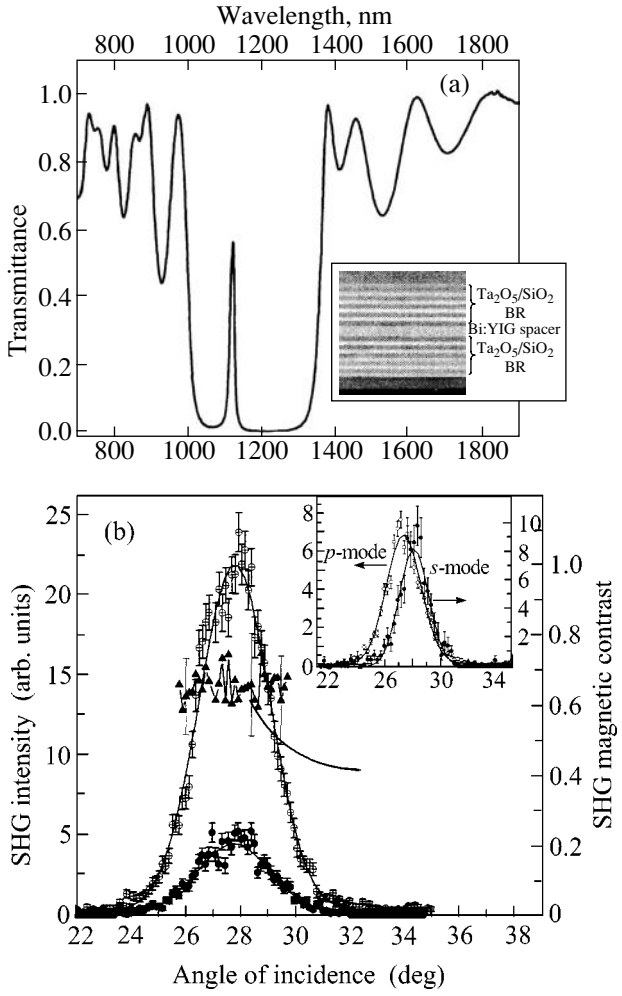

Fig. 1. (a) Linear transmission coefficient of the *p*-polarized fundamental wave at normal incidence; inset: SEM image of the magnetophotonic microcavity cleavage. (b) Angular spectra of the SH intensity for the *p–p* combination of the fundamental and SH waves, respectively, measured in the vicinity of the MC mode for the opposite directions of a magnetic field (circular symbols) and the spectra of magnetic TH contrast (triangular symbols). Inset: angular TH spectra for the *p–p* and *s–p* polarization combinations.

1064 nm, a pulse intensity of 10 MW/cm^2, a pulse duration of 15 ns, and a pulse repetition rate of 25 Hz. The SH and TH radiation reflected from the sample were separated from the fundamental radiation by glass and interference filters and detected by a photomultiplier and gated electronics. Part of the fundamental radiation was led to a reference channel, where the SH signal from the reference sample (quartz crystal) was detected. The normalization of the intensity measured in the signal channel to the signal intensity in the reference channel allowed the influence of laser-intensity fluctuations on the accuracy of the SH and TH intensities measured from the MC sample to be reduced. The polarization of fundamental radiation was varied using a half-wave plate and monitored, together with the SH polarization, by Glan prisms. For magnetic measurements, the sample was placed in a saturating static magnetic field with a strength of ≃2 kOe produced by permanent magnets in the geometry of the transverse magnetic Kerr effect. When measuring the angular spectra of SH and TH intensities, the sample was mounted on a computer-controlled automated goniometer with an angular resolution of 0.24°.

The transmission spectrum of a magnetic MC at normal incidence is shown in Fig. 1a. It demonstrates the presence of a photonic band gap in the wavelength range from 1000 to 1340 nm, as follows from the almost total absence of the transmitted light (i.e., its total reflection) in this range, and an MC mode centered at $\lambda \simeq 1117$ nm.

For this sample, the quadratic nonmagnetic and magnetic nonlinear-optical properties were primarily characterized by the SH generation method.

For the in-plane isotropic nonlinear film, the following components of quadratic susceptibility are nonzero in the absence of an external magnetic field: $\chi^{(2)}_{zzz}$, $\chi^{(2)}_{zxx} = \chi^{(2)}_{zyy}$, and $\chi^{(2)}_{xxz} = \chi^{(2)}_{yyz}$. The coordinate system is chosen in such a way that the *z* axis is directed along the normal to the sample plane and the *x* axis lies in the sample plane and in the incidence plane. In this case, the SH generation is allowed only for the *p–p* and *s–p* combinations of the fundamental and SH waves, respectively. The corresponding experimentally measured angular SH spectra are presented in the inset in Fig. 1. One can see that the angular positions of the nonmagnetic *p–p* and *s–p* SHs are different, which correlates with the presence of two modes for the *p* and *s* pumping in the frequency spectra of the linear reflection coefficient [9, 10]. The spectral (angular or frequency) distinction between the positions of the *p* and *s* modes can be caused by both the polarization splitting [12] and the uniaxial anisotropy of the ferrite garnet layer in the normal direction to the sample. Such an anisotropy can be induced during the course of sample preparation as a result of the deformation of the ferrite garnet layer, which is clamped between the dielectric Bragg reflectors [10].

The angular positions of the SH maxima correspond to the angles of incidence for which the condition for exciting the MC mode by the fundamental radiation with a wavelength of 1064 nm is achieved. Using the expression $\lambda = \lambda_0\sqrt{1 - \sin^2\alpha/n^2(\omega)}$ for the wavelength resonant with MC at a nonzero incidence angle, where λ_0 is the resonant wavelength at the normal incidence on the sample, α is the angle of incidence, and *n* is the refractive index, one can determine the value of the latter at the fundamental wavelength: $n_{1064} = 1.554$.

For a sample placed in a magnetic field in the geometry of the transverse magnetooptical Kerr effect (along the *Y* axis), additional *M*-odd (*M* is the magnetization)

quadratic susceptibility components appear: $\chi^{(2),M}_{xyyY}$, $\chi^{(2),M}_{xxxY}$, $\chi^{(2),M}_{yyxY}$, $\chi^{(2),M}_{xzzY}$, and $\chi^{(2),M}_{zzxY}$, where the fourth index indicates the orientation of a magnetic field (magnetization) in the laboratory coordinate system. In the case where the nonmagnetic and *M*-odd magnetic contributions to the nonlinear polarization interfere, one can also observe the *M*-odd effects in the SH intensity.

The SH angular spectra of magnetic MC, as measured for the *p*-polarized SH and fundamental radiations and for the opposite directions of a magnetic field in the geometry of the transverse Kerr effect, are shown in Fig. 1b. One can see from this figure that the magnetic field induces an appreciable *M*-odd change in the SH intensity, whereas the angular position of the SH maximum remains virtually unshifted. The magnetic contrast $\varrho_{2\omega} = (I_{2\omega}(\uparrow) - I_{2\omega}(\downarrow))/(I_{2\omega}(\uparrow) + I_{2\omega}(\downarrow))$ serves as a measure of the magnetization-induced change in the intensity of reflected SH, where $I_{2\omega}(\uparrow)$ and $I_{2\omega}(\downarrow)$ are the SH intensities measured for the opposite magnetic-field directions. The angular spectrum of magnetic contrast at the SH wavelength in the MC mode is also shown in Fig. 1b. It is seen that, within the measurement error, the magnetic contrast is spectrally independent and equal to ≈0.6.

We now turn to the TH generation in magnetic MCs. Symmetry analysis of the cubic dipole susceptibility tensor responsible for the optical third harmonic generation shows that, in the absence of a magnetic field, the following components are nonzero for a nonlinear medium that is isotropic in the layer plane:

$$\chi^{(3)}_{zzzz}, \chi^{(3)}_{xxxx} = \chi^{(3)}_{yyyy}, \chi^{(3)}_{zzxx} = \chi^{(3)}_{zzyy},$$
$$\chi^{(3)}_{xxyy} = \chi^{(3)}_{yyxx}, \chi^{(3)}_{xxzz} = \chi^{(3)}_{yyzz}. \quad (1)$$

It follows from the form of nonlinear susceptibility components that the nonmagnetic TH generation is possible only for the *s*–*s* and *p*–*p* combinations of the fundamental and TH waves, respectively. The corresponding experimentally measured TH angular spectra are shown in Fig. 2b. As in the case of SH generation, the angular spectra of the TH *s* and *p* modes were shifted by 1.5°–2° relative to each other.

The dependence of the TH intensity on the fundamental radiation intensity is shown in the inset in Fig. 2a. The logarithm of TH intensity linearly depends on the logarithm of fundamental intensity, with the slope being equal to three. This cubic dependence confirms that the experimentally detected signal belongs to the third harmonic.

As in the case of SH, a magnetic field induces the appearance of magnetization-odd components of cubic dipole susceptibility. One can show that the following components appear in the geometry of the transverse

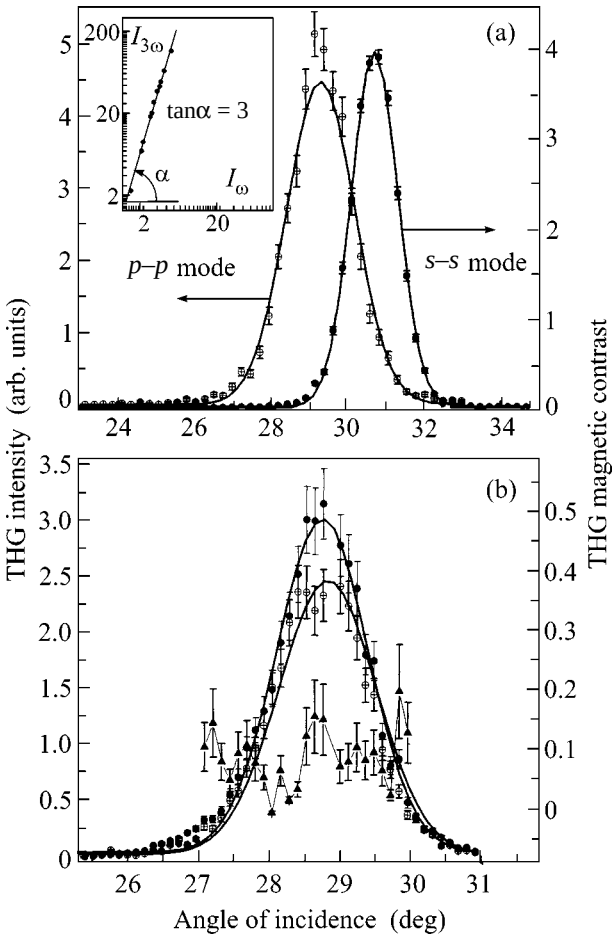

Fig. 2. (a) Angular TH spectra for the *p*–*p* and *s*–*s* combinations of fundamental and TH wave polarizations (open and dark circles, respectively). Inset: TH intensity as a function of pump intensity (log–log scale). (b) Angular spectra of *p*-polarized TH for oppositely directed magnetic fields in the geometry of the meridional Kerr effect (circles) and the TH magnetic contrast (triangles). The polarization of fundamental radiation makes an angle of 7° with the *s* polarization.

(longitudinal) Kerr effect in a magnetic field parallel to the *Y*(*X*) axis:

M ∥ *Y*:

$$\chi^{(3),M}_{zxzzY}, \chi^{(3),M}_{xxxzY}, \chi^{(3),M}_{zxxxY}, \chi^{(3),M}_{yyxxY}, \chi^{(3),M}_{xzzzY}, \quad (2)$$

M ∥ *X*:

$$\chi^{(3),M}_{zyyyX}, \chi^{(3),M}_{yxxzX}, \chi^{(3),M}_{yzzzX}, \quad (3)$$

where the fifth index indicates the orientation of a magnetic field (magnetization) in the sample.

The magnetization-odd intensity variations in TH generation are possible if the nonmagnetic and *M*-odd magnetic components of the cubic nonlinear polarization interfere, thereby causing the internal homodyne effect that was previously studied for magnetization-induced SH generation in [11, 13]. It follows from the

form of the above *M*-odd cubic susceptibility components that such a situation occurs only for the *p*–*p* combination of polarizations in the geometry of the transverse magnetooptical Kerr effect. However, the *M*-odd effect was not experimentally observed in the TH generation, most likely because of a comparatively low magnetic cubic susceptibility.

The following experimental scheme was chosen for recording the magnetization-induced TH component: the pump polarization was turned by 5°–7° from *s*, and the *p*-polarized TH component was recorded. Under these conditions, almost the entire magnetic TH *s*–*p* component $\chi^{(3),M}_{zyyyX}$, which interfered with a strongly suppressed nonmagnetic TH *p*–*p* component, was recorded. The TH magnetic contrast was also measured for the *s*-polarized TH component, and the pump polarization shifted from *p* by an angle of ≃7°. Similar to the magnetization-induced SH generation, the TH magnetic contrast was determined by the expression $\rho_{3\omega} = (I_{3\omega}(\uparrow) - I_{3\omega}(\downarrow))/(I_{3\omega}(\uparrow) + I_{3\omega}(\downarrow))$, where $I_{3\omega}(\uparrow)$ and $I_{3\omega}(\downarrow)$ are the TH intensities for the oppositely directed magnetic fields. The resulting value of the TH magnetic contrast $\rho_{3\omega}$ was found to be ≃0.1 for the incidence angles corresponding to the MC-mode center and for a shift of ±1°.

The observed TH magnetic contrast can be caused by two factors. First, it can be due to TH generation by the magnetization-induced cubic susceptibility components and by the internal homodyne effect, which consists in the revelation of a weak TH magnetic component on the background of a much stronger nonmagnetic TH interfering with the former [11, 13]. In this case, $\chi^{(3),M}$ can be estimated at $\sim 2 \times 10^{-4}\chi^{(3)}$, where $\chi^{(3)}$ is the effective nonmagnetic cubic susceptibility for the *p*–*p* combination. Second, the magnetization-induced effect may reveal itself in the TH intensity because of a change in the polarization of the fundamental radiation as a result of a Faraday rotation in the ferromagnetic MC layer. The latter contribution is, presumably, small, because the Faraday rotation of infrared fundamental radiation with a wavelength of 1064 nm is less than 1° even for the MC-enhanced linear Faraday effect [7].

In summary, magnetization-induced optical TH generation has been experimentally observed in magnetophotonic yttrium–iron garnet microcavities. It has been shown that the magnetization-induced change in the TH intensity is primarily due to the odd contribution from the magnetic cubic susceptibility, as becomes clear from the interference with the nonmagnetic contribution from the internal homodyne effect.

This work was supported by the Russian Foundation for Basic Research (project nos. 01-02-16746, 01-02-17524, 01-02-04018, 00-02-16253) and the President grant "Leading Scientific Russian Schools" (no. 00-15-96555).

REFERENCES

1. N. N. Akhmediev, S. B. Borisov, A. K. Zvezdin, *et al.*, Fiz. Tverd. Tela (Leningrad) **27**, 1075 (1985) [Sov. Phys. Solid State **27**, 650 (1985)].
2. O. A. Aktsipetrov, O. V. Braginskii, and D. A. Esikov, Kvantovaya Élektron. (Moscow) **17**, 320 (1990) [Sov. J. Quantum Electron. **20**, 259 (1990)].
3. Th. Rasing, J. Magn. Magn. Mater. **165**, 35 (1997).
4. T. V. Murzina, T. V. Misuryaev, A. F. Kravets, *et al.*, Surf. Sci. **482–485**, 1101 (2001).
5. J. Reif, J. C. Zink, C.-M. Schneider, and J. Kirschner, Phys. Rev. Lett. **67**, 2878 (1991).
6. Results on magnetization-induced effects in third-harmonic generation in thin garnet films were presented recently by Dr. Shin-ichi Ohkoshi from The University of Tokyo on Conference on Magnetics at Tokyo University of Agriculture and Technology.
7. T. V. Dolgova, A. I. Maidykovski, M. G. Martemyanov, *et al.*, Appl. Phys. Lett. **81**, 2725 (2002); T. V. Dolgova, A. I. Maidikovsky, M. G. Martemyanov, *et al.*, Pis'ma Zh. Éksp. Teor. Fiz. **75**, 17 (2002) [JETP Lett. **75**, 15 (2002)].
8. M. Inoue, K. Arai, T. Fujii, and M. Abe, J. Appl. Phys. **83**, 6768 (1998); M. Inoue, K. Arai, T. Fujii, and M. Abe, J. Appl. Phys. **85**, 5768 (1999).
9. A. A. Fedyanin, T. Yoshida, K. Nishimura, *et al.*, Pis'ma Zh. Éksp. Teor. Fiz. **76**, 609 (2002) [JETP Lett. **76**, 527 (2002)].
10. A. A. Fedyanin, T. Yoshida, K. Nishimura, *et al.*, J. Magn. Magn. Mater. **258–259**, 96 (2003).
11. T. V. Murzina, A. A. Fedyanin, T. V. Misuryaev, *et al.*, Appl. Phys. B **68**, 537 (1999).
12. D. Bachter, M. S. Skolnik, A. Armitage, *et al.*, Phys. Rev. B **56**, 10032 (1997).
13. O. A. Aktsipetrov, Colloids Surf. A **202**, 165 (2002).

Translated by V. Sakun

JETP Letters, Vol. 77, No. 10, 2003, pp. 541–545. From Pis'ma v Zhurnal Éksperimental'noĭ i Teoreticheskoĭ Fiziki, Vol. 77, No. 10, 2003, pp. 644–648.
Original English Text Copyright © 2003 by Mamun, Shukla, Bingham.

Dust-Alfvén Mach Cones in Saturn's Dense Rings¶

A. A. Mamun*, [1], P. K. Shukla*, [2], and R. Bingham, [3]**

** Institut für Theoretische Physik IV, Rubr-Universität Bochum, D-44780 Bochum, Germany*

*** Ratherford Appleton Laboratory, Chilton, Didcot, Oxfordshire, OX 11 OQX, England*

Received March 20, 2003

The formation of Mach cones associated with long-wavelength dust-Alfvén waves in Saturn's dense rings has been theoretically investigated. It is explicitly shown that for typical dusty plasma parameters corresponding to Saturn's dense rings, Mach cones are only formed by dust-Alfvén waves, which are found to be more prominent than any other longitudinal waves (e.g., long-wavelength dust-acoustic waves). The characteristics of the dust-Alfvén Mach cones that are found to be formed in Saturn's dense rings are also presented. The dusty plasma model, dust-Alfvén waves, and dust-Alfvén Mach cones that we predict in our present letter are expected to be observed in Saturn's dense rings by the imaging and occultation experiments on board the NASA/ESA space mission CASSINI, arriving at Saturn in 2004. © *2003 MAIK "Nauka/Interperiodica".*

PACS numbers: 96.30.Mh; 52.27.Lw; 52.35.Bj

It is well known that an object moving with a supersonic speed in a dispersive medium creates a pressure disturbance that is not felt upstream from the object. The cone that confines the disturbance is called a Mach cone. The latter is well known in gas dynamics. They are produced, for example, by bullets and supersonic jet planes. If the perturbing object moves straight at a constant velocity U, it creates expanding waves that are circular in two-dimensions and spherical in three dimensions. The superposition of these waves forms a cone. The Mach cone opening angle θ, defined as a semivertex angle of the cone, is determined by the geometry as $\theta = \sin^{-1}(1/M)$, where $M = U/C_s$ is the Mach number of the supersonic object and C_s is the acoustic (sound) speed in the undisturbed medium.

Mach cones are also known to occur in gas dynamics [1, 2], solid matter [3], and in some crystals [4, 5]. In an elastic medium surrounding a fluid-filled borehole, spontaneously launched surface waves propagating along the fluid-solid boundary excite P and S waves propagating into the bulk solid. The interference between P and S waves forms Mach cones. The wavefront of the surface wave acts as the supersonic object, since its speed is typically higher than the P and S waves.

Ship waves have an appearance similar to Mach cones. The latter are also known as the "Kelvin wedge" that forms behind a ship in deep water. Here a moving pointlike disturbance generates either gravity or capillary waves on the fluid surface. These deep-water strongly dispersive surface waves [6] are responsible for multiple Mach cone structures.

Besides the above-mentioned Mach cones on human scales, Mach cones also occur on astronomical scales (e.g., the Earth's magnetotail formed by interaction with the solar wind) and microscopic scales (e.g., Cherenkov radiation created by rapidly moving elementary charge). Havnes *et al.* [7, 8] theoretically predicted the existence of super dust-acoustic Mach cones associated with dust-acoustic waves [9] of an unmagnetized dusty plasma, which are claimed to be relevant to Saturn's rings. Dubin [10] developed a linear theory for the phonon wake produced by a charge moving relative to a crystalline lattice in an unmagnetized plasma containing strongly coupled dust grains. The theory predicts multiple Mach cones due to constructive interference of strongly dispersive compressional phonons. However, Dubin's theory cannot be applied to Saturn's magnetized plasmas with weakly correlated dust grains. In Saturn's rings, we may have Mach cones associated with numerous dispersive plasma waves that are affected by the ambient magnetic field. For example, we may have obliquely propagating intermediate-frequency ($\omega_{cd} \ll \omega \ll \omega_{ci}$, $k_z v_{te}$, where ω_{cd} and ω_{ci} are the dust and ion gyrofrequencies, respectively, k_z is the component of the wave vector $\mathbf{k}$ along the external magnetic field $\hat{\mathbf{z}} B_0$, and v_{te} is the electron thermal speed) long-wavelength (in comparison with the electron Debye radius λ_{De} and the ion gyroradius ρ_s, at the electron temperature) dust-acoustic waves [11] whose phase speed for $k_z\lambda_{De} \ll \omega_{pd}/\omega_{pi}$ is $C_{De}/(1 + k_\perp^2\rho_s^2)^{1/2}$, where $C_{De} = \lambda_{De}\omega_{pd}$, $\rho_s = \lambda_{De}\omega_{pi}/\omega_{ci}$, ω_{pd} (ω_{pi} is the dust

¶ This article was submitted by the authors in English.

[1] Permanent address: Department of Physics, Jahangirnagar University, Savar, Dhaka, Bangladesh.

[2] Also at the Department of Plasma Physics, Umeå University, SE-90187 Umeå, Sweden.

[3] Also at the Department of Physics and Applied Physics, University of Strathclyde, Glasgow, G4 ONG, Scotland.

(ion) plasma frequency, and $k_\perp$ is the component of $\mathbf{k}$ across $\hat{\mathbf{z}}$. Here, the electrons rapidly thermalize along the magnetic field direction and follow a Boltzmann distribution, while the density distributions of magnetized ions (unmagnetized dust grains) are affected (unaffected) by the external magnetic field. Furthermore, in the opposite limit, viz. $k_z\lambda_{De} \gg \omega_{pd}/\omega_{pi}$, the dust grains can be considered stationary, and the corresponding parallel (to $\hat{\mathbf{z}}$) phase speed of the dust ion-acoustic wave (DIAW) is $C_I = \lambda_{De}\omega_{pi}/(1 + k_\perp^2\rho_s^2)^{1/2}$, indicating that the DIA waves are nondispersive along the magnetic field direction. The high-phase speed DIA waves would not participate in the Mach cone formation, as they propagate much faster than a dust boulder, whose speed is given by Eq. (3). On the other hand, in the short-wavelength (in comparison with the ion gyroradius ρ_i) dust-acoustic fields, the ions follow a straight-line orbit across $\hat{\mathbf{z}}$ and establish a Boltzmann density distribution in the wave potential. Taking a Boltzmann electron density distribution and inertial dust, one then obtains the dust-acoustic wave (DAW) whose phase speed is $C_D = \lambda_D\omega_{pd}/(1 + k^2\lambda_D^2)^{1/2}$, where $\lambda_D = \lambda_{De}\lambda_{Di}/(\lambda_{De}^2 + \lambda_{Di}^2)^{1/2}$ and λ_{Di} is the ion Debye radius. As usual, for $n_iT_e \gg n_eT_i$, the dust-acoustic phase speed is [11, 12] $C_d = (Z_d^2 n_d T_i/n_i m_d)^{1/2}$, where $n_i(n_d)$ is the ion (dust) number density, $T_e(T_i)$ the electron (ion) temperature, and Z_d is the number of electrons residing on the dust grain surface. For typical plasma parameters corresponding to Saturn's rings [11, 13–16], viz. $B_0 \simeq 0.2$ G, $T_i = 10$ eV, $n_d \simeq 10$ cm^{-3}, $Z_d \simeq 10^3$, $r_d \simeq 0.25$ μm, where r_d is the dust particle radius, one finds that $C_d^2/V_A^2 \simeq 5 \times 10^{-5}$, where $V_A = B_0/\sqrt{4\pi\rho_d}$ is the dust-Alfvén speed, $\rho_d = n_d m_d$ is the dust mass density, and m_d is the mass of micron-sized dust particles. This means that in Saturn's rings the dust-magnetoacoustic wave propagation [17] is more prominent than the long-wavelength dust-acoustic wave propagation, and the waves involving perturbation of magnetic fields are likely to participate in the formation of Mach cones. Accordingly, in this letter we have taken into account the dynamics of both the ion and dust species in the ambient Saturn's magnetic field and study the dust-hydromagnetic waves and associated Mach cones in Saturn's dense rings. We have predicted here that the perturbation/acoustic waves that may exist in Saturn's rings are not long-wavelength dust-acoustic but dust-magnetoacoustic, in which the magnetic pressure $B_0^2/4\pi$ gives rise to the restoring force and the dust mass density $n_d m_d$ provides the inertia. Therefore, in Saturn's dense rings, if Mach cones are formed, they are formed by dust-magnetoacoustic waves but, of course, not by the long-wavelength dust-acoustic waves.

We consider a negatively charged dust particle of mass m_d and charge-$Z_d e$ moving in a field that includes Keplerian gravity and a corotating planetary magnetic field (taken to be aligned centered dipole) with concomitant induced electric field [13–16, 18]. We first consider single particle dynamics and neglect the radiation pressure, plasma drag, planetary oblateness, charge fluctuations, and collective effects. The dynamics of such a negatively charged dust particle is governed by the combined gravitational, magnetic, and electric forces. The orbital angular velocity ω_d of the negatively charged dust particle can, therefore, be expressed as [13, 16]

$$\omega_d = \frac{1}{2r^3}\left[-\omega_{cd} \pm \sqrt{\omega_{cd}^2 + 4r^3(\Omega_k^2 + \omega_{cd}\Omega_p)}\right], \quad (1)$$

where r is the dust particle position normalized by the planet radius R_p, $\omega_{cd} = Z_d e B_0/m_d c$ and $\Omega_k = (GM_p/R_p^3)^{1/2}$ are the dust cyclotron and Kepler frequencies both evaluated at a point on the planetary equator, Ω_p is planetary spin rate, M_p is the planet mass, G is the universal gravitational constant, and n is the speed of light in vacuum. We note that in deriving (1) the planetary magnetic field $\mathbf{B}_p$ is assumed to be dipolar with the dipole strength $\mathbf{M} = \mathbf{B}_0 R_p^3$ (where $\mathbf{B}_0$ is the magnetic field strength on the planetary equator), which is appropriate for Saturn and Jupiter. The + (–) sign in (1) represents the prograde (retrograde) motion of the dust particle.

A large boulder and a small dust particle will, therefore, move at different velocities. The difference in velocities V_d is given by

$$V_d = rR_p(\omega_d - r^{-3/2}\Omega_k). \quad (2)$$

To approximate V_d, let us consider a dust particle in Saturn's rings where [7, 13, 14, 16, 18] $R_p = 60300$ km, $M_p = 5.688 \times 10^{26}$ kg, $\Omega_p = 1.691 \times 10^{-4}$ rad/s, $r = 7$, $B_0 \simeq 0.2$ G, $Z_d \simeq 10^3$, $r_d \simeq 0.25$ μm, so that $\Omega_k = 4.16 \times 10^{-4}$ rad/s and $\omega_{cd} \simeq 4.89 \times 10^{-5}$ rad/s. So for a particle in Saturn's rings, we can safely take the approximations $\omega_{cd} \ll \Omega_k$, $\Omega_p \leq \Omega_k$, and $r \geq 1$, which allow us to approximate (2) as

$$V_d \simeq \frac{R_p\omega_{cd}}{2r^2}\left(\frac{\Omega_p}{\Omega_k} - 1\right). \quad (3)$$

To study the perturbation of the medium, we consider a two-component magnetized dusty plasma composed of negatively charged dust grains and positively charged ions. We assume that the electron number density is highly depleted due to the attachment of almost all the electrons to the surface of highly charged and extremely massive dust grains. The dust-ion plasma system is assumed to be immersed in a homogeneous magnetic field $\hat{\mathbf{z}}B_0$. This model is quite appropriate for

Saturn's rings (e.g., Saturn's F-ring [11, 13–15, 19). We consider a small-amplitude long-wavelength (in comparison with ρ_i) perturbation in such a dust-ion plasma, which may be described by the two linearized coupled equations

$$\frac{\partial^2 \mathbf{u}_d}{\partial t^2} + \frac{V_A^2}{\omega_{ci}} \nabla \times \frac{\partial^2 \mathbf{B}}{\partial t^2} - V_A^2 \left(\nabla \times \frac{\partial \mathbf{B}}{\partial t} \right) \times \hat{\mathbf{z}} - C_d^2 \nabla (\nabla \cdot \mathbf{u}_d) = 0, \quad (4)$$

and

$$\frac{\partial \mathbf{B}}{\partial t} + \hat{\mathbf{z}} (\nabla \cdot \mathbf{u}_d) - (\hat{\mathbf{z}} \cdot \nabla) \mathbf{u}_d - \frac{1}{\omega_{cd}} \nabla \times \frac{\partial \mathbf{u}_d}{\partial t} = 0, \quad (5)$$

where $\mathbf{u}_d$ is the dust fluid velocity, $\mathbf{B}$ is the wave magnetic field normalized to B_0, $\omega_{ci} = eB_0/m_i c$ is the ion gyrofrequency, and m_i is the ion mass. We now assume that the perturbation mode propagates in the x–z plane, i.e., $\mathbf{B}$ and $\mathbf{u}_d$ are proportional to $\exp[-i\omega t + i(k_x x + k_z z)]$. Therefore, using (4) and (5), we obtain

$$\begin{pmatrix} D_{xx} & D_{xy} & D_{xz} \\ D_{yx} & D_{yy} & D_{yz} \\ D_{zx} & D_{zy} & D_{zz} \end{pmatrix} \begin{pmatrix} B_x \\ B_y \\ B_z \end{pmatrix} = 0, \quad (6)$$

where

$$D_{xx,zz} = (1 + k_{z,x}^2 \lambda_i^2)\omega - \frac{k_{z,x}^2 V_A^2 (\omega^2 - k_z^2 C_d^2)}{\omega(\omega^2 - k^2 C_d^2)},$$

$$D_{xy} = -D_{yx} = -ik_z^2 V_A^2 \left(\frac{1}{\omega_{cd}} - \frac{1}{\omega_{ci}} \right),$$

$$D_{xz} = D_{zx} = -\omega k_z k_x \lambda_i^2 + \frac{k_z k_x V_A^2 (\omega^2 - k_z^2 C_d^2)}{\omega(\omega^2 - k^2 C_d^2)}, \quad (7)$$

$$D_{yy} = (1 + k^2 \lambda_i^2)\omega - \frac{k_z^2 V_A^2}{\omega},$$

$$D_{yz} = -D_{zy} = -ik_z k_x V_A^2 \left(\frac{1}{\omega_{cd}} - \frac{1}{\omega_{ci}} \right).$$

Here, $\lambda_i = c/\omega_{pi}$ is the ion skin depth. We note that the origin of the dispersive effect involving the $k\lambda_i$ term is attributed to the ion inertial effect, which breaks the frozen-in-field condition.

We are interested in extremely low-frequency obliquely propagating dust-hydromagnetic waves for which $\omega \ll \omega_{cd}$ are valid. Using these approximations, we obtain from (6) three types of obliquely propagating dust-hydromagnetic waves. These are

$$\frac{\omega}{k} = \frac{V_A \cos\delta}{\sqrt{1 + k^2 \lambda_i^2}}, \quad (8)$$

and

$$\frac{\omega}{k} = \frac{1}{\sqrt{2}} \left[\frac{V_A^2}{1 + k^2 \lambda_i^2} + C_d^2 \pm \sqrt{\left(\frac{V_A^2}{1 + k^2 \lambda_i^2} + C_d^2 \right)^2 - \frac{4 V_A^2 C_d^2 \cos^2\delta}{1 + k^2 \lambda_i^2}} \right]^{1/2}, \quad (9)$$

where δ is the angle between the directions of the ambient magnetic field and the wave propagation. Equation (8) represents the dispersion relation for the shear dust-Alfvén waves modified by the effect of the ion-skin depth, which decreases their phase speed by the factor $\sqrt{1 + k^2 \lambda_i^2}$. On the other hand, (9) with the + (–) sign represents the dispersion relation for the fast (slow) dust-hydromagnetic waves modified by the effect of the ion-skin depth and obliqueness. For typical plasma parameters corresponding to Saturn's rings [11, 13–16], we find that $C_d^2/V_A^2 \simeq 5 \times 10^{-5}$. This means that in Saturn's rings the dust-Alfvén wave propagation is much more prominent than the long-wavelength dust-acoustic wave propagation, and therefore the consideration of the long-wavelength dust-acoustic wave propagation and associated Mach cones in Saturn's rings is not realistic. We are, therefore, interested in examining the formation as well as detecting the characteristics of Mach cones associated with the dust-hydromagnetic waves defined by (8) and (9).

As we explained physically in the introduction, Mach cones associated with the waves defined by (8) and (9) will be formed if the dust particle speed V_d is larger than the wave phase speed $V_p = \omega/k$, i.e., if $V_d/V_p > 1$. If this condition is satisfied, the Mach cone opening angle θ is given by

$$\theta = \sin^{-1} \left(\frac{V_p}{V_d} \right), \quad (10)$$

where V_d is given by (2) and $V_p = \omega/k$ is given by (8) for shear dust-Alfvén waves, and by (9) for fast and slow dust-magnetosonic waves. We have numerically analyzed V_d/V_p for typical plasma parameters corresponding to Saturn's rings [11, 13–16], given in the figure caption, and have shown that Mach cones are formed by the shear dust-Alfvén waves of wavelength ~7 km or less (cf. lower plot) and by slow dust-magnetosonic waves of any wavelength [without the upper bound on the wavelength (cf. upper plot)]. We have also found that the upper bound on the wavelength of both the shear dust-Alfvén and slow dust-magnetosonic waves by which Mach cones are formed increases as we increase their propagation angle δ (cf. lower and upper plots). We note here that, for parameters corresponding

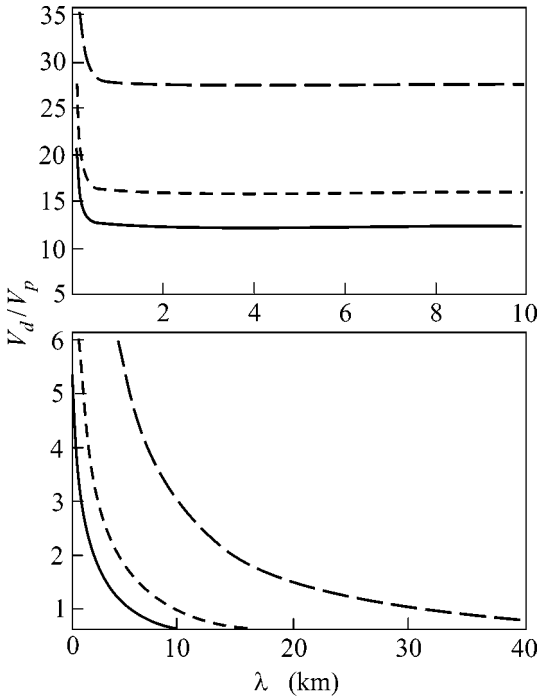

The wavelength regimes of shear dust-Alfvén (lower plot) and of slow dust-magnetosonic (upper plot) waves propagating with different angle δ for which Mach cones are formed in Saturn's dense rings ($B_0 = 0.2$ G, $T_i = 10$ eV, $n_d = 10$ cm^{-3}, $Z_d = 10^3$, $r = 7$, $r_d = 0.25$ μm). The solid, dotted, and dashed curves are for δ = 85°, δ = 87°, and δ = 89° in both the plots.

to Saturn's rings, Mach cones are not formed by fast dust-magnetosonic waves.

It is obvious from the figure and Eq. (9) that the Mach cone opening angle θ decreases with increasing propagation angle δ in the case of shear dust-Alfvén waves. We have also estimated the Mach cone opening angle θ (that may be formed in Saturn's dense rings) associated with shear dust-Alfvén and slow dust-magnetosonic waves of wavelength 5 km, propagating with an angle δ = 85°. These are ~30° and ~4°, respectively. Physically, Mach cones arise due to the constructive interference of dispersive dust-hydromagnetic waves in dust-ion plasmas of Saturn's dense rings. We expect that the NASA/ESA space probe CASSINI can make direct observations of the dust-hydromagnetic modes and associated Mach cones that we have reported in this letter. From the opening angle of the dust-Alfvénic Mach cones, one can then deduce the dust and ion mass densities, as well as dust charge and the optical depth of Saturn's dense rings. Although the present investigation provides the parameter regimes for the existence of the dust-Alfvénic Mach cones, the fine structure of a dust magnetoacoustic wake behind a dust boulder can be obtained by numerically solving the dust magnetoacoustic wave equation with an appropriate source. This investigation can be carried out along the lines of Brattli *et al.* [8].

In closing, we mention that although the formation of Mach cones in a magnetized dusty plasma of Saturn's rings is attributed to constructive interference between linear dispersive dust magnetohydrodynamic waves, nonlinear and dissipative effects can appear when the wave amplitudes are large and dust charge perturbations are taken into consideration. A delicate balance between nonlinearity and dissipation can produce magnetoacoustic shock waves, similar to those studied by Popel *et al.* [20, 21] for an unmagnetized dusty plasma. However, a detailed investigation of the dust grain charging in a magnetized dusty plasma containing large amplitude dust hydromagnetic waves is quite involved and is beyond the scope of the present work. We anticipate that dust charge perturbation effects might be insignificant, since the dust grain charging time is typically much shorter than the timescale on which the dust magnetoacoustic perturbations develop.

A.A. Mamun gratefully acknowledges the financial support of the Alexander von Humboldt-Stiftung (Bonn, Germany). This work was partially supported by the Deutsche Forschungsgemeinschaft, sonder-forschungsbereich 591, as well as by the European Commission, contract nos. HPRN-CT-2000-00140 and HPRN-CT-2001-00314.

REFERENCES

1. H. W. Liepman and A. Roshko, *Elements of Gas Dynamics* (Wiley, New York, 1957).
2. J. Bond, K. Watson, and J. Welch, *Atomic Theory of Gas Dynamics* (Addison-Wesley, Reading, MA, 1965).
3. N. Cheng, Z. Zhu, C. Cheng, and M. Toksöz, Geophys. Prospect. **42**, 303 (1994).
4. P. Gumbsch and H. Gao, Science **283**, 965 (1999).
5. D. Samsonov, J. Gorce, Z. W. Ma, *et al.*, Phys. Rev. Lett. **83**, 3649 (1999).
6. G. Crapper, *Introduction to Water Waves* (Horwood, Chichester, 1984).
7. O. Havnes, T. Aslaksen, T. W. Hartquist, *et al.*, J. Geophys. Res. **100**, 1731 (1995); O. Havnes *et al.*, Planet. Space Sci. **49**, 223 (2001).
8. O. Havnes, F. Li, M. Melandso, *et al.*, J. Vac. Sci. Technol. A **14**, 525 (1996); A. Brattli, O. Havnes, and F. Melandsø, Phys. Plasmas **9**, 958 (2002).
9. N. N. Rao, P. K. Shukla, and M. Y. Yu, Planet. Space Sci. **38**, 543 (1990); P. K. Shukla, Phys. Plasmas **8**, 1791 (2001).
10. D. E. Dubin, Phys. Plasmas **7**, 3895 (2000).
11. P. K. Shukla and A. A. Mamun, *Introduction to Dusty Plasma Physics* (Inst. of Physics, Bristol, 2002).

12. V. E. Fortov, in *Dusty Plasmas in the New Millennium: Third International Conference on the Physics of Dusty Plasmas*, Ed. by R. Bharuthram *et al.* (AIP, Melvill, N.Y., 2002), pp. 3–12.
13. D. A. Mendis, H. L. F. Houpis, and J. R. Hill, J. Geophys. Res. **87**, 3449 (1982).
14. D. A. Mendis and M. Rosenberg, Annu. Rev. Astron. Astrophys. **32**, 419 (1994).
15. D. A. Mendis, Plasma Sources Sci. Technol. **11**, A219 (2002).
16. J. E. Howard, M. Horanyi, and G. R. Stewart, Phys. Rev. Lett. **83**, 3993 (1999); J. E. Howard and M. Horanyi, Geophys. Res. Lett. **28**, 1907 (2001).
17. N. N. Rao, Phys. Scr. **48**, 363 (1993).
18. M. Horanyi, Phys. Plasmas **7**, 3847 (2000).
19. P. K. Shukla and V. P. Silin, Phys. Scr. **45**, 508 (1992).
20. S. I. Popel, M. Y. Yu, and V. N. Tsytovich, Phys. Plasmas **3**, 4313 (1996).
21. S. I. Popel, A. P. Golub', and T. V. Losseva, Pis'ma Zh. Éksp. Teor. Fiz. **74**, 396 (2001) [JETP Lett. **74**, 362 (2001)].

JETP Letters, Vol. 77, No. 10, 2003, pp. 546–550. From Pis'ma v Zhurnal Éksperimental'noĭ i Teoreticheskoĭ Fiziki, Vol. 77, No. 10, 2003, pp. 649–653.
Original English Text Copyright © 2003 by Dyachenko, Korotkevich, Zakharov.

Weak Turbulence of Gravity Waves¶

A. I. Dyachenko[1], A. O. Korotkevich[1, *], and V. E. Zakharov[1, 2]

[1] *Landau Institute for Theoretical Physics, Russian Academy of Sciences, Moscow, 119334 Russia*

** e-mail: kao@landau.ac.ru*

[2] *University of Arizona, Department of Mathematics, Tucson, USA*

Received April 16, 2003

For the first time weak turbulent theory was demonstrated for surface gravity waves. Direct numerical simulation of the dynamical equations shows Kolmogorov turbulent spectra as predicted by analytical analysis [1] from kinetic equation. © *2003 MAIK "Nauka/Interperiodica".*

PACS numbers: 47.35.+i; 92.10.Hm

In this letter we numerically study the steady Kolmogorov spectra for spatially homogeneous gravity waves. According to the theory of weak turbulence, the main physical process here is the stationary energy flow to the small scales, where the energy dissipates [1, 2]. This flow is described by a kinetic equation which has power-like solutions—Kolmogorov spectra. This straightforward picture takes place experimentally and numerically for different physical situations. For capillary waves, it was observed on the surface of liquid hydrogen [3, 4]. The numerical simulation of this process was performed in [5]. In nonlinear fiber optics, these spectra were demonstrated in numerical simulation [6]. There are many other results [7–11]. One of the most interesting applications of weak turbulence theory is surface gravity waves. From the pioneering article by Toba [12] to the most recent observations [13], many experimentalists get the spectra predicted by weak turbulence theory. But these experiments cannot be treated as a complete confirmation, because the Zakharov–Filonenko spectrum is isotropic, while the observed spectra are essentially anisotropic. It is worth noting that the wave kinetic equation, which is the keystone of this theory, was derived under several assumptions. Namely, it was assumed that the phases of all interacting waves are random and are in a state of chaotic motion. The validity of this proposition is not clear *a priori*. The direct numerical simulation of nonlinear dynamical equations can confirm whether this assumption is valid or not. But for the particular case of gravity surface waves, the numerical confirmation was absent in spite of the significant efforts applied. The only successful attempt in this direction was the simulation of freely decaying waves [14]. The reason for that, in our opinion, was concerned with the choice of numerical scheme parameters. Namely, the numerical simulation is very sensitive to the width of resonance of four-wave interaction. It must be wide enough to provide resonance on the discrete grid, as was studied in [15] for decay of the monochromatic capillary wave. On the other hand, it has to be not too wide (due to nonlinear frequency shift) when the weak turbulent conditions fail. We have spent significant efforts to secure the right choice of numerical parameters. As a result, we have obtained the first evidence of the weak turbulent Kolmogorov spectrum for energy flow for surface gravity waves. The numerical simulation was surprisingly time consuming (in comparison to capillary waves turbulence), but we finally got a clear spectrum for surface elevation,

$$|\eta_k|^2 \sim \frac{1}{k^{7/2}}, \tag{1}$$

which is in agreement with real experiments [12, 13].

Theoretical background. Let us consider the potential flow of an ideal incompressible fluid of infinite depth and with a free surface. We use standard notations for velocity potential $\phi(\mathbf{r}, z, t)$, $\mathbf{r} = (x, y)$; $\mathbf{v} = \nabla\phi$ and surface elevation $\eta(\mathbf{r}, t)$. Fluid flow is irrotational $\Delta\phi = 0$. The total energy of the system can be represented in the form

$$H = T + U,$$

$$T = \frac{1}{2}\int d^2r \int_{-\infty}^{\eta} (\nabla\phi)^2 dz, \tag{2}$$

$$U = \frac{1}{2}g\int \eta^2 d^2r, \tag{3}$$

where g is the acceleration of gravity. It was shown [16] that under these assumptions the fluid is a Hamiltonian system

$$\frac{\partial\eta}{\partial t} = \frac{\delta H}{\delta\psi}, \quad \frac{\partial\psi}{\partial t} = -\frac{\delta H}{\delta\eta}, \tag{4}$$

¶ This article was submitted by the authors in English.

where $\psi = \phi(\mathbf{r}, \eta(\mathbf{r}, t), t)$ is a velocity potential on the surface of the fluid. In order to calculate the value of ψ we have to solve the Laplace equation in the domain with varying surface η. This problem is difficult. One can simplify the situation using the expansion of the Hamiltonian in powers of "steepness"

$$\begin{aligned} H &= \frac{1}{2}\int (g\eta^2 + \psi\hat{k}\psi)d^2r \\ &+ \frac{1}{2}\int \eta[|\nabla\psi|^2 - (\hat{k}\psi)^2]d^2r \\ &+ \frac{1}{2}\int \eta(\hat{k}\psi)[\hat{k}(\eta(\hat{k}\psi)) + \eta\Delta\psi]d^2r. \end{aligned} \tag{5}$$

For gravity wave, it is enough to take into account terms up to the fourth order. Here, $\hat{k}$ is the linear operator corresponding to multiplying of Fourier harmonics by modulus of the wavenumber $\mathbf{k}$. In this case, dynamical equations (4) acquire the form

$$\begin{aligned} \dot{\eta} &= \hat{k}\psi - (\nabla(\eta\nabla\psi)) - \hat{k}[\eta\hat{k}\psi] \\ &+ \hat{k}(\eta\hat{k}[\eta\hat{k}\psi]) + \frac{1}{2}\Delta[\eta^2\hat{k}\psi] + \frac{1}{2}\hat{k}[\eta^2\Delta\psi], \\ \dot{\psi} &= -g\eta - \frac{1}{2}[(\nabla\psi)^2 - (\hat{k}\psi)^2] \\ &- [\hat{k}\psi]\hat{k}[\eta\hat{k}\psi] - [\eta\hat{k}\psi]\Delta\psi + D_{\mathbf{r}} + F_{\mathbf{r}}. \end{aligned} \tag{6}$$

Here, $D_{\mathbf{r}}$ is some artificial damping term used to provide dissipation at small scales; $F_{\mathbf{r}}$ is a pumping term corresponding to external force (having in mind wind blow, for example). Let us introduce the Fourier transform

$$\psi_{\mathbf{k}} = \frac{1}{2\pi}\int \psi_{\mathbf{r}} e^{i\mathbf{kr}} d^2r, \quad \eta_{\mathbf{k}} = \frac{1}{2\pi}\int \eta_{\mathbf{r}} e^{i\mathbf{kr}} d^2r.$$

With these variables, Hamiltonian (5) acquires the form

$$\begin{aligned} H &= H_0 + H_1 + H_2 + \ldots, \\ H_0 &= \frac{1}{2}\int (|k||\psi_{\mathbf{k}}|^2 + g|\eta_{\mathbf{k}}|^2)d\mathbf{k}, \\ H_1 &= -\frac{1}{4\pi}\int L_{\mathbf{k}_1\mathbf{k}_2}\psi_{\mathbf{k}_1}\psi_{\mathbf{k}_2}\eta_{\mathbf{k}_3} \\ &\times \delta(\mathbf{k}_1 + \mathbf{k}_2 + \mathbf{k}_3)d\mathbf{k}_1 d\mathbf{k}_2 d\mathbf{k}_3, \\ H_2 &= \frac{1}{16\pi^2}\int M_{\mathbf{k}_1\mathbf{k}_2\mathbf{k}_3\mathbf{k}_4}\psi_{\mathbf{k}_1}\psi_{\mathbf{k}_2}\eta_{\mathbf{k}_3}\eta_{\mathbf{k}_4} \\ &\times \delta(\mathbf{k}_1 + \mathbf{k}_2 + \mathbf{k}_3 + \mathbf{k}_4)d\mathbf{k}_1 d\mathbf{k}_2 d\mathbf{k}_3 d\mathbf{k}_4. \end{aligned} \tag{7}$$

Here,

$$\begin{aligned} L_{\mathbf{k}_1\mathbf{k}_2} &= (\mathbf{k}_1\mathbf{k}_2) + |k_1||k_2|, \\ M_{\mathbf{k}_1\mathbf{k}_2\mathbf{k}_3\mathbf{k}_4} &= |\mathbf{k}_1||\mathbf{k}_2|\Big[\frac{1}{2}(|\mathbf{k}_1 + \mathbf{k}_3| + |\mathbf{k}_1 + \mathbf{k}_4| \\ &+ |\mathbf{k}_2 + \mathbf{k}_3| + |\mathbf{k}_2 + \mathbf{k}_4|) - |\mathbf{k}_1| - |\mathbf{k}_2|\Big]. \end{aligned} \tag{8}$$

It is convenient to introduce the canonical variables $a_{\mathbf{k}}$ as shown below:

$$a_{\mathbf{k}} = \sqrt{\frac{\omega_{\mathbf{k}}}{2k}}\eta_{\mathbf{k}} + i\sqrt{\frac{k}{2\omega_k}}\psi_{\mathbf{k}}, \tag{9}$$

where

$$\omega_k = \sqrt{gk}. \tag{10}$$

This is the dispersion relation for the case of infinite depth. Similar formulas can be derived in the case of finite depth [17]. With these variables, equations (4) take the form

$$\dot{a}_{\mathbf{k}} = -i\frac{\delta H}{\delta a^*_{\mathbf{k}}}. \tag{11}$$

The dispersion relation (10) is of the "nondecay type" and the equations

$$\omega_{k_1} = \omega_{k_2} + \omega_{k_3}, \quad \mathbf{k}_1 = \mathbf{k}_2 + \mathbf{k}_3 \tag{12}$$

have no real solution. This means that, in the limit of small nonlinearity, the cubic terms in the Hamiltonian can be excluded by a proper canonical transformation $a(\mathbf{k}, t) \longrightarrow b(\mathbf{k}, t)$ [18]. The formula of this transformation is rather bulky and well known [17, 18], so let us omit the details here.

For statistical description of a stochastic wave field, one can use a pair correlation function

$$\langle a_{\mathbf{k}} a^*_{\mathbf{k}'}\rangle = n_k\delta(\mathbf{k} - \mathbf{k}'). \tag{13}$$

The $n_{\mathbf{k}}$ is a measurable quantity, connected directly with observable correlation functions. For instance, from (9) one can get

$$I_k = \langle|\eta_{\mathbf{k}}|^2\rangle = \frac{1}{2}\frac{\omega_k}{g}(n_k + n_{-k}). \tag{14}$$

In the case of gravity waves, it is convenient to use another correlation function,

$$\langle b_{\mathbf{k}} b^*_{\mathbf{k}'}\rangle = N_k\delta(\mathbf{k} - \mathbf{k}'). \tag{15}$$

The function N_k cannot be measured directly. The relation connecting n_k and N_k is rather complex in the case of a fluid of finite depth. But in the case of deep water, it becomes very simple [17]:

$$\frac{n_k - N_k}{n_k} \simeq \mu, \tag{16}$$

where $\mu = (ka)^2$. Here, a is a characteristic elevation of the free surface. In the case of the weak turbulence $\mu \ll 1$. The correlation function N_k obeys the kinetic equation [1]

$$\frac{\partial N_k}{\partial t} = st(N, N, N) + f_p(k) - f_d(k). \tag{17}$$

Here,

$$\begin{aligned} st(N, N, N) &= 4\pi \int \left|T_{\mathbf{k}, \mathbf{k}_1, \mathbf{k}_2, \mathbf{k}_3}\right|^2 \\ &\times (N_{k_1} N_{k_2} N_{k_3} + N_k N_{k_2} N_{k_3} - N_k N_{k_1} N_{k_2} \\ &- N_k N_{k_1} N_{k_3}) \delta(\mathbf{k} + \mathbf{k}_1 - \mathbf{k}_2 - \mathbf{k}_3) d\mathbf{k}_1 d\mathbf{k}_2 d\mathbf{k}_3. \end{aligned} \tag{18}$$

The complete form of matrix element $T_{\mathbf{k}, \mathbf{k}_1, \mathbf{k}_2, \mathbf{k}_3}$ can be found in many sources [1, 2, 17]. Function $f_p(k)$ in (17) corresponds to wave pumping due to wind blowing, for example. Usually it is located on long scales. Function $f_d(k)$ represents the absorption of waves due to viscosity and wave-breaking. None of these functions are known to a sufficient degree.

Let us consider stationary solutions of Eq. (17) assuming that

—the medium is isotropic with respect to rotations;

—dispersion relation is a power-like function: $\omega = ak^\alpha$;

—$T_{\mathbf{k}, \mathbf{k}_1, \mathbf{k}_2, \mathbf{k}_3}$ is a homogeneous function:

$$T_{\epsilon\mathbf{k}, \epsilon\mathbf{k}_1, \epsilon\mathbf{k}_2, \epsilon\mathbf{k}_3} = \epsilon^\beta T_{\mathbf{k}, \mathbf{k}_1, \mathbf{k}_2, \mathbf{k}_3}.$$

Under these assumptions, one can get Kolmogorov solutions [18]

$$\begin{aligned} n_k^{(1)} &= C_1 P^{1/3} k^{-\frac{2\beta}{3} - d}, \\ n_k^{(2)} &= C_2 Q^{1/3} k^{-\frac{2\beta - \alpha}{3} - d}. \end{aligned} \tag{19}$$

Here, d is a spatial dimension ($d = 2$ in our case). The first one is a Kolmogorov spectrum, corresponding to a constant flux of energy P to the region of small scales (direct cascade of energy). The second one is the Kolmogorov spectrum, describing inverse cascade of wave action to large scales, and Q is a flux of action. In both cases, C_1 and C_2 are dimensionless "Kolmogorov constants."

In the case of deep water, $\omega = \sqrt{gk}$ and, apparently, $\beta = 3$. It has been known since [1] that for deep water

$$n_k^{(1)} = C_1 P^{1/3} k^{-4}. \tag{20}$$

In the same way [19], for the second spectrum,

$$n_k^{(2)} = C_2 Q^{1/3} k^{-23/6}. \tag{21}$$

In this letter, we will explore the first spectrum (energy cascade). Using (14), one can get

$$I_k = \frac{C_1 g^{1/2} P^{1/3}}{k^{7/2}}. \tag{22}$$

Numerical Simulation. Dynamical Eqs. (6) are very hard for analytical analysis. One of the main obstacles is the $\hat{k}$ operator, which is nonlocal. However, using the Fourier technique makes practically no difference between the derivative and $\hat{k}$. The numerical simulation of the system is based on consequent application of the fast Fourier transform algorithm. The details of this numerical scheme will be published separately.

For numerical integration of (6), we used the functions F and D defined in the Fourier space

$$\begin{aligned} F_k &= f_k e^{iR_\mathbf{k}(t)}, \\ f_k &= 4F_0 \frac{(k - k_{p1})(k_{p2} - k)}{(k_{p2} - k_{p1})^2}; \\ D_\mathbf{k} &= \gamma_k \psi_\mathbf{k}, \\ \gamma_k &= -\gamma_1, \quad k \le k_{p1}, \\ \gamma_k &= -\gamma_2 (k - k_d)^2, \quad k > k_d. \end{aligned} \tag{23}$$

Here, $R_\mathbf{k}(t)$ is the uniformly distributed random number in the interval $(0, 2\pi)$. We solved the system of Eqs. (6) in the periodic domain $2\pi \times 2\pi$ (the wave numbers k_x and k_y are integers in this case). The size of the grid was chosen as 256 x 256 points. Acceleration of gravity $g = 1$. Parameters of the damping and pumping were the following: $k_{p1} = 5$, $k_{p2} = 10$, $k_d = 64$. Thus, the inertial interval is about half a decade.

During the simulations, we paid special attention to problems that could "damage" the calculations, first of all, the bottleneck phenomenon at the boundary between inertial interval and dissipation region. This effect is very fast but can be effectively suppressed by proper choice of damping value γ_2 in the case of moderate pumping values F_0. The second problem is the accumulation of "condensate" in low wave numbers. This mechanism for the case of capillary waves was examined in detail in [15]. This obstacle can be overcome by a simple adaptive damping scheme in small wave numbers. After some time, the system reaches the stationary state, where equilibrium between pumping and damping takes place. An important parameter in this state is the ratio of nonlinear to linear energy $(H_1 + H_2)/H_0$.

For example, in the case of $F_0 = 2 \times 10^{-4}$, $\gamma_1 = 1 \times 10^{-3}$, $\gamma_2 = 400$, the level of nonlinearity was equal to $(H_1 + H_2)/H_0 \simeq 2 \times 10^{-3}$. The Hamiltonian as a function of time is shown in Fig. 1.

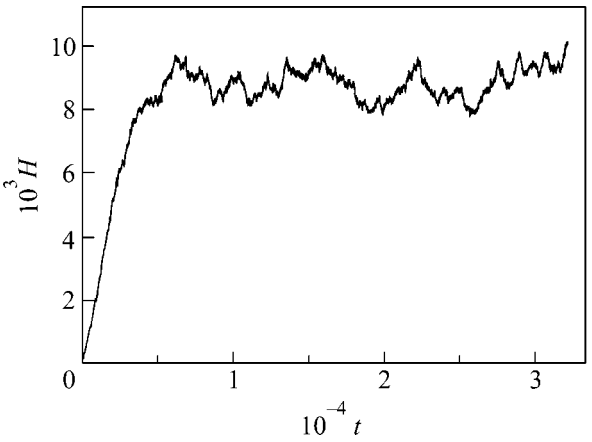

Fig. 1. Hamiltonian as a function of time.

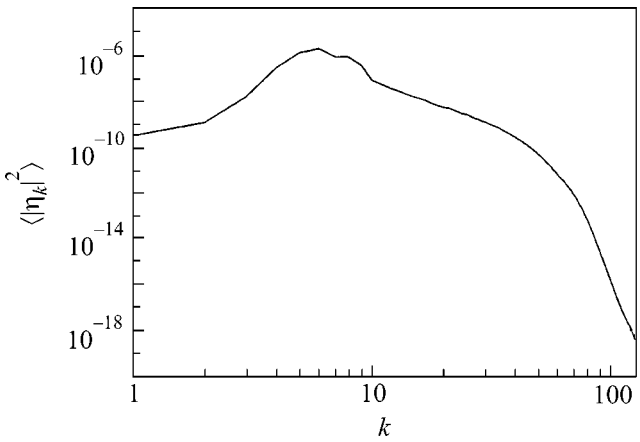

Fig. 2. The logarithm of the correlator function of surface elevation as a function of logarithm of the wave number.

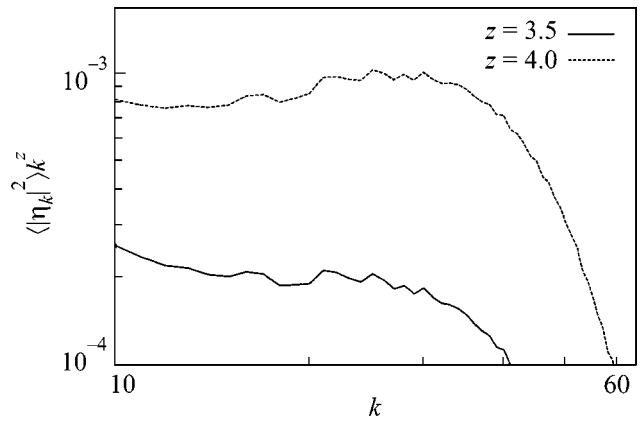

Fig. 3. Compensated correlators in inertial interval for different values of the compensation power: $z = 3.5$ solid line (weak turbulence theory), $z = 4.0$ dashed one (Phillips theory).

The surface elevation correlator function appears to be power-like in the essential part of inertial interval, where the influence of pumping and damping was small. The correlator is shown in Fig. 2.

One can try to estimate the exponent of the spectrum. It is worth noting that an alternative spectrum was proposed earlier by Phillips [20]. That power-like spectrum is due to the wave-breaking mechanism and gives us a surface elevation correlator as $I_k \sim k^{-4}$. Compensated spectra are shown in Fig. 3. This seems to be evidence that the Kolmogorov spectrum predicted by weak turbulence theory better fits the results of the numerical experiment.

The inertial interval was rather narrow (half a decade). But the obtained results allow us to conclude that the accuracy of experiment was good enough under the time constraints of simulation (we get the steady state after 20–30 h using available hardware, and we need several days to average the $|\eta_k|^2$ function). Simulation on a larger grid (512×512, for example) can make the accuracy better. But even these results give us a clear qualitative picture.

This work was supported by RFBR grant no. 03-01-00289, INTAS grant no. 00-292, the Program "Nonlinear dynamics and solitons" from the RAS Presidium, a grant by "Leading Scientific Schools of Russia," the US Army Corps of Engineers, RDT&E Program, grant DACA no. 42-00-C0044, and NSF grant no. NDMS0072803.

The authors thank the creators of the open-source fast Fourier transform library FFTW [21] for this fast, portable, and completely free piece of software.

REFERENCES

1. V. E. Zakharov and N. N. Filonenko, Dokl. Akad. Nauk SSSR **170**, 1292 (1966) [Sov. Phys. Dokl. **11**, 881 (1966)].
2. V. E. Zakharov and N. N. Filonenko, J. Appl. Mech. Tech. Phys. **4**, 506 (1967).
3. M. Yu. Brazhnikov, G. V. Kolmakov, A. A. Levchenko, and L. P. Mezhov-Deglin, Pis'ma Zh. Éksp. Teor. Fiz. **74**, 660 (2001) [JETP Lett. **74**, 583 (2001)].
4. M. Yu. Brazhnikov, G. V. Kolmakov, and A. A. Levchenko, Zh. Éksp. Teor. Fiz. **122**, 521 (2002) [JETP **95**, 447 (2002)].
5. A. N. Pushkarev and V. E. Zakharov, Phys. Rev. Lett. **76**, 3320 (1996).
6. A. I. Dyachenko, A. C. Newell, A. Pushkarev, and V. E. Zakharov, Physica D (Amsterdam) **57**, 96 (1992).
7. F. Dias, P. Guyenne, and V. E. Zakharov, Phys. Lett. A **291**, 139 (2001).
8. V. E. Zakharov, O. A. Vasilyev, and A. I. Dyachenko, Pis'ma Zh. Éksp. Teor. Fiz. **73**, 68 (2001) [JETP Lett. **73**, 63 (2001)].
9. Y. V. Lvov and E. G. Tabak, Phys. Rev. Lett. **87**, 168501 (2001).

10. S. Galtier, S. V. Nazarenko, A. C. Newell, and A. Pouquet, Astrophys. J. **564**, L49 (2002).
11. S. L. Musher, A. M. Rubenchik, and V. E. Zakharov, Phys. Rep. **252**, 178 (1995).
12. Y. Toba, J. Oceanogr. Soc. Jpn. **29**, 209 (1973).
13. P. A. Hwang, D. W. Wang, E. J. Walsh, *et al.*, J. Phys. Oceanogr. **30**, 2753 (2000).
14. M. Onorato, A. R. Osborne, M. Serio, *et al.*, Phys. Rev. Lett. **89**, 144501 (2002).
15. A. I. Dyachenko, A. O. Korotkevich, and V. E. Zakharov, Pis'ma Zh. Éksp. Teor. Fiz. **77**, 572 (2003) [JETP Lett. **77**, 477 (2003)].
16. V. E. Zakharov, J. Appl. Mech. Tech. Phys. **2**, 190 (1968).
17. V. E. Zakharov, Eur. J. Mech. B/Fluids **18** (3), 327 (1999).
18. V. E. Zakharov, G. Falkovich, and V. S. Lvov, *Kolmogorov Spectra of Turbulence*, Vol. 1: *Wave Turbulence* (Springer, Berlin, 1992).
19. V. E. Zakharov and M. M. Zaslavskii, Izv. Atmos. Ocean. Phys. **18**, 747 (1982).
20. O. M. Phillips, J. Fluid Mech. **4**, 426 (1958).
21. http://fftw.org.

JETP Letters, Vol. 77, No. 10, 2003, pp. 551–555. Translated from Pis'ma v Zhurnal Éksperimental'noĭ i Teoreticheskoĭ Fiziki, Vol. 77, No. 10, 2003, pp. 654–658.
Original Russian Text Copyright © 2003 by Zaburdaev, Chukbar.

Memory Effects in Stochastic Transport

V. Yu. Zaburdaev and K. V. Chukbar*

Russian Research Centre Kurchatov Institute, pl. Kurchatova 1, Moscow, 123182 Russia

**e-mail: chukbar@dap.kiae.ru*

Received April 24, 2003

The memory effects in stochastic transport, namely, the dependence of the form of transport equations on the macroscopic time are considered. Equations explicitly taking into account the microscopic aspect of the problem, without which the transfer processes cannot be adequately described, are derived; the methods of their solution are suggested; and the asymptotic properties of the latter are analyzed. © *2003 MAIK "Nauka/Interperiodica".*

PACS numbers: 05.60.Cd; 05.40.Fb

In recent years, growing interest has been shown in the processes of stochastic transport because of the spatial and temporal nonlocalities inherent in this phenomenon [1–4]. The use of an adequate mathematical language of fractional derivatives [5, 6] and stable distributions [1, 7] allowed the physical theory of random transport to be substantially generalized, as compared to the primitive diffusion picture.

There are many physical reasons that are responsible for the above-mentioned nonlocalities (fractional derivatives) in the transport equations (see discussion in [8, 9]). One of the most frequently occurring phenomena is the presence of slowly damping spatial and time correlations in the motion of individual particles in a spreading cloud. Inasmuch as the macroscopic (for cloud) transport equations are derived from the random walk model for individual (not necessarily physical) particles, these equations basically have an asymptotic character. In our preceding work [8], concerning the effects caused by the limited walk rate, we drew attention to the nontriviality of this asymptotic transition and to the nontrivial dependence of the macroscopic transport on the microscopic details and on the initial conditions. It is our purpose to reveal, in this work, the details of the physical consequences of this ideological and mathematical nontriviality.

Evidently, one should expect that evolution is continuous for any physical process satisfying the causality principle: if the solution to the equations is functionally related to the initial state by the Green's function G_t, i.e., if $n(x, t) = G_{t} * n(t = 0)$, then

$$G_{t_1 + t_2} * n(t = 0) = G_{t_2} * n(t = t_1) = G_{t_2} * (G_{t_1} * n(t = 0)). \quad (1)$$

In other words, if we consider the state at any time t_1 as a new initial condition, we do not disturb the evolution continuity. Nevertheless, the equations discussed in all available works devoted to the nonlocal nondiffusion transport with a fractional time derivative, including a recent excellent review [4], strictly speaking, do not possess this property. This unpleasant fact has in no way been discussed in the literature, though it is precisely the point that is expected to be helpful in the recognition of a hidden defect of the above-mentioned description, namely, of the incompleteness in the description of a particle cloud only in terms of its macroscopic concentration $n(x, t)$. Interestingly, similar problems arise for strongly coupled coulombic systems in the quantum kinetic theory, where the solutions show a strong dependence on the initial correlations [10].

An attempt to unravel this phenomenon leads to the paradoxical conclusion that, even in the cases where the effective equation for macroscopic evolution reduces to the classical diffusion equation containing the familiar first-order time derivative (evidently, satisfying Eq. (1)), the defect is often "hidden under the rug." In reality, the time for approaching the microscopic evolution regime strongly depends on the initial condition and can be much longer than the microscopic time $\langle\tau\rangle$ characterizing the random walk of individual particles (see below). This is especially characteristic of the subdiffusion time operators.

Therefore, the memory effects considered in this work consist not in the familiar temporal nonlocality (fractional derivative) in the effective transport equation but in the fact that the form of this equation depends on the macroscopic time t (see below).

When deriving the transport equations, we will use, as in [6, 8], the standard random walk model. A one-dimensional motion of a particle along the x axis obeys the probability laws $g(|x|)$ and $f(t)$: a particle appearing at any point (say, x_0) may undergo an instantaneous jump to the neighboring points in such a way that the probability of finding it in the interval $(x_0 + x, x_0 + x + dx)$ equals $g(x)dx$, and this transfer proceeds after some waiting process, so that the probability of escaping the

particle residence in the interval $(t, t + dt)$ is equal to $f(t)dt$. For the convenience of intermediate calculations, we choose, without loss of generality, these functions in the form [6, 8]

$$g(x) = \frac{\Gamma(\beta + 1/2)}{\sqrt{\pi}\Gamma(\beta)} \frac{1}{(1 + x^2)^{\beta + 1/2}}; \quad f(t) = \frac{\gamma}{(1 + t)^{\gamma + 1}}. \tag{2}$$

Here, Γ is the Euler gamma function, and the numerical coefficients are determined by the unity normalization condition for g and f. The exponents of the power-law "tails" parameterized by the positive indices β and γ are only essential for further consideration.

The particles at point x "remember" their time of arrival at this point, so that their spatial density n is the integral of a certain distribution N over the "lifetime" τ:

$$n(x, t) = \int_0^\infty N(x, t, \tau)d\tau.$$

Let us define the transition to the subsequent motion in terms of "probability of surviving to time τ," which is simply related to the function f as

$$F(\tau) = 1 - \int_0^\tau f(t)dt.$$

Then, the particle flux $Q(x, t)$ leaving (on both sides and at all distances) a given point can be expressed using the formula for the conditional probability (see [6])

$$Q(x, t) = \int_0^\infty \frac{N(x, t, \tau)}{F(\tau)} f(\tau)d\tau. \tag{3}$$

We can now write the balance equations for the particle at a given time and a given point:

$$n(x, t) = \int_{-\infty}^{+\infty} g(x') \int_0^t Q(x - x', t - t')F(\tau')dt'dx' + \int_t^\infty \frac{N_0(x, \tau - t)}{F(\tau - t)} F(\tau)d\tau. \tag{4}$$

The last term on the right-hand side of this equation accounts for the effect of initial particle lifetime distribution $N_0(x, \tau) \equiv N(x, 0, \tau)$. The set of Eqs. (3) and (4) completely describes the situation and, obviously, satisfies condition (1). Note that, if $N_0 = n_0\delta_+(\tau)$ ("shifted" Dirac delta function: $\int_0^\infty \delta_+(\tau)d\tau = 1$), then, after the arrival of new particles at each point (at any $t > 0$), the self-similar profile

$$N(t, \tau) = \theta(t - \tau)P(t - \tau)F(\tau) \tag{5}$$

forms instantaneously with the correlated dependence on t and τ, where P is the incoming flux and $\theta(t)$ is the Heaviside step function. In this case, one can pass from the set of Eqs. (3) and (4) to a single basic equation for the macroscopic density n [6]:

$$n(x, t) = \int_{-\infty}^{+\infty} g(x') \times \int_0^t f(t')n(x - x', t - t')dt'dx' + F(t)n_0(x). \tag{6}$$

The Green's function of this equation reads

$$G_{k, p} = \frac{F_p}{1 - f_p g_k}, \tag{7}$$

where the symbol $[\cdot]_{k, p}$ denotes the Fourier and/or Laplace component of the corresponding function.

The transport equation can also be written in terms of only n if $f = \mu\exp(-\mu t)$ ($\mu = 1/\langle\tau\rangle$); then F and f (and, hence, Q and n) are proportional to each other. The reason for setting off the exponential law is quite clear, because only in this case does a fixed percentage of the sitting particles leave the point, irrespective of the time of their arrival at this point; i.e., all particles $\int_0^\infty N(\tau)d\tau$ in a "common bag" are in the same conditions. In all other cases, the "reel game" depends on the waiting time τ, and one cannot ignore the details of the $N(\tau)$ distribution.

In the majority of works, Eq. (6) is written without any substantiation, which should imply that either one of the two above-mentioned conditions is fulfilled or a certain model is used (the authors of those works did not discuss this issue). In the general case, Eq. (6) is valid only for a certain asymptotic meaning: a time must be elapsed (see below) until the self-similar dependence (5) covers the larger part of the $N(\tau)$ profile and becomes dominating Q, as compared to N_0. One can readily verify that condition (1) is met for Eq. (6) only if $f = \mu\exp(-\mu t)$. In all other cases, one should use the initial set of Eqs. (3) and (4) to adequately describe the transport process. In what follows, we propose a method for solving this set exactly and show that the initial particle lifetime distribution influences the subsequent evolution.

To begin with, it is convenient to divide $N(x, t, \tau)$ into two terms (see Eq. (4)):

$$N_1(x, t, \tau) = \frac{N_0(x, \tau - t)F(\tau)}{F(\tau - t)}\theta(\tau - t); \tag{8}$$

$$N_2(x, t, \tau) = \int_{-\infty}^{+\infty} g(x')F(\tau)Q(x - x', t - \tau)\theta(t - \tau)dx', \quad \tau < t. \tag{9}$$

The term N_1 describes the particles living at the time point $\tau > t$, i.e., those particles of the initial distribution N_0 which survived up to time t. The term N_2 is the particle profile formed by the flux $Q(x, t)$, to which both N_1 and N_2 make a contribution. The equation for N_2 is analogous to Eq. (4) and follows from Eq. (3) for the flux:

$$N_2(x, t, \tau) = F(\tau)\int_{-\infty}^{+\infty} g(x')\left\{\int_0^{t-\tau}\frac{N_2(x-x', t-\tau, \tau_1)f(\tau_1)}{F(\tau_1)}d\tau + \int_{t-\tau}^{+\infty}\frac{N_1(x-x', t-\tau_1, \tau_1)f(\tau_1)}{F(\tau_1)}d\tau\right\}dx'. \quad (10)$$

Let us substitute Eqs. (8) and (9) in Eq. (10) and perform the Laplace and Fourier transforms with respect to time and spatial variables, respectively, to get rid of convolution integrals. After this, we again use Eq. (9) and set off the term $N_{2p,k}$ on the right-hand side of the resulting expression. By solving the linear equation for this term, we get

$$N_{2p,k}(\tau) = \frac{g_k F(\tau)\exp(-p\tau)}{1-f_p g_k}\times\left(\int_t^{+\infty}\frac{N_{0k}(\tau_1-t)f(\tau_1)d\tau_1}{F(\tau_1-t)}\right)_p. \quad (11)$$

The particle density can also be written as the sum of two terms $n = n_1 + n_2$, where

$$n_1 = \int_t^{\infty} N_1(x, t, \tau)d\tau, \quad n_2 = \int_0^t N_2(x, t, \tau)d\tau.$$

Since N_2 depends on its variables in the self-similar manner (9) (cf. Eq. (5)), we can write

$$n_{2p,k} = \frac{F_p N_{2p,k}}{F(\tau)\exp(-p\tau)}. \quad (12)$$

Now, using Eqs. (8) and (11) and the relationship $f_p(t + t') = F(t') - pF_p(t + t')$ (hereafter, the index p denotes the Laplace transform with respect to t), we obtain, after simple mathematics,

$$n_{p,k} = \frac{1}{1-f_p g_k}\times\left\{F_p n_{0k} + (1-g_k)\int_0^{\infty} N_{0k}(\tau)\left(\frac{F(\tau+t)}{F(\tau)} - F(t)\right)_p d\tau\right\}. \quad (13)$$

Note that the first term in braces is the solution to Eq. (6) for the density (see [6]), and, hence, the second term demonstrates the dependence of the solution on the initial lifetime distribution. Note again that the second term becomes zero for $F(t) = \exp(-\mu t)$; i.e., the dependence on the microscopic distribution vanishes.

To demonstrate the distinctions between Eqs. (13) and (6), we consider an example with the initial condition $N_0(x, \tau) = n_0(x)\delta_+(\tau - t_0)$, where t_0 is a certain nonnegative delay time. In this case, the solution can be written in a different and more compact form. By substituting the initial condition into Eq. (11) and using Eq. (12), we obtain

$$n_{2p,k} = \frac{g_k}{F(t_0)}\frac{F_p n_{0k}}{1-f_p g_k} f_p(t + t_0),$$

$$n_1 = \frac{F(t + t_0)n_0(x)}{F(t_0)}.$$

Finally, we write the expression for the particle density $n(x, t)$

$$n(x, t) = \frac{1}{F(t_0)}\left(\int_{-\infty}^{+\infty} dx' g(x') \times \int_0^t f(\tau + t_0)\tilde{n}(x-x', t-\tau)d\tau + F(t + t_0)n_0(x)\right),$$

where $n(x, t)$ stands for the already known solution to Eq. (6), towards which $\tilde{n}(x, t)$ tends at large t's. However, the initial stage of density evolution at $t < t_0$, which, depending on t_0, can be rather prolonged, proceeds in a different way. For clearness, let us consider the situation with $\beta, \gamma > 1$. In this case, the function f has a nonzero first moment $\langle\tau\rangle$ (mean waiting time) and the function g has a finite or noninfinite second moment $\langle x^2\rangle$ (mean square displacement). Hence, after expanding the integrand in Eq. (6) with allowance for the smallnesses $t \gg \langle\tau\rangle$ and $x \gg \sqrt{\langle x^2\rangle}$, we should arrive at the standard diffusion equation with the coefficient $D = \langle x^2\rangle/2\langle\tau\rangle$. In our situation, this is not the case. After expanding the expression for n_1 in powers of the small parameter $t/t_0 \ll 1$, we see that the number of such particles decreases linearly with time following the law

$$n_1(x, t) \simeq n_0(x)(1 - \gamma t/t_0), \quad (14)$$

which leads, correspondingly, to a linear increase in the number of particles n_2, so that the evolution of density n_2 at $t \gg \langle\tau\rangle$ obeys the diffusion equation with a constant source on the right-hand side:

$$\frac{\partial n_2}{\partial t} = D\frac{\partial^2 n_2}{\partial x^2} + \varphi(x);$$
$$\varphi(x) = \frac{\gamma}{t_0}\int_{-\infty}^{+\infty} g(x')n_0(x-x')dx', \quad D = \frac{\langle x^2\rangle}{2\langle\tau\rangle}. \quad (15)$$

Its solution has the form (see, e.g., [11])

$$n_2(x, t) = \int_0^{t} \int_{-\infty}^{+\infty} \frac{\varphi(\xi, t)}{\sqrt{4\pi D(t-\tau)}} \exp\left(-\frac{(x-\xi)^2}{4D(t-\tau)}\right) d\xi d\tau. \quad (16)$$

Denoting by x_0 the characteristic width of the function $\varphi(x)$ and by $t_D = x_0^2/D$ the corresponding diffusion time, one can replace φ by the delta function if the inequalities $t_D \ll t \ll t_0$ are fulfilled and arrive, after integrating with respect to the coordinate, at an even simpler expression.

Consequently, the introduction of a delay time t_0 into the initial lifetime distribution brings about a deviation from the standard picture on the interval $\langle\tau\rangle < t < t_0$ even for the parameters β and γ corresponding to the conventional diffusion. The particles in the initial distribution decrease in number, according to Eq. (14), and serve as a source for the formation of the self-similar n_2 profile (16). This is so because of the absence of any internal scale in a power function. For instance, the exponential law is characterized by the time $\langle\tau\rangle$, which indicates that the function at $t = t_0 + \langle\tau\rangle$ decreases by e times compared to its value at $t = t_0$, irrespective of the chosen t_0. One can easily verify that such is not the case for a power function. Moreover, as t_0 increases, one is forced to wait an even longer time $t_1 \sim t_0$, after which the function decreases, e.g., twofold, and $t_1 \longrightarrow \infty$ for $t_0 \longrightarrow \infty$.

Let us now turn to the property (1). This problem differs from the preceding one in that the initial distribution N_0 is now not arbitrary but arises from the preliminary evolution of $\delta_+(\tau)$ during time t_1 according to Eqs. (3) and (4). In the case where the transport process is described asymptotically by the conventional diffusion equation, the time it takes for establishing the self-similar solution is determined by the microscopic time $\langle\tau\rangle$; i.e., Eq. (1) is fulfilled even at $t_1, t_2 \gg \langle\tau\rangle$. This is not the case for the subdiffusion regime. Let us apply the Laplace transform with respect to variables t_1 and t_2 to Eq. (1) and use the property

$$[f(t_1 + t_2)]_{p_1, p_2} = \frac{[f(t_1)]_{p_1} - [f(t_2)]_{p_2}}{p_2 - p_1}.$$

Then the relationship

$$\frac{G_{p_1} - G_{p_2}}{p_2 - p_1} = G_{p_2} G_{p_1}$$

must be fulfilled. One can easily verify that it is valid for the Green's function of the form (7) only if $p_2 \ll p_1$ or $t_2 \gg t_1$. This signifies that, depending on the duration t_1 of the first evolution stage, the time $t_2 \sim t_1$ is required for establishing the previous self-similar solution. The real transport process at times $t_2 \ll t_1$ can be described using the equations with a source on the right-hand side, as was done for the model problem with time delay (see above). However, in contrast to the example considered, a decrease in n_1 in this case and, correspondingly, an increase in the number of particles n_2 would be more rapid (at small t), because $N_0(\tau)$ is no longer concentrated at the far boundary $\tau = t_1$ but is extended over the entire interval $(0, t_1)$. For example, the source $q(x, t)$ in the equation for n_2 (cf. [12])

$$\frac{\partial^\gamma n_2(x, t)}{\partial t^\gamma} = \frac{1}{2}\frac{\partial^2 n_2}{\partial x^2} + q(x, t)$$

brings about an increase in n_2 according to the law

$$\int_{-\infty}^{+\infty} n_2(x, t) dx \propto t^{1-\gamma}.$$

In summary, we have demonstrated that the microscopic features of the initial distribution have a sizable effect on the process of stochastic transport. These features should be explicitly taken into account in the transport equation because they are responsible for the memory effects, specifically, for the dependence of the form of the equation on the macroscopic time. This additional degree of freedom allows the first stage of system evolution to be modified. This stage can be rather prolonged, as we have demonstrated by a model example where the effective equations are different from the classical diffusion equation even for the diffusional parameters of the problem (for the functions of class (2)). The number of particles in the initial condition linearly decreases with time to form a profile whose evolution is described by the diffusion equation with a constant source. The reason is that a power function describing the waiting time at any point for a particle executing random walk has no internal scale. Taking account of the initial distribution allows one to remove the main drawback consisting in the violation of evolution continuity in the asymptotic equation and use the subdiffusion equation with a time-independent source for the description of the transient process of profile formation by the particles of the initial distribution. We can say that the zero moment of a distribution function, i.e., the total number of particles, is insufficient for a correct description of the process. This function must be represented as a sum of terms, each corresponding to its own type of particles. A simple illustration of this approach is provided by the initial lifetime distribution in the form of a comb of shifted delta functions. However, it turns out that the division of particles even into two classes and the inclusion of the next moment of the distribution function (transition time from one sort of particles to the other) appreciably improves the accuracy of equations.

This work was supported by the Russian Foundation for Basic Research (project no. 03-02-16765) and Scientific School (project no. 2292.2003.2).

REFERENCES

1. E. W. Montroll and M. F. Schlesinger, in *Studies in Statistical Mechanics*, Ed. by J. Leibowitz and E. W. Montroll (North-Holland, Amsterdam, 1984), Vol. 2, p. 1.
2. J.-P. Bouchand and A. Georges, Phys. Rep. **195**, 127 (1990).
3. M. B. Isichenko, Rev. Mod. Phys. **64**, 961 (1992).
4. J. Klafter and R. Metzler, Phys. Rep. **339**, 1 (2000).
5. G. M. Zaslavsky, Physica D (Amsterdam) **76**, 110 (1994).
6. K. V. Chukbar, Zh. Éksp. Teor. Fiz. **108**, 1875 (1995) [JETP **81**, 1025 (1995)].
7. V. M. Zolotarev, V. V. Uchaĭkin, and V. V. Saenko, Zh. Éksp. Teor. Fiz. **115**, 1411 (1999) [JETP **88**, 780 (1999)].
8. V. Yu. Zaburdaev and K. V. Chukbar, Zh. Éksp. Teor. Fiz. **121**, 299 (2002) [JETP **94**, 252 (2002)].
9. K. V. Chukbar, Zh. Éksp. Teor. Fiz. **109**, 1335 (1996) [JETP **82**, 719 (1996)].
10. D. Semkat, D. Kremp, and M. Bonitz, J. Math. Phys. **41**, 7458 (2000).
11. V. S. Vladimirov, *Generalized Functions in Mathematical Physics* (Nauka, Moscow, 1976; Mir, Moscow, 1979), p. 218.
12. L. A. Bol'shov, A. M. Dykhne, and P. S. Kondratenko, Pis'ma Zh. Éksp. Teor. Fiz. **75**, 291 (2002) [JETP Lett. **75**, 246 (2002)].

Translated by V. Sakun

JETP Letters, Vol. 77, No. 10, 2003, pp. 556–560. Translated from Pis'ma v Zhurnal Éksperimental'noĭ i Teoreticheskoĭ Fiziki, Vol. 77, No. 10, 2003, pp. 659–663.
Original Russian Text Copyright © 2003 by Belim.

Effect of Elastic Deformations on the Critical Behavior of Three-Dimensional Systems with Long-Range Interaction

S. V. Belim

Omsk State University, Omsk, 644077 Russia

e-mail: belim@univer.omsk.su

Received March 31, 2003

A field-theoretical description of the behavior of compressible Ising systems with long-range interactions is presented. The description is performed in the two-loop approximation in three dimensions with the use of the Padé–Borel resummation technique. The renormalization group equations are analyzed, and the fixed points that determine the critical behavior of the system are found. It is shown that the effect of elastic deformations on a system with a long-range interaction causes changes in its critical, as well as multicritical, behavior.
© *2003 MAIK "Nauka/Interperiodica".*

PACS numbers: 46.05.+b; 46.25.Cc; 64.60.Ak

In compressible systems, the relation of the order parameter to elastic deformations plays an important role. Earlier [1] it was shown that, in the case of an elastically isotropic body, the critical behavior of a compressible system with a quadratic striction is unstable with respect to the relation of the order parameter to acoustic modes, and a first-order phase transition close to a second-order one is realized. However, the conclusions formulated in the cited paper [1] hold only for low pressures. As was shown later [2], at high pressures beginning from a certain tricritical point P_t, the deformations induced by the external pressure affect the system to a greater extent and lead to a change of sign of the effective interaction constant for the order parameter fluctuations and, as a consequence, to a change in the order of the phase transition. In this case, according to [2], a homogeneous compressible system is characterized by two types of tricritical behavior with a fourth-order critical point formed as the point of intersection of the two tricritical curves. Calculations performed in terms of the two-loop approximation [3] confirmed the presence of two types of tricritical behavior for Ising systems and provided values of the tricritical indices.

In structural phase transitions that occur in the absence of the piezoelectric effect, in the paraphase the elastic strains play the role of a secondary order parameter whose fluctuations are not critical in most cases.

The effect of the long-range interaction described by the power law $1/r^{-D-a}$ at long distances was studied analytically in terms of the ε expansion [4–6] and numerically by the Monte Carlo method [7–9] in two and three dimensions. It was found that the long-range interaction considerably affects the critical behavior of Ising systems for the parameter values $a < 2$. A recent study carried out for a three-dimensional space in the two-loop approximation [10] confirmed the prediction of the ε expansion for systems with long-range interactions.

This paper describes the critical and tricritical behavior of three-dimensional compressible systems by taking into account the effect of the long-range interaction with different values of the parameter a.

For a homogeneous Ising-like model with elastic deformations and a long-range interaction, the Hamiltonian can be represented in the form

$$H_0 = \int d^D x \left[\frac{1}{2}(\tau_1 + \nabla^a)S(x)^2 + \frac{u_0}{4!}(S(x)^2)^2\right] + \int d^D x \left[a_1\left(\sum_{\alpha=1}^{3} u_{\alpha\alpha}(x)\right)^2 + a_2 \sum_{\alpha,\beta=1}^{3} u_{\alpha\beta}^2\right] + \frac{1}{2}a_3 \int d^D x \mathbf{S}(x)^2 \left(\sum_{\alpha=1}^{3} u_{\alpha\alpha}(x)\right), \quad (1)$$

where $S(x)$ is the scalar order parameter, u_0 is a positive constant, $\tau_0 \sim |T - T_c|/T_c$, T_c is the phase transition temperature, $u_{\alpha\beta}$ is the strain tensor, a_1 and a_2 are the elastic constants of the crystal, and a_3 is the quadratic striction parameter. Let us change to the Fourier transforms of the variables in Eq. (1) and perform integration with respect to the components depending on the nonfluctuating variables, which do not interact with the order parameter $S(x)$. Then, introducing, for convenience, the

new variable $y(x) = \sum_{\alpha=1}^{3} u_{\alpha\alpha}(x)$, we obtain the Hamiltonian of the system in the form

$$\begin{aligned} H_0 &= \frac{1}{2}\int d^D q(\tau_0 + q^a) S_q S_{-q} \\ &+ \frac{u_0}{4!}\int d^D q_i S_{q1} S_{q2} S_{q3} S_{-q1-q2-q3} \\ &+ a_3 \int d^D q y_{q1} S_{q2} S_{-q1-q2} + \frac{a_3^{(0)}}{\Omega} y_0 \int d^D q S_q S_{-q} \\ &+ \frac{1}{2} a_1 \int d^D q y_q y_{-q} + \frac{1}{2}\frac{a_1^{(0)}}{\Omega} y_0^2. \end{aligned} \tag{2}$$

In Eq. (2), the components y_0 describing the homogeneous strains are separated. According to [1], such a separation is necessary, because the inhomogeneous strains y_q are responsible for the acoustic phonon exchange and lead to long-range interactions, which are absent in the case of homogeneous strains.

For the system under study, let us determine the effective Hamiltonian that depends only on the strongly fluctuating order parameter S:

$$\exp\{-H[S]\} = B\int \exp\{-H_R[S, y]\} \prod dy_q. \tag{3}$$

If the experiment is performed at constant volume, y_0 is a constant and the integration in Eq. (3) is performed with respect to only the inhomogeneous strains, while the homogeneous strains do not contribute to the effective Hamiltonian. If the experiment occurs at constant pressure, the term $P\Omega$ is added to the Hamiltonian, the volume is represented in terms of the strain tensor components as

$$\Omega = \Omega_0\left[1 + \sum_{\alpha=1} u_{\alpha\alpha} + \sum_{\alpha\neq\beta} u_{\alpha\alpha}u_{\beta\beta} + O(u^3)\right], \tag{4}$$

and the integration in Eq. (3) is performed with respect to the homogeneous strains as well. According to [11], the inclusion of quadratic terms in Eq. (4) may be important when dealing with high pressures and crystals with large striction effects. The neglect of these quadratic terms restricts the applicability of the results obtained by Larkin and Pikin [1] to the case of low pressures. Thus, the Hamiltonian has the form

$$\begin{aligned} H &= \frac{1}{2}\int d^D q(\tau_0 + q^a) S_q S_{-q} \\ &+ \left(\frac{u_0}{4!} - \frac{z_0}{2}\right)\int d^D\{q_i\} S_{q1} S_{q2} S_{q3} S_{-q1-q2-q3} \\ &+ \frac{1}{2\Omega}(z_0 - w_0)\int d^D\{q_i\} S_{q1} S_{-q1} S_{q2} S_{-q2}, \\ z_0 &= a_1^2/(4a_3), \quad w_0 = a_1^{(0)2}/(4a_3^{(0)}). \end{aligned} \tag{5}$$

The effective interaction parameter $v_0 = u_0 - 12z_0$ that appears in the Hamiltonian due to striction effects, which are determined by the parameter z_0, can take not only positive but also negative values. As a result, the Hamiltonian describes both first-order and second-order phase transitions. At $v_0 = 0$, the system exhibits a tricritical behavior. In its turn, the effective interaction determined in Hamiltonian (5) by the parameter difference $z_0 - w_0$ may cause a second-order phase transition in the system when $z_0 - w_0 > 0$ and a first-order phase transition when $z_0 - w_0 < 0$. This form of the effective Hamiltonian suggests that a higher order critical point can be realized in the system as the point of intersection of the tricritical curves when the conditions $v_0 = 0$ and $z_0 = w_0$ are simultaneously satisfied [2]. It should be noted that, with the tricritical condition $z_0 = w_0$, Hamiltonian (5) of the model under consideration is isomorphic with the Hamiltonian of a rigid homogeneous system.

In the framework of the field-theoretical approach [12], the asymptotic critical behavior and the structure of the phase diagrams in the fluctuation region are determined by the Callan–Symanzik renormalization group equation for the vertex parts of the irreducible Green functions. To calculate the β and γ functions as the functions involved in the Callan–Symanzik equation for renormalized interaction vertices u, a_1, and $a_1^{(0)}$, or complex vertices $z = a_1^2/4a_3$, $w = a_1^{(0)2}/4a_3^{(0)}$, and $v = u - 12z$, which are more convenient for the determination of critical and tricritical behavior, a standard method based on the Feynman diagram technique and on the renormalization procedure [13] was used with the propagator $G_0(\mathbf{k}) = 1/(\tau + |\mathbf{k}|^a)$. As a result, the following expressions were obtained for the β and γ functions in the two-loop approximation:

$$\beta_v = -(4-D)v\left[1 - 36vJ_0 + 1728\left(2J_1 - J_0^2 - \frac{2}{9}G\right)v^2\right],$$

$$\beta_z = -(4-D)z\left[1 - 24vJ_0 - 2zJ_0 + 576\left(2J_1 - J_0^2 - \frac{2}{3}G\right)v^2\right],$$

$$\beta_w = -(4-D)w\left[1 - 24vJ_0 - 4zJ_0 + 2wJ_0 + 576\left(2J_1 - J_0^2 - \frac{2}{3}G\right)v^2\right],$$

$$\gamma_t = (4-D)\left[-12vJ_0 - 2zJ_0 + 2wJ_0 + 288\left(2J_1 - J_0^2 - \frac{1}{3}G\right)v^2\right],$$
$$\gamma_\varphi = (4-D)96Gv^2,$$
$$J_1 = \int \frac{d^Dq\,d^Dp}{(1+|\mathbf{q}|^a)^2(1+|\mathbf{p}|^a)(1+|q^2+p^2+2\mathbf{pq}|^{a/2})},$$
$$J_0 = \int \frac{d^Dq}{(1+|\mathbf{q}|^a)^2},$$
$$G = -\frac{\partial}{\partial|\mathbf{k}|^a}\int \frac{d^Dq\,d^Dp}{(1+|q^2+k^2+2\mathbf{kq}|^a)(1+|\mathbf{p}|^a)(1+|q^2+p^2+2\mathbf{pq}|^{a/2})}. \quad (6)$$

Redefining the effective interaction vertices as

$$v = \frac{v}{J_0}, \quad z = \frac{z}{J_0}, \quad w = \frac{w}{J_0}, \quad (7)$$

we arrive at the following expressions for the β and γ functions:

$$\beta_v = -(4-D)v\left[1 - 36v + 1728\left(2\tilde{J}_1 - 1 - \frac{2}{9}\tilde{G}\right)v^2\right],$$
$$\beta_z = -(4-D)$$
$$\times z\left[1 - 24v - 2z + 576\left(2\tilde{J}_1 - 1 - \frac{2}{3}\tilde{G}\right)v^2\right],$$
$$\beta_w = -(4-D)w\left[1 - 24v - 4z + 2w + 576\left(2\tilde{J}_1 - 1 - \frac{2}{3}\tilde{G}\right)v^2\right],$$
$$\gamma_t = (4-D)$$
$$\times\left[-12v - 2z + 2w + 288\left(2\tilde{J}_1 - 1 - \frac{1}{3}\tilde{G}\right)v^2\right],$$
$$\gamma_\varphi = (4-D)96\tilde{G}v^2. \quad (8)$$

The redefining procedure makes sense for $a \le D/2$. In this case, J_0, J_1, and G become divergent functions. Introducing the cutoff parameter Λ and considering the ratios

$$\frac{J_1}{J_0^2} = \frac{\int_0^\Lambda\int_0^\Lambda d^Dq\,d^Dp/((1+|\mathbf{q}|^a)^2(1+|\mathbf{p}|^a)(1+|q^2+p^2+2\mathbf{pq}|^{a/2}))}{\left[\int_0^\Lambda d^Dq/(1+|\mathbf{q}|^a)^2\right]^2},$$
$$\frac{G}{J_0^2} = \frac{-\partial/(\partial|\mathbf{k}|^a)\int_0^\Lambda\int_0^\Lambda d^Dq\,d^Dp/((1+|q^2+k^2+2\mathbf{kq}|^a)(1+|\mathbf{p}|^a)(1+|q^2+p^2+2\mathbf{pq}|^a))}{\left[\int_0^\Lambda d^Dq/(1+|\mathbf{q}|^a)^2\right]^2} \quad (9)$$

in the limit of $\Lambda \longrightarrow \infty$, we obtain finite expressions.

The values of the integrals were determined numerically. For the case $a \le D/2$, a sequence of the values of J_1/J_0^2 and G/J_0^2 was constructed for different Λ and then approximated to infinity.

It is well known that perturbative series expansions are asymptotic and the interaction vertices of the order parameter fluctuations in the fluctuation region are sufficiently large to directly apply Eqs. (8). Therefore, to extract the necessary physical information from the expressions derived above, the Padé–Borel method

Table

No.	v^*	z^*	w^*	b_1	b_2	b_3	ν	η
				$a = 1.9$				
1	0.042067	0	0	0.684	−0.184	−0.184	0.620054	0.013420
2	0.044353	0.095190	0	0.684	0.185	0.183	0.713861	0.013420
3	0.044353	0.095190	0.095190	0.684	0.185	−0.185	0.620054	0.013420
4	0	0.5	0	–1	1	1	1	0
5	0	0.5	0.5	–1	1	–1	0.5	0
				$a = 1.8$				
1	0.023230	0	0	0.628	−0.488	−0.488	0.572714	0.007461
2	0.023230	0.245404	0	0.628	0.489	0.490	0.704621	0.007461
3	0.023230	0.245404	0.245404	0.628	0.489	−0.489	0.572714	0.007461
4	0	0.5	0	–1	1	1	1	0
5	0	0.5	0.5	–1	1	–1	0.5	0
				$a = 1.7$				
1	0.020485	0	0	0.699	−0.532	−0.532	0.567334	0.004862
2	0.020485	0.266497	0	0.699	0.533	0.532	0.706051	0.004862
3	0.020485	0.266497	0.266497	0.699	0.533	−0.533	0.567334	0.004862
4	0	0.5	0	–1	1	1	1	0
5	0	0.5	0.5	–1	1	–1	0.5	0
				$a = 1.6$				
1	0.015974	0	0	0.874	−0.616	−0.616	0.557889	0.003936
2	0.015974	0.309684	0	0.874	0.617	0.620	0.711578	0.003936
3	0.015974	0.309684	0.309684	0.874	0.617	−0.618	0.557889	0.003936
4	0	0.5	0	–1	1	1	1	0
5	0	0.5	0.5	–1	1	–1	0.5	0
				$a = 1.5$				
1	0.015151	0	0	0.919	−0.635	−0.635	0.555566	0.002647
2	0.015151	0.316966	0	0.919	0.636	0.630	0.712195	0.002647
3	0.015151	0.316966	0.316966	0.919	0.636	−0.636	0.555566	0.002647
4	0	0.5	0	–1	1	1	1	0
5	0	0.5	0.5	–1	1	–1	0.5	0

generalized to the three-parameter case was used. The corresponding direct and inverse Borel transformations have the form

$$f(v, z, w) = \sum_{i_1, i_2, i_3} c_{i_1, i_2, i_3} v^{i_1} z^{i_2} w^{i_3}$$
$$= \int_0^\infty e^{-t} F(vt, zt, wt) dt, \qquad (10)$$
$$F(v, z, w) = \sum_{i_1, i_2, i_3} \frac{c_{i_1, i_2, i_3}}{(i_1 + i_2 + i_3)} v^{i_1} z^{i_2} w^{i_3}.$$

For an analytical continuation of the Borel transform of a function, a series in an auxiliary variable θ is introduced:

$$\tilde{F}(v, z, w, \theta)$$
$$= \sum_{k=0}^{\infty} \theta^k \sum_{i_1, i_2, i_3} \frac{c_{i_1, i_2, i_3}}{k!} v^{i_1} z^{i_2} w^{i_3} \delta_{i_1 + i_2 + i_3, k}, \qquad (11)$$

and the [L/M] Padé approximation is applied to this series at the point θ = 1. This approach was proposed and tested in [14] in describing the critical behavior of systems characterized by several vertices of interaction of the order parameter fluctuations. The property [14] of the system retaining its symmetry under the Padé

approximants in the variable θ is essential in the description of multivertex models.

In the two-loop approximation, the β functions were calculated using the [2/1] approximant. The character of the critical behavior is determined by the existence of a stable fixed point satisfying the set of equations

$$\beta_i(v^*, z^*, w^*) = 0 \quad (i = 1, 2, 3). \tag{12}$$

The requirement that the fixed point be stable is reduced to the condition that the eigenvalues b_i of the matrix

$$B_{i,j} = \frac{\partial \beta_i(u_1^*, u_2^*, u_3^*)}{\partial u_j} \quad (u_i, u_j \equiv v, z, w) \tag{13}$$

lie in the half-plane of the right-hand complex. The fixed point with $v^* = 0$, which corresponds to the tricritical behavior, is a saddle point and must be stable in the directions determined by the variables z and w and unstable in the direction determined by the variable v. The stabilization of the tricritical fixed point in the direction determined by the variable v is achieved by taking into account the sixth-order terms with respect to the order parameter fluctuations in the effective Hamiltonian of the model. The fixed point with $z^* = w^*$, which corresponds to the tricritical behavior of the second type, is also a saddle point and must be stable in the directions determined by the variables v and z and unstable in the direction determined by the variable w. Its stabilization is possible at the expense of the anharmonic effects.

The resulting set of the resummed β functions contains a wide variety of fixed points. The table specifies the fixed points that are of most interest for describing the critical and tricritical behavior and lie in the physical region of vertex values with $v, z, w \geq 0$. The table also shows the eigenvalues of the stability matrix for the corresponding fixed points and the critical indices ν and η.

The analysis of the values and stability of the critical points suggests the following conclusions. Qualitatively, the critical phenomena seem to be identical for any value of the long-range interaction parameter a. The critical behavior of incompressible systems is unstable with respect to the deformation degrees of freedom (points 1). The stable point proves to be the one at a constant strain (points 2). Fixed points 3 describe the first type of tricritical behavior of compressible systems, which occurs at constant pressure. Fixed points 4 are tricritical for systems studied at constant volume. Points 5 are fourth-order critical points at which two tricritical curves intersect.

For the tricritical behavior of the first type (points 3), Hamiltonian (5) is isomorphic with the Hamiltonian of an incompressible homogeneous model and, hence, the critical indices also coincide with those of the incompressible model. The tricritical behavior of the second type (points 4) corresponds to the critical behavior of a spherical model and is determined by the corresponding indices. The fourth-order fixed points (points 5) are characterized by the field-average values of the critical indices.

The large values of the effective vertices z and w in comparison with the systems with short-range interactions [3] are caused by the fact that the mechanism governing the effect of elastic deformations on the critical phenomena is related to the dependence of the interaction integral in the Ising model on the distance between the lattice sites.

The study described above revealed the considerable effect of elastic deformations on the critical behavior of systems with a long-range interaction. This effect manifests itself as a change in the values of the critical indices for Ising systems along with the appearance of multicritical points in the phase diagrams of the substances.

REFERENCES

1. A. I. Larkin and S. A. Pikin, Zh. Éksp. Teor. Fiz. **56**, 1664 (1969) [Sov. Phys. JETP **29**, 891 (1969)].
2. Y. Imry, Phys. Rev. Lett. **33** (21), 1304 (1974).
3. S. V. Belim and V. V. Prudnikov, Fiz. Tverd. Tela (St. Petersburg) **43**, 1299 (2001) [Phys. Solid State **43**, 1353 (2001)].
4. M. E. Fisher, S.-K. Ma, and B. G. Nickel, Phys. Rev. Lett. **29**, 917 (1972).
5. J. Honkonen, J. Phys. A **23**, 825 (1990).
6. E. Luijten and H. Mebingfeld, Phys. Rev. Lett. **86**, 5305 (2001).
7. E. Bayong and H. T. Diep, Phys. Rev. B **59**, 11 919 (1999).
8. E. Luijten, Phys. Rev. E **60**, 7558 (1999).
9. E. Luijten and H. W. J. Bloöte, Phys. Rev. B **56**, 8945 (1997).
10. S. V. Belim, Pis'ma Zh. Éksp. Teor. Fiz. **77**, 118 (2003) [JETP Lett. **77**, 112 (2003)].
11. D. J. Bergman and B. I. Halperin, Phys. Rev. B **13**, 2145 (1976).
12. D. Amit, *Field Theory the Renormalization Group and Critical Phenomena* (McGraw-Hill, New York, 1976).
13. J. Zinn-Justin, *Quantum Field Theory and Critical Phenomena* (Clarendon Press, Oxford, 1989).
14. A. I. Sokolov and K. B. Varnashev, Phys. Rev. B **59**, 8363 (1999).

Translated by E. Golyamina

JETP Letters, Vol. 77, No. 10, 2003, pp. 561–564. Translated from Pis'ma v Zhurnal Éksperimental'noĭ i Teoreticheskoĭ Fiziki, Vol. 77, No. 10, 2003, pp. 664–667.
Original Russian Text Copyright © 2003 by Efanov, Zhuravlev, Shamirzaev, Kellner, Pasher.

Observation of Exchange Interaction Effects under Optical Orientation of Excitons in AlGaAs

A. V. Efanov*, K. S. Zhuravlev*, T. S. Shamirzaev*, W. Kellner, and H. Pasher****

** Institute of Semiconductor Physics, Siberian Division, Russian Academy of Sciences, Novosibirsk, 630090 Russia*
e-mail: zhur@thermo.isp.nsc.ru
*** Physikalisches Institut, Universität, Bayreuth, Germany*

Received March 27, 2003

Exciton luminescence in AlGaAs layers is studied under interband excitation by circularly polarized light. Curves of luminescence depolarization in a transverse magnetic field (Hanle effect) exhibit peaks arranged symmetrically about a point $H = 0$. It is shown that this effect is attributable to crossings of fine-structure levels in the magnetic field. The exchange splitting of bulk exciton levels and also recombination and spin-relaxation times are determined from a comparison between theoretical and experimental dependences. © *2003 MAIK "Nauka/Interperiodica".*

PACS numbers: 71.35.Ji; 72.25.Rb

In recent years, effects of the fine structure in exciton levels in systems of low dimensionality have been studied intensively [1, 2]. The exchange splitting in such systems is considerably increased as compared to the bulk case as a result of a larger overlap between electron and hole wave functions. Owing to this fact, various manifestations of the fine structure can be observed at not-too-low temperatures. In this work, such effects were observed for bulk excitons in $Al_xGa_{1-x}As$ crystals under nonresonant excitation with circularly polarized light.

This work is devoted to studying the transverse magnetic field effects on the degree of the circular polarization of exciton luminescence (Hanle effect) in high-purity samples of $Al_xGa_{1-x}As$. The layers were grown by molecular-beam epitaxy on semiinsulating GaAs substrates with a (100) orientation using a Riber-32P setup. The Al content varied within the range $0.09 < x < 0.295$. The layer thickness was 2.5 mm. To decrease surface recombination, the layers were coated with buffer AlAs layers 25 nm thick. The details of the growth procedure were described in our previous work [3].

The measurements were performed at a superfluid helium temperature of 1.6 K. Steady-state luminescence was excited with a He–Ne laser with a power density of order 3 W/cm^2. The sign of the circular polarization was reversed using an electro-optical modulator in the range of frequencies from 100 Hz to 100 kHz. Luminescence was measured in the back-scattering geometry at a fixed position of the analyzer using a monochromator with a focal distance of 0.64 m. The monochromator was connected to a dual-channel photon counter synchronized with the modulator.

The free-exciton line predominated in all the luminescence spectra [3]. The circular-polarization degree of luminescence was measured at the line maximum. The Hanle curves were measured in $Al_xGa_{1-x}As$ samples with x = 0.09, 0.15, and 0.21 (Fig. 1). In the absence of a magnetic field, the circular-polarization degree of luminescence for all samples comprised a value of order 8% (curves for $x = 0.09$ and $x = 0.15$ are shifted in vertical). In the measurements, the polariza-

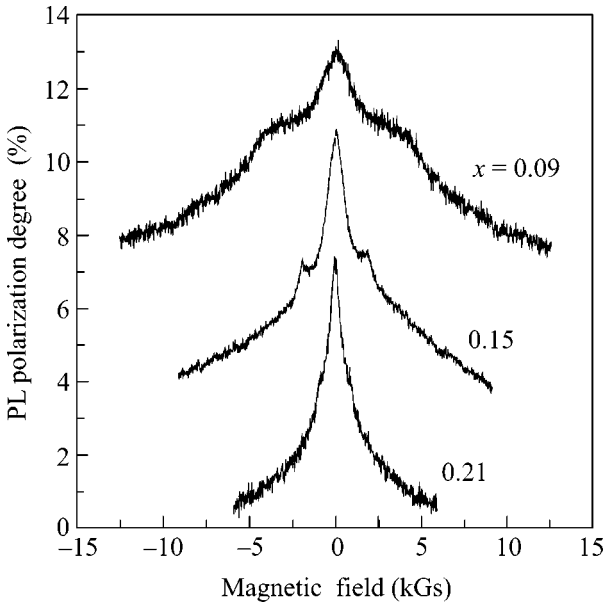

Fig. 1. Dependence of the circular-polarization degree of luminescence P_c on the magnetic field in $Al_xGa_{1-x}As$ samples with compositions x = 0.09, 0.15, and 0.21 (curves with x = 0.09 and 0.21 are shifted in vertical).

tion of the exciting light was reversed with a frequency of 1 kHz. For the compositions indicated above, the sign of the electron *g*-factor ranged over the region of both positive and negative values.

It is evident in Fig. 1 that the Hanle curves are intricate in shape. They represent a superposition of two contours with widths differing approximately by a factor of 10. Two additional peaks arranged symmetrically about the zero magnetic field are observed for the composition $x = 0.15$. These peaks are not associated with the dynamic polarization of nuclei, because measurements at a frequency of 100 kHz do not change the shape of the curves. In the sample with $x = 0.21$, the peaks are not clearly defined and weak deviations from the monotonic behavior of the curves are observed in their place. In the sample with $x = 0.09$, a broad "pad" is observed instead of peaks.

The following model was used to account for the results obtained. We assumed that the main part of excitons is formed through a bimolecular mechanism as a result of coupling of free electrons and holes. By virtue of the experimental conditions, the intensities of photoexcitation cannot be weak. For this reason, the formation of hot excitons through the geminate (pump-linear) mechanism, in this case, turns out to be less efficient. It was suggested that luminescence at a low temperature is determined by bound excitons grouped in the tail region of the density of states, which is associated with composition fluctuations in a disordered solid solution.

The pattern of the luminescence spectrum formation in a disordered solid solution, in the general case, is rather intricate [4, 5]. In this work, it is suggested that the exciton centers of mass are localized in fluctuation wells. In this case, the internal structure of an exciton wave function can be close to the state of a free exciton. The smallness of the line width of exciton luminescence, which comprises about 1 meV in the experiment, corroborates the suggestion that the potential fluctuations are weak.

In the proposed model, the spin orientation of excitons arises in the course of a two-stage cascade process. At the first stage, free electrons and holes are generated through direct interband optical transitions. Depending on the composition of the solid solution, at a fixed pumping frequency, the kinetic energy of photoexcited excitons in the conduction band falls into either the passive band or the band lying higher than the passive band by a value of up to ten energies of optical phonons. Under these conditions, electrons retain their spin orientation during energy relaxation. In the opposite case, photogenerated holes lose it completely.

Excitons are formed at the second, slower stage of the cascade. In our samples, a radiationless recombination channel is virtually absent [3]. For this reason, the lifetime of free carriers is fully determined by the process of their escape to excitons. During the coupling of electrons and holes to excitons, the electrons themselves do not lose their spin orientation.

With the suggestions indicated above, the dynamics of the electron spin $\mathbf{S}_e$ is described by the equation

$$\frac{d\mathbf{S}_e}{dt} = \mathbf{\Omega}_e \times \mathbf{S}_e - \frac{\mathbf{S}_e}{T_e} + \mathbf{s}_e G, \tag{1}$$

where G is the photogeneration intensity, $\mathbf{s}_e$ is the vector of the average spin of a photoexcited electron, $\Omega_e = g_e \mu_B \mathbf{B}/\hbar$, μ_B is the Bohr magneton, and g_e is the gyromagnetic ratio. The relaxation time T_e is determined by the equation $T_e^{-1} = \tau_b^{-1} + \tau_{es}^{-1}$, where τ_b is the exciton coupling time and τ_{es} is the electron spin relaxation time. The steady-state number of electrons N_e in the absence of the thermal dissociation of electrons is given by the equation $N_e = \tau_b G$.

The kinetics of bound excitons will be described with the use of the density matrix formalism [6]. The Hamiltonian of an exciton in the magnetic field H is taken in the form

$$H = \frac{\Delta}{4}(\mathbf{J}^2 - 2) + \frac{1}{2}\mu_B(g_e \boldsymbol{\sigma}\mathbf{H} + 2g_h \mathbf{j}\mathbf{H}). \tag{2}$$

Here, g_e and g_h are *g*-factors of electrons and holes, $\mathbf{j}$ is the angular momentum operator of a hole ($j = 3/2$), $\boldsymbol{\sigma}$ are the Pauli matrices, $\mathbf{J}$ is the total angular momentum operator of an exciton, and Δ is the exchange splitting between exciton levels with total angular momenta $J = 1, 2$.

The equation for the density matrix of an exciton ρ has the structure

$$-\left(\frac{\partial \rho}{\partial t}\right)^r - \left(\frac{\partial \rho}{\partial t}\right)^s + \frac{i}{\hbar}[H, \rho] = \tilde{G}. \tag{3}$$

The first term on the left-hand side takes into account recombination. This term involves τ_1 and τ_2 twice for levels with $J = 1, 2$ and the nondiagonal relaxation time defined by the equation $\tau_{12}^{-1} = (\tau_1^{-1} + \tau_2^{-1})/2$. By analogy with [6], we suggest that the exciton spin relaxes mainly through fluctuations of the hole spin. Correspondingly, the second term in Eq. (3) is characterized by only one time τ_s. In the above approach, it is assumed that temperature is high compared to Δ.

The matrix $\tilde{G}$ in Eq. (3) describes the generation of excitons. In accordance with the model assumed above, it can be taken in the form of the product of the density matrix of nonpolarized holes by the density matrix of electrons

$$\tilde{G} = \frac{1}{8}G(1 + 2\mathbf{s}\boldsymbol{\sigma}). \tag{4}$$

Here, $\mathbf{s} = \mathbf{S}_e/N_e$ is a vector numerically equal to the average spin of a free electron. As distinct from [6], we take into account the rotation of this vector in the magnetic field, which is determined by Eq. (1).

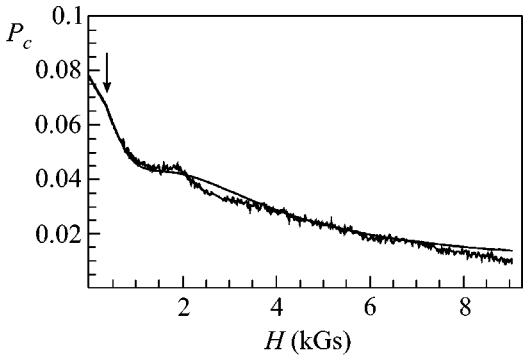

Fig. 2. Experimental and theoretical dependences $P_c(H)$ for $x = 0.15$ (curve with noise is experimental). The arrow shows the place at which the slope of the curves changes.

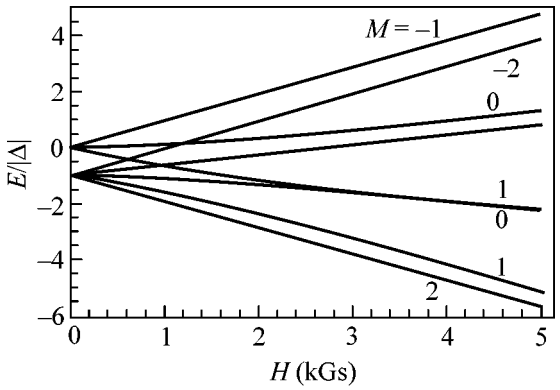

Fig. 3. Splitting of exciton levels in a magnetic field. Graphs are constructed for $g_e = 0.1$, $g_h = -2$, and $\Delta = -18$ μeV.

Based on the proposed model, we performed numerical calculations of the circular-polarization degree of luminescence P_c in a transverse magnetic field. From the very start, the relaxation broadening of levels $\hbar/\tau$ was suggested, where $\tau^{-1} \sim \tau_1^{-1} + \tau_s^{-1}$ is sufficiently small compared to the exchange splitting Δ. In this case, details of the fine structure can be revealed. The following relation among times was considered: $\tau_1 \sim \tau_s \ll \tau_2$. For the spin of photoexcited electrons, the highest possible value of $s_e = -0.5$ was taken.

The calculated results for the solid solution with $x = 0.15$ are presented in Fig. 2. The initial part of the curve, including the side peak, corresponds to exciton depolarization. The strong-field region corresponds to the precession of the free-electron spin. This circumstance seems rather unconventional, because the lifetime and the spin relaxation time are usually sufficiently long (>1 ns). On the contrary, it is the central peak that should be associated with electrons. In fact, here the small value of the electron g-factor plays an essential part: $g_e \approx 0.1$ at $x = 0.15$ [7]. The estimate of the characteristic width of the Lorentzian tail δH involves the product $g_e\mu_B T_e \delta H/\hbar \sim 1$, and, thus, the large value of T_e is partially compensated by the smallness of g_e.

We relate the increase in luminescence polarization at a finite field to the convergence or crossing (depending on the sign of the g_e factor) of a certain group of exciton levels. The corresponding curves are constructed in Fig. 3 in the case of $x = 0.15$. The spectrum of the Hamiltonian (Eq. (2)) is found in an analytical form. Its levels are classified by the projection of the total angular momentum M onto the magnetic field. It is evident in the figure that the pair of levels with $M = 0$ and $M = 1$, originating, correspondingly, from the states with the total angular momenta $J = 2$ and $J = 1$, approach each other in the peak region in a zero magnetic field. Under certain conditions, the above levels make the main contribution of to the degree of luminescence polarization.

The mechanism of this phenomenon can be clarified in the simplest case when the recombination times are equal, that is, $\tau_1 = \tau_2 = \tau$. The solution of the equation for the density matrix in this case can be written explicitly. The elements of the density matrix calculated from the exact wave function of their levels of the Hamiltonian (Eq. (2)) with the energies ε_1 and ε_2 are proportional to $\rho_{12} \sim [i(\varepsilon_1 - \varepsilon_2) + \hbar/T]^{-1}$, where $T^{-1} = \tau^{-1} + \tau_s^{-1}$. These values are calculated in the basis set of states with a certain projection of the angular momentum of the exciton onto the magnetic field. For this reason, the density matrix elements diagonal in their level number make no contribution to the circular luminescence polarization in the direction perpendicular to the magnetic field. The luminescence polarization is determined solely by the nondiagonal elements, whose values depend on the distance between the levels $\Delta\varepsilon = |\varepsilon_1 - \varepsilon_2|$. If this distance for a particular pair of levels is smaller than the parameter $\hbar/T$ and all the other levels are separated by a considerably larger distance, then, according to the parameter $\hbar/\Delta\varepsilon T \ll 1$ the contribution of the latter to polarization turns out to be small.

The calculation shows that a broad side peak must appear at a fixed orientation of the free electron spin $\mathbf{S}_e$. The large extension of this peak is caused by the smallness of the electron g-factor. Taking into account the rotation of the free electron spin in the magnetic field considerably decreases the peak width. However, the obtained decay rate of polarization is slower than in the experimental curves. The faster decay of polarization compared to the calculated rate could be associated with the processes of relaxation acceleration during large level splitting, which are not taken into account in the proposed model.

A comparison between the experimental and theoretical dependences for the sample with $x = 0.15$ gives the value $\Delta \approx 18$ μeV, which is in agreement with the known data for the short-range part of the exchange splitting in the bulk exciton [8]. The obtained exciton recombination times are equal to $\tau_1 = 50$ ps and $\tau_2 =$

4 ns, and the spin relaxation time is τ_s = 60 ps. In the field determined by the estimate $g_h\mu_B H\tau_s/\hbar \sim 1$ (indicated by an arrow in Fig. 2), a characteristic kink is observed in the region of the central peak of the Hanle curve. Here, the change in the curve slope corresponds to the transition between two approximate asymptotes, considered in [6] in the case of a large exchange splitting of exciton levels $\Delta \gg \hbar/T$ and $\tau_1 < \tau_s \ll \tau_2$. Calculation with the approximate equations [6] describes well the Hanle curves in a weak field.

The electron relaxation times are found to be τ_b = 0.9 ns and τ_{es} = 2.1 ns. The obtained value of the electron lifetime τ_b agrees with the fact that the case when the density of electron–hole pairs is not too low takes place in the experiment. It is for this case that long-term exciton luminescence decay is usually observed in the samples under study.

Note that the measured spin relaxation time can apparently characterize the processes of energy relaxation of excitons in the region below the mobility edge. In this region, processes of radiative recombination and phonon-assisted hopping down in energy through exciton tunneling between localized states are in competition [5]. During inelastic tunneling, hole spin relaxation inevitably proceeds because of spin–orbit interaction in the valence band.

In the sample with x = 0.09, g_e = –0.07. The best agreement with the experimental curves is obtained at Δ = 15 μeV and relaxation times τ_1 = 30 ps and τ_s = 50 ps. In this case, because of the smallness of the electron *g*-factor and the shorter exciton lifetime, the structure with a side peak smears out into a broad "pad" under the central peak. In the sample with x = 0.21, g_e = 0.2. Good agreement is obtained at Δ = 8 μeV, τ_1 = 60 ps, and τ_s= 110 ps. At this value of the *g*-factor, the crossing region of the group of levels mentioned above lies in a weak field, where the contribution of all other Zeeman levels has already become notable. The reason for the wide scatter in the value of Δ in the samples under study is not clear and calls for detailed investigation.

In conclusion, it can be noted that manifestations of the fine structure of a bulk exciton were observed in this work using the optical orientation method and the value of exchange splitting was calculated independently.

This work was supported by the Russian Foundation for Basic Research, project no. 01-02-16967.

REFERENCES

1. S. V. Gupalov and E. L. Ivchenko, Fiz. Tverd. Tela (St. Petersburg) **42**, 1976 (2000) [Phys. Solid State **42**, 2030 (2000)].
2. E. Blackwood, M. J. Snelling, and R. T. Harley, Phys. Rev. B **50**, 14246 (1994).
3. K. S. Zhuravlev, A. I. Toropov, T. S. Shamirzaev, and A. K. Bakarov, Appl. Phys. Lett. **76**, 1131 (2000).
4. A. A. Klochikhin, S. A. Permogorov, and A. N. Reznitskiĭ, Fiz. Tverd. Tela (St. Petersburg) **39**, 1170 (1997) [Phys. Solid State **39**, 1035 (1997)].
5. L. E. Golub, S. V. Ivanov, E. L. Ivchenko, *et al.*, Phys. Status Solidi B **205**, 203 (1998).
6. G. E. Pikus and G. L. Bir, Zh. Éksp. Teor. Fiz. **67**, 788 (1974) [Sov. Phys. JETP **40**, 390 (1974)].
7. C. Weisbuch and C. Hermann, Phys. Rev. B **15**, 816 (1977).
8. W. Ekardt, K. Lösch, and D. Bimberg, Phys. Rev. B **20**, 3303 (1979).

Translated by A. Bagatur'yants

JETP Letters, Vol. 77, No. 10, 2003, pp. 565–566. Translated from Pis'ma v Zhurnal Éksperimental'noĭ i Teoreticheskoĭ Fiziki, Vol. 77, No. 10, 2003, pp. 668–669.
Original Russian Text Copyright © 2003 by Marchenko, Podolyak.

On the Penetration Depth of a Strong Field into Superconductors

V. I. Marchenko* and E. R. Podolyak

Kapitsa Institute for Physical Problems, Russian Academy of Sciences, ul. Kosygina 2, Moscow, 117334 Russia

**e-mail: mar@kapitza.ras.ru*

Received April 2, 2003

The field dependence of the magnetic penetration depth over the entire range of stability and metastability of the Meissner state was determined within the framework of the Ginzburg–Landau theory. A simple interpolation formula is suggested. © *2003 MAIK "Nauka/Interperiodica".*

PACS numbers: 74.25.Ha; 74.20.De; 74.25.Op

Ginzburg and Landau [1] calculated the low-field correction to the magnetic penetration depth for an arbitrary value of the parameter κ:

$$\delta(H) = \delta(0)\left(1 + \frac{\kappa(\kappa + 2\sqrt{2})}{8(\kappa + \sqrt{2})^2}\frac{H^2}{H_c^2}\right). \quad (1)$$

In the limiting cases of large and small κ values, Eq. (1) is valid over the entire domain of existence of the equilibrium Meissner state (up to the field H_c in type-I superconductors and H_{c1} in type-II superconductors).

In type-I superconductors, an normal metal–superconductor transition in an external magnetic field is a phase transition of the first order. It can be accompanied by superheating or supercooling. In type-II superconductors, the process of superconductivity destruction involves a stage, during which the superconductor is in a mixed state. The transition from the normal to the mixed state in the field H_{c2} is a classical phase transition of the second order. The occurrence of the mixed state in a superconductor exposed to an external field H_{c1}, as well as its reconstruction in a varying magnetic field, should be accompanied by superheating or supercooling even in the absence of pinning. This is caused by the Bean–Livingston energy barrier to vortex penetration into superconductors [2]. In the limit of large values of the Ginzburg–Landau parameter, the barrier to vortex penetration disappears in a field $H_m = H_c$ (see [3], §34) that considerably exceeds the field H_{c1}, in which the transition to the mixed state occurs.

A phase diagram (κ, H) for superconductors near the transition temperature, where the Ginzburg–Landau theory is valid, is shown in Fig. 1. The highest possible superheating field $H_m(\kappa)$ for the Meissner state was determined by Ginzburg [4], who numerically solved the Ginzburg–Landau equations.

In the limit of large κ values, Ginzburg [4] obtained an analytical solution to the problem of magnetic field decay in the superconductor bulk:

$$B = 2H_c \sinh\left(\frac{x}{\delta} + C\right)\cosh^{-2}\left(\frac{x}{\delta} + C\right), \quad (2)$$

where the constant C is a function of the external field and determined by the following equation:

$$\cosh(C) = \frac{H_c}{H}\left(\sqrt{1 + \frac{H}{H_c}} + \sqrt{1 - \frac{H}{H_c}}\right). \quad (3)$$

Ginzburg's solution determines the dependence of magnetic penetration depth

$$\delta(H) = \frac{1}{H}\int_0^\infty B\,dx$$

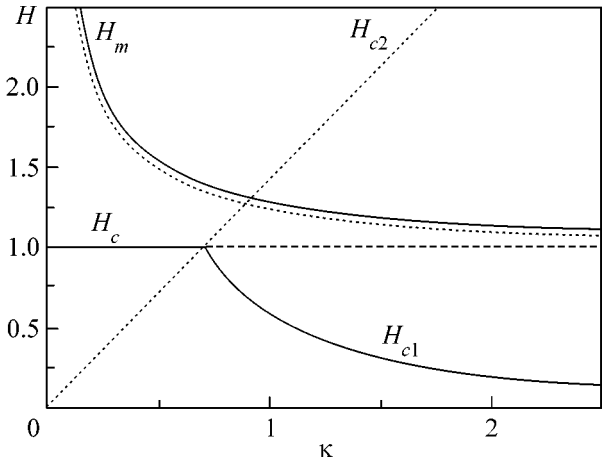

Fig. 1. Ginzburg–Landau phase diagram for superconductors. Solid curves (except H_c) for the maximal superheating field H_m and the field H_{c1} (equal to the ratio between the one-quantum vortex energy and the magnetic flux quantum) were obtained by numerical computation. The dotted curve is the function $H_{GL}(\kappa)$ given by Eq. (7).

0021-3640/03/7710-0565$24.00 © 2003 MAIK "Nauka/Interperiodica"

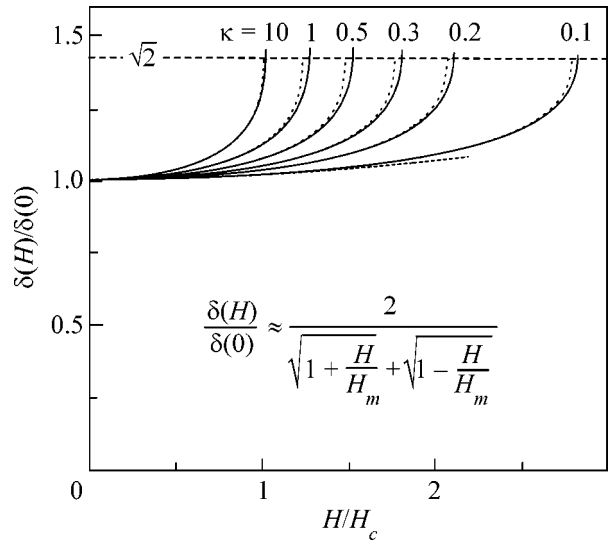

Fig. 2. Field dependence of the magnetic penetration depth for various values of the parameter κ. Solid lines are the results of a numerical solution to the Ginzburg–Landau equations. Dotted lines are interpolation functions (4). The dashed line is the Ginzburg–Landau quadratic low-field approximation (1).

on a magnetic field over the entire range $0 < H < H_m = H_c$, where the Meissner state can be observed at large values of κ:

$$\delta(H) = 2\delta(0)\left(\sqrt{1+\frac{H}{H_m}} + \sqrt{1-\frac{H}{H_m}}\right)^{-1}. \qquad (4)$$

In the limit of small κ values, the Ginzburg–Landau equation for the Meissner state was solved by Galaĭko [5]. For small κ, the presence of a magnetic field at distances greater than the penetration depth can be neglected. Then,

$$\psi = \tanh\frac{\kappa(x+a)}{\sqrt{2}}. \qquad (5)$$

The parameter a is determined by matching solution (5) and the solution near the boundary of the field penetration region.

In the approximation considered, the field penetration is described by a simple exponential function $A = H|\psi_0|^{-1}\exp(-|\psi_0|x)$. It can easily be shown, using the solution obtained in [5], that in this limit the dependence of magnetic penetration depth $\delta(H) = \psi_0^{-1}$ on the external magnetic field is also given by Eq. (4) with the superheating field H_m equal to

$$H_m = \frac{H_c}{\sqrt{\sqrt{2}\kappa}}. \qquad (6)$$

Thus, quite unexpectedly, the field dependences for the small and large values of the parameter κ were found to coincide. The numerical solution to the Ginzburg–Landau equations for an arbitrary value of κ showed that the field dependence of the penetration depth over the entire field range deviated only slightly (Fig. 2) from the interpolation function (4), where the critical superheating field for an arbitrary κ is taken to be

$$H_m = H_{GL} = H_c\frac{\kappa+\sqrt{2}}{\sqrt{\kappa^2+2\sqrt{2}\kappa}}, \qquad (7)$$

as follows from the low-field limit (1).

As the maximum superheating field is approached, both Eq. (4) and the numerical solution to the Ginzburg–Landau equations (Fig. 2) exhibit a root singularity. Such a singularity is usually indicative of loss of stability of a metastable state against uniform disturbances (see [6], part 3).

The close similarity between the results of numerical computation of the function $H_m(\kappa)$ and the curve $H_{GL}(\kappa)$ (Fig. 1), as well as the fact that the maximal increase in the penetration depth is close to $\sqrt{2}$ (Fig. 2), shows that the accuracy of the suggested interpolation formula is rather high. Thus, the superconductor parameters H_c and κ can be reliably determined from the measured field dependence of the penetration depth in bulk superconductors only in the combination entering the equation for H_{GL}. To separately determine these parameters with an accuracy of 10^{-1}, the accuracy of measuring the penetration depth should be 10^{-3} or better.

We are grateful to G.M. Éliashberg and V.F. Gantmakher, who called our attention to works [4] and [5].

This work was supported by the Russian Foundation for Basic Research, project nos. 00-02-16250 and 03-02-16958.

REFERENCES

1. V. L. Ginzburg and L. D. Landau, Zh. Éksp. Teor. Fiz. **20**, 1064 (1950).
2. C. P. Bean and J. D. Livingston, Phys. Rev. Lett. **12**, 14 (1964).
3. V. V. Shmidt, *Introduction to the Physics of Superconductors* (MTsNMO, Moscow, 2000).
4. V. L. Ginzburg, Zh. Éksp. Teor. Fiz. **34**, 113 (1958) [Sov. Phys. JETP **7**, 78 (1958)].
5. V. P. Galaĭko, Zh. Éksp. Teor. Fiz. **50**, 717 (1966) [Sov. Phys. JETP **23**, 475 (1966)].
6. V. I. Marchenko and E. R. Podolyak, Zh. Éksp. Teor. Fiz. **124** (2003) (in press).

Translated by K. Chamorovskiĭ

JETP Letters, Vol. 77, No. 10, 2003, pp. 567–570. Translated from Pis'ma v Zhurnal Éksperimental'noĭ i Teoreticheskoĭ Fiziki, Vol. 77, No. 10, 2003, pp. 670–674.
Original Russian Text Copyright © 2003 by Gulyaev, Nikitov, Zhivotovskiĭ, Klimov, Tailhades, Presmanes, Bonningue, Tsai, Vysotskiĭ, Filimonov.

Ferromagnetic Films with Magnon Bandgap Periodic Structures: Magnon Crystals

Yu. V. Gulyaev[1], S. A. Nikitov[1], L. V. Zhivotovskiĭ[1], A. A. Klimov[1], Ph. Tailhades[2], L. Presmanes[2], C. Bonningue[2], C. S. Tsai[3, 4], S. L. Vysotskiĭ[5], and Yu. A. Filimonov[5]

[1] *Institute of Radio Engineering and Electronics, Russian Academy of Sciences, Moscow, 125009 Russia*
e-mail: nikitov@cplire.ru

[2] *CIRIMAT, UMR-CNRS 5085, Universite Paul Sabatier, 31062 Toulouse, France*

[3] *Institute for Applied Sciences and Engineering Research, Academia Sinica, 11529 Taipei, Taiwan*

[4] *Department of Electrical and Computer Engineering, University of California, CA 92697, Irvine, USA*

[5] *Institute of Radio Engineering and Electronics, Saratov Branch, Russian Academy of Sciences, Saratov, 410008 Russia*

Received April 2, 2003; in final form, April 14, 2003

A new type of photonic crystals is proposed. The new crystals have a forbidden gap in the microwave spectrum of magnetostatic spin waves, and, by analogy with photonic crystals, they are called magnon crystals. Specimens of such crystals were fabricated on the basis of yttrium iron garnet films. The surfaces of ferromagnetic films containing two-dimensional etched hole structures were studied by atomic force and magnetic force magnetometry. The propagation of spin waves through the magnon crystals was investigated. © *2003 MAIK "Nauka/Interperiodica".*

PACS numbers: 42.70.Qs; 75.30.Ds; 75.70.Ak

Studies of the physical properties of photonic crystals stimulated the design of crystals intended for operation in the visible frequency range and formed on the basis of synthetic opals, colloidal particles, nanostructured films, etc. [1–4]. The properties of photonic crystals and, in particular, the presence of a photonic bandgap depend on the wavelength of propagating light. Miniature devices based on photonic crystals can be designed only for wavelengths corresponding to the visible or infrared regions. Photonic crystals with a bandgap in the rf region should be fairly large, because the corresponding electromagnetic wavelengths are on the order of several centimeters. In parallel with the development of photonic crystals, an idea was put forward to develop similar crystals whose operation is based on the propagation of magnons (spin waves) [5–11]. Such crystals should exhibit the same properties as photonic crystals, but with respect to the spin waves. The crystals similar to photonic crystals but formed on the basis of magnetic materials (namely, magnon crystals), in which spin waves can propagate, have a series of advantages over the photonic crystals. First, the spin wavelength and, hence, the properties of these crystals depend on an external magnetic field and, hence, can be controlled by it. Second, for a wide class of ferromagnetic materials, the spin-wave wavelengths in the microwave (rf) range are within tens or hundreds of microns, and, hence, it is possible to fabricate photonic (or magnon) bandgap crystals of about several millimeters in size. Moreover, such crystals can be fabricated in the planar geometry, which is important for designing integrated devices, such as narrow-band optical or microwave filters or high-speed switches. The properties of magnon crystals are, as yet, little investigated. The first publications on the crystals with a magnon bandgap only posed the problem of the existence of this kind of crystals. However, the authors of these publications recognized that the development of such crystals should be very promising and important from both scientific and practical points of view. In particular, they discussed the problem of controlling the magnon bandgap by an external magnetic field for one- and two-dimensional magnon crystals [5, 6, 8, 9]. With an appropriate choice of magnetic materials in a periodic structure, it is possible to obtain nonreciprocal magnon crystals with one-way transparence (i.e., crystals that transmit the spin waves in one direction and do not transmit them in the opposite direction) [7]. The problem of light propagation and diffraction in linear [10, 11] and nonlinear [12] magnetic photonic crystals was also considered in the literature. In particular, the cited publications considered the growth of the additive Faraday effect due to the resonant wave reflection [10] and anisotropic transformation of waveguide modes in magnetic photonic crystals.

In this paper, we discuss the possibilities of fabricating magnon crystals, report the results of an experimental realization of these crystals, and consider the prospects of their application.

The simplest one-dimensional magnon crystal is a strictly periodic multilayer structure consisting of magnetic layers with different magnetizations, or a similar

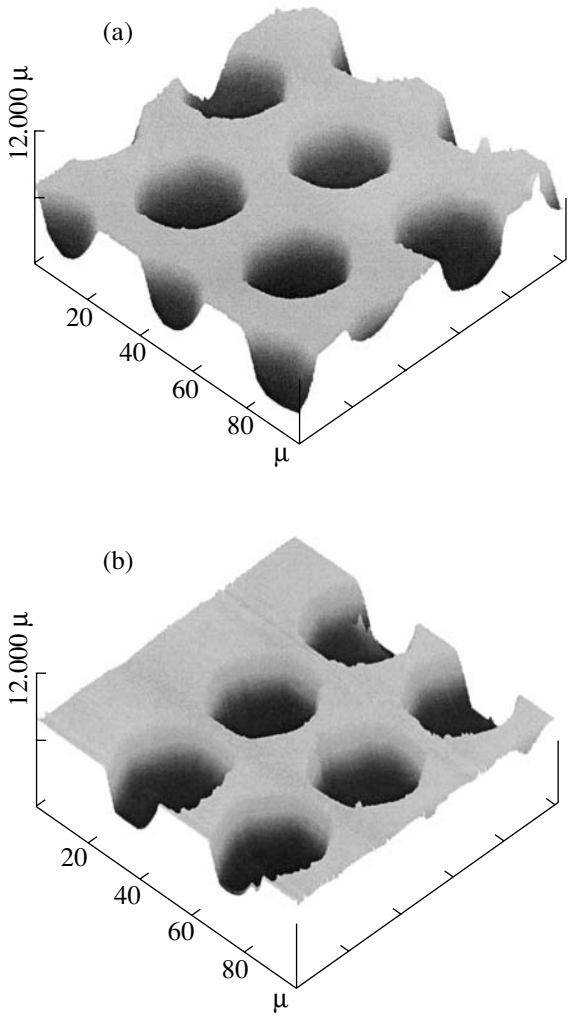

Fig. 1. Magnetic photonic crystals based on the YIG films with (a) a square lattice and (b) a hexagonal lattice. The period of the structure is 50 μm, and the radius of the holes is 20 μm. The image is obtained by an atomic force microscope.

structure consisting of magnetic and nonmagnetic layers. The realization of such a structure is rather difficult, because the periodicity of the magnetic properties of layers can be violated in the course of the layer growth, which will break the magnon crystal structure possessing a magnon bandgap. From the point of view of application, a two-dimensional magnon crystal formed on the basis of ferromagnetic films seems to be preferable. This crystal represents a ferromagnetic waveguide with two-dimensional magnetization inhomogeneities. The inhomogeneities can be represented by, e.g., implanted elements of another ferromagnet or holes made in the structure. As the initial object for fabricating a magnon crystal, we choose a ferromagnetic yttrium iron garnet (YIG) film grown epitaxially on a nonmagnetic gadolinium gallium garnet substrate. Magnetostatic spin waves can be easily excited in such films by microstrip transducers. Owing to the high

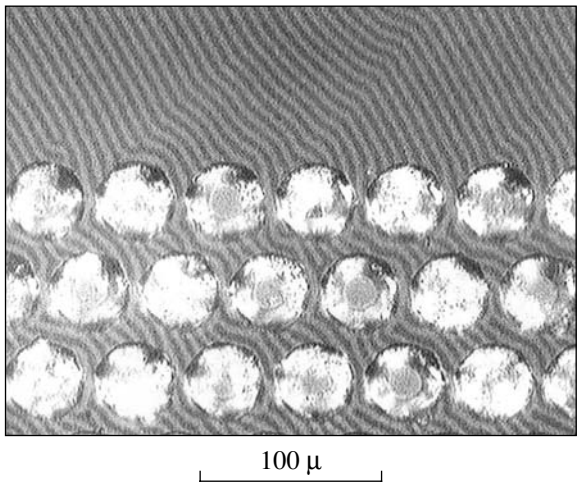

Fig. 2. Image of the magnon crystal surface from a polarizing microscope. In addition to the holes, one can see the domain structure.

quality of the films, the propagation loss in them should be fairly small, and the magnetostatic spin waves propagate in these films without any considerable attenuation within distances of many wavelengths. The structure studied by us was a YIG film with holes made by etching. The diameter of the holes and their periodicity were taken to be close to a half-wavelength (to satisfy the Bragg reflection condition). The transverse dimensions of the film were 1.5×0.5 cm^2, and the film thickness was 5 μm. The periodic hole structures were made in the films by the photolithographic technique according to the following procedure. A silicon dioxide layer was deposited on the YIG film. Then, the structure was covered by a 1.3-μm-thick photoresist layer, which was insolated through a chromium mask with a periodic hole pattern. Two types of hole patterns were used: a square lattice and a hexagonal lattice. After exposure, silicon dioxide was eliminated by a mixture of hydrofluoric acid and ammonium fluoride (solution 1). Then, the remaining silicon dioxide lattice was used as a mask for etching the YIG film in an aqueous solution of phosphoric acid and iron chloride (with a molar proportion of 49.4 : 49.4 : 1.2; solution 2). The time and temperature of etching were chosen so as to etch the material through a thickness of 4–4.5 μm. After the etching procedure, silicon dioxide was completely eliminated by solution 1. The hole thickness and the surface structure were studied by a three-dimensional optical rugosi meter and an atomic force microscope (D300 Digital Instruments and Solver P47H NT-MDT). Figure 1 presents the micrographs of square and hexagonal etch patterns in the YIG films. The micrographs were obtained using the atomic force microscope. The hole thickness is 4 μm, and the hole period is about 50 μm. In addition, the film surface was also analyzed by a polarizing microscope. Figure 2 shows the micrograph of the ferromagnetic film surface in a weak bias mag-

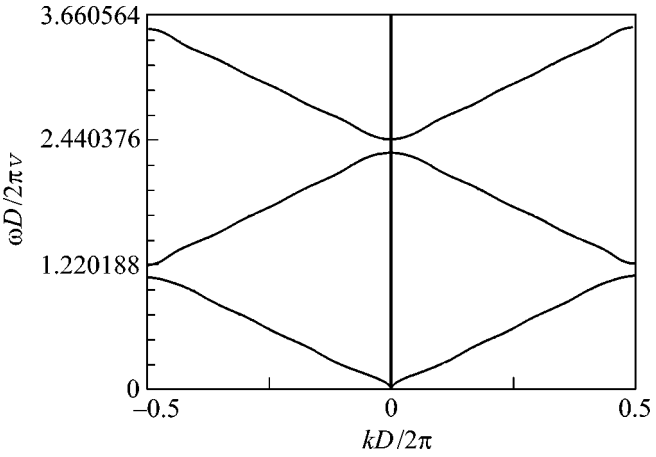

Fig. 3. Spectrum of magnetostatic spin waves propagating in the periodic structure with the period $D = 10$ μm; v is the group velocity of spin waves.

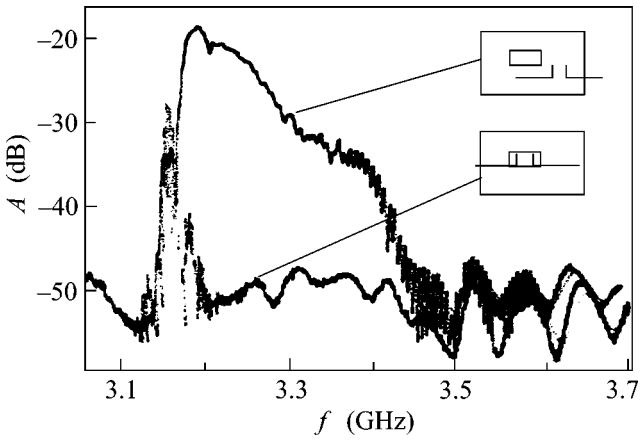

Fig. 4. Amplitude–frequency characteristic of the model delay line for the case of the propagation of magnetostatic surface spin waves in a film with a hexagonal structure. The bias magnetic field is 530 Oe.

netic field. Apart from the holes, a magnetic domain structure is clearly visible on the film surface.

The spectrum of spin waves propagating in a ferromagnetic film with a two-dimensional periodic structure is determined from the solutions to the Landau–Lifshits equations for the magnetization motion and the Maxwell equations with the corresponding boundary (at the film surface) and periodic conditions [11, 12]. As a result of solving the boundary-value problem, we obtain the generalized dispersion equation

$$\cos\kappa_1 d\cos\kappa_2 d + \left(\frac{\kappa_1}{2\kappa_2} + \frac{\kappa_2}{2\kappa_1}\right)\sin\kappa_1 d\sin\kappa_2 d = \cosh(2q_z D), \quad (1)$$

where d is the film thickness, D is the period of the periodic structure, q_z is the wave number of the propagating spin wave, and κ_1 and κ_2 are the propagation constants of spin waves. The latter are determined by the relations

$$\kappa_1 = \sqrt{q_z^2 - k_0^2\mu_\perp}, \quad \kappa_2 = \sqrt{q_z^2 - k_0^2\varepsilon},$$

$$\mu_\perp = \frac{(\mu^2 - \nu^2)}{\mu}, \quad \mu = 1 + \frac{\omega_H\omega_M}{\omega_H^2 - \omega^2},$$

$$\nu = \frac{\omega_H\omega_M}{\omega_H^2 - \omega^2}, \quad \omega_H = \gamma H, \quad \omega_M = 4\pi\gamma M_0,$$

where H is the external magnetic field, M_0 is the saturation magnetization of the ferromagnet, and ω is the spin wave frequency. The spectrum of the waves propagating in the periodic structure is shown in Fig. 3. One can see that the spectrum contains bandgaps corresponding to frequencies at which the wave propagation through the periodic structure is impossible. It should be noted that the position of the bandgap in the frequency spectrum depends on the parameters of the film (the periodic structure) and on the external magnetic field. Thus, by varying the magnetic field, one can control the spectrum of the waves propagating in a magnetic photonic crystal.

To experimentally test the spectra of spin waves propagating in magnon crystals, we constructed delay lines, each line containing a ferromagnetic film with the etched structure and transducers converting electromagnetic signals to spin waves (the input and output transducers). We studied the amplitude–frequency characteristics of the propagating spin waves. The characteristics were obtained using a phase compensator (PC2-18), which measured the phase difference and attenuation. The model delay line was placed in the gap of an electromagnet, so that the bias magnetic field could be varied by changing the distance between the magnet poles. The spacing between the antennas was 5 mm, and the length and width of the antennas were 3 mm and 40 μm, respectively. We compared the amplitude–frequency characteristics of the YIG film part that was not etched and the part that was adjacent to the etched film area (in Fig. 4, the etched area is the small rectangle) with the amplitude–frequency characteristics of the film part containing the periodic etch pattern. From Fig. 4, one can see that the frequency band of spin wave excitation (the zone of magnon existence) is much narrower for the case of wave excitation in the film containing the periodic structure of etched holes. Figure 5 presents the amplitude–frequency characteristics of the propagating spin waves for the cases when the exciting antennas partially covered the area of the etched hole structure. The frequency band of spin wave excitation decreases by an order of magnitude: when the wave excitation occurs in the smooth (nonetched) region, the frequency band is 400 MHz, and when the waves are excited and propagate in the region with the holes, the frequency band of wave excitation is about 50 MHz.

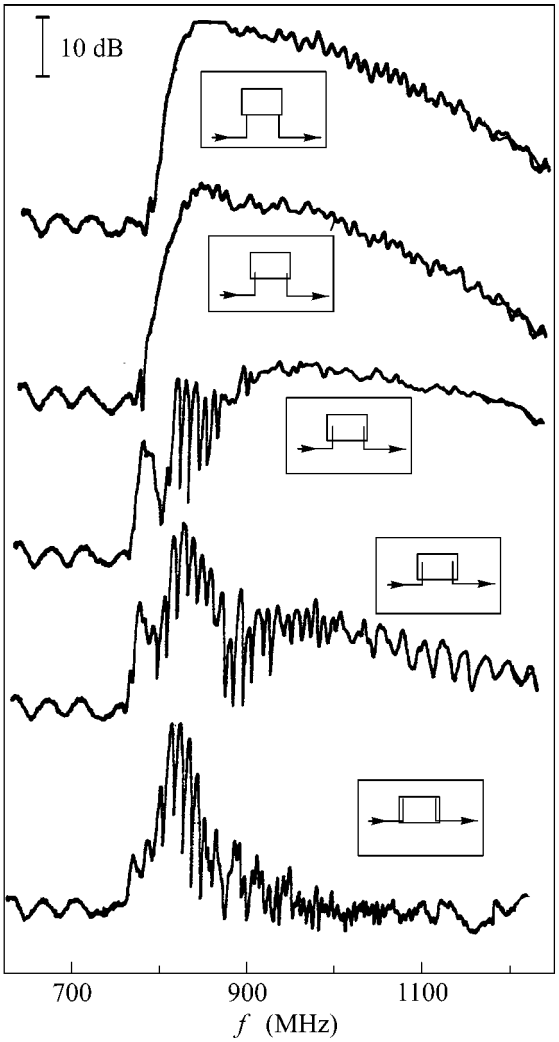

Fig. 5. Amplitude–frequency characteristic of the model delay line for the case of the propagation of magnetostatic surface spin waves in a film with a hexagonal structure in a bias magnetic field of 55 Oe for different positions of the input and output antennas with respect to the region containing the holes.

Thus, in this paper, we proposed the fabrication of ferromagnetic film–based photonic crystals that have a photonic bandgap in the frequency spectrum of spin waves propagating in them (the magnon crystals). We fabricated specimens of such crystals on the basis of YIG films. Using atomic force and polarization microscopes, we studied the structure of these crystals. We studied the propagation of magnetostatic spin waves in the ferromagnetic films representing the magnon crystals. We presented the amplitude–frequency characteristics of spin waves and calculated the band structure of magnetic photonic crystals.

This work was supported by the Russian Foundation for Basic Research, project nos. 02-02-17166 and 01-02-17178, and the International Science and Technology Center (ISTC), project no. 1522.

REFERENCES

1. J. D. Joannopoulos, R. D. Meade, and J. N. Winn, *Photonic Crystals: Molding the Flow of Light* (Princeton Univ. Press, Princeton, N.J., 1995).
2. *Photonic Bandgap Materials*, Ed. by C. M. Soukoulis (Kluwer Academic, Dordrecht, 1996).
3. K. Sakoda, *Optical Properties of Photonic Crystals* (Springer, Berlin, 2001).
4. S. G. Johnson and J. D. Joannopoulos, *Photonic Crystals: The Road from Theory to Practice* (Kluwer, Boston, 2002).
5. J. O. Vasseur, L. Dobrzynski, B. Dijafari-Rouhani, and H. Puszkarski, Phys. Rev. B **54**, 1043 (1996).
6. H. Al-Wahsh, A. Akjouj, B. Dijafari-Rouhani, *et al.*, Phys. Rev. B **59**, 8709 (1999).
7. A. Figotin and I. Vitebsky, Phys. Rev. E **63**, 066609 (2001).
8. S. A. Nikitov, Ph. Tailhades, and C. S. Tsai, J. Magn. Magn. Mater. **236**, 320 (2001).
9. Yu. V. Gulyaev and S. A. Nikitov, Dokl. Akad. Nauk **380**, 469 (2001) [Dokl. Phys. **46**, 687 (2001)].
10. M. Inoue, K. I. Arai, M. Afujii, *et al.*, J. Magn. Soc. Jpn. **23**, 1861 (1999).
11. S. A. Nikitov and Ph. Tailhades, Opt. Commun. **190**, 389 (2001).
12. I. L. Lyubchanskii, N. N. Dadoenkova, M. I. Lyubchanskii, *et al.*, Appl. Phys. B **74**, 711 (2002).

Translated by E. Golyamina

JETP Letters, Vol. 77, No. 10, 2003, pp. 571–576. Translated from Pis'ma v Zhurnal Éksperimental'noĭ i Teoreticheskoĭ Fiziki, Vol. 77, No. 10, 2003, pp. 675–680.
Original Russian Text Copyright © 2003 by Meĭlikhov.

Magnetic Phase Diagram for a Random Three-Dimensional Ising Point-Dipole Lattice

E. Z. Meĭlikhov

Institute of Molecular Physics, Russian Research Centre Kurchatov Institute, pl. Akademika Kurchatova 1, Moscow, 123182 Russia

e-mail: meilikhov@imp.kiae.ru

Received February 21, 2003; in final form, April 14, 2003

It is shown, within the framework of the generalized mean-field theory, that the ground state of a system of Ising point dipoles randomly filling the sites of a three-dimensional cubic lattice depends on the fraction p of filled sites. For example, a body-centered lattice is ferromagnetic at $p > p_{c1} \approx 0.55$, a spin glass at $p_{c1} < p < p_{c2} \approx 0.35$, and paramagnetic at $p < p_{c2}$. The transition between these states has a percolation nature. The temperature dependences of the magnetization in the ferromagnetic phase and the susceptibility in the paramagnetic phase were determined. The magnetic phase diagram of the system was constructed. © *2003 MAIK "Nauka/Interperiodica".*

PACS numbers: 75.10.Nr; 75.50.Lk; 75.30.Kz

1. INTRODUCTION

The traditional mean-field theory of magnets, while taking into account thermal fluctuations of interacting magnetic moments, does assume that their local fields are identical. This assumption is not true for random systems with configurational disorder. The latter leads to spatial fluctuations of a local field, which, in contrast to thermal fluctuations, precludes the establishing of magnetic order even at zero temperature. In the systems with long-range interactions, to which our random three-dimensional Ising point-dipole lattice belongs, this is supplemented by the necessity of including the anisotropy of this interaction.

Thus, to adequately describe disordered magnetic systems, the traditional mean-field theory must be generalized. The character of generalization depends on the type of random process. In "liquid" random systems, the point dipoles can be situated at any site of the space, and, to a first approximation, the correlation in their spatial arrangement need not be taken into account. The corresponding random process is markovian, and, to determine the distribution function for random magnetic fields in such a system, one can use the Markov theory [1]. The magnetic properties of such systems are considered in [2]. In random lattice structures, dipoles can (randomly) occupy only the sites of a certain regular (crystal) array. The method [1] does not apply to such systems, because they are not markovian. It is the purpose of this work to consider the magnetic properties of a non-markovian three-dimensional random lattice.

The properties of Ising ferromagnets with short-range (exchange) interaction between magnetic moments have been studied by the statistical [3] and percolation [4] methods. Unfortunately, these methods are unsuitable for the systems with long-range (in particular, dipolar) interactions. In this case, it is necessary to appropriately modify the mean-field theory for random systems.

The model of a random dipole lattice considered in this work can be used to describe the properties of various physical objects. Among these are materials with giant magnetoresistance (magnetic nanograins in a nonmagnetic metallic matrix), transparent ferromagnets (including those in a polymeric matrix), frozen ferromagnetic fluids, and crystalline systems with partially substituted magnetic ions. Among the latter, the $LiHoF_4$ compound crystallizing in the sheelite structure $CaWO_4$ (space group C_{4h}^6) is noteworthy. Its ferromagnetism (Curie temperature $T_C = 1.53$ K) is due to the Ho^{3+} ions with magnetic moments $m \sim 13\mu_B$. A partial substitution of the nonmagnetic ions Y^{3+} (with a closed $4p^6$ electronic configuration) for Ho ions gives rise to the $LiHo_xY_{1-x}F_4$ compound, in which the magnetic ions Ho^{3+} are randomly distributed over the corresponding lattice sites. The exchange interaction between the magnetic moments of these ions (their $4f$ shell is unfilled ($4f^{10}$ configuration)) is efficiently screened by $5s$ and $5p$ electrons. In such a situation, the dipole–dipole interactions between ions become dominant and, due to crystal anisotropy, their magnetic moments assume an Ising character. The Curie temperature $T_C(x)$ of this compound decreases monotonically with increasing x (especially in the range $x = 0.4$–0.3), and it becomes paramagnetic at $x \sim 0.2$ [5].

In this work, a model of a random Ising-dipole lattice is suggested which can be used for the adequate description of the magnetic properties of $LiHo_xY_{1-x}F_4$.

2. GENERALIZED MEAN-FIELD THEORY FOR A RANDOM 3D POINT-DIPOLE LATTICE

Let us consider a three-dimensional square lattice, whose sites are randomly occupied by Ising magnetic dipoles. The fraction of filled sites is p and the dipole magnetic moments $\mathbf{m}_{ikl}$ are parallel to one of the lattice faces and take only two values: $\mathbf{m}_{ikl} = \pm m\mathbf{e}_0$, where $\mathbf{e}_0$ is a unit vector in the dipole direction.

In the traditional theory, each dipole is subjected to the same local field $\mathbf{H}_0$, which determines the mean magnetic dipole moment $\langle \mathbf{m}_{ikl} \rangle_T$ (angular brackets stand for ensemble averaging, and the subscript T denotes thermodynamic averaging). For Ising dipoles, $\mathbf{H}_0 \parallel \mathbf{e}_0$, and one has

$$\langle \mathbf{m}_{ikl} \rangle_T = \frac{\sum_{\mathbf{m} = \pm m\mathbf{e}_0} \mathbf{m} \exp(\mathbf{m}\mathbf{H}_0/kT)}{\sum_{\mathbf{m} \pm m\mathbf{e}_0} \exp(\mathbf{m}\mathbf{H}_0/kT)} = m\mathbf{e}_0 \tanh(mH_0/kT), \quad \mathbf{I} = n\langle \mathbf{m}_{ikl} \rangle_T, \tag{1}$$

where $\mathbf{I}$ is the magnetization of the system and n is the dipole concentration. For a sample shaped like a prolate cylinder with its axis parallel to the direction of magnetic dipoles, the local field $\mathbf{H}_0$ is also parallel to its axis and equals

$$H_0 = \frac{4\pi}{3} I + H_3. \tag{2}$$

Here, $(4\pi/3)I$ is the Lorentz field produced by the polarization magnetic charges at the surface of a sufficiently large sphere,

$$H_3 = m \sum_{ikl} \frac{3\cos^2 \alpha_{ikl} - 1}{\rho_{ikl}^3}, \tag{3}$$

where the summation goes over the sites occupied by the dipoles inside the sphere, ρ_{ik} is the distance between a certain dipole (placed at the origin of coordinates) and the dipole at the site (ikl), and α_{ikl} is the angle between the line connecting these dipoles and the direction $\mathbf{e}_0$.

Let the system with randomly distributed dipoles be in the state with mean magnetization $\mathbf{I} \parallel \mathbf{e}_0$. The local magnetic fields H_3 are different for different lattice sites and characterized by the distribution function $F_p(\eta; H_3)$, which that depends on the fraction p of occupied lattice sites and the fraction η of dipoles whose average moments are directed along the magnetization $\mathbf{I}$ of the system.

Let us consider the possibility of magnetic ordering in the random system of interest. The magnetization is $\mathbf{I} = pn\langle \mathbf{m}_i \rangle_T$, where the average magnetic moment $\langle \mathbf{m}_i \rangle_T$ should be calculated with allowance made for the scatter of random fields H_3 through the generalization of regular Eq. (1). The corresponding mean random-field equation for the magnetization $j = I/pnm$ has the form

$$j = \int_{-\infty}^{\infty} \tanh\left[\frac{1}{\Theta}\left(\frac{4\pi}{3} pj + \frac{H_3}{mn}\right)\right] F_p(j; H_3) dH_3, \tag{4}$$

where $\Theta = kT/m^2 n$ is the reduced temperature (the magnetization $j = 2\eta - 1$ is one of the arguments of the function F_p).

The ground state ($T = 0$) of the system is ferromagnetic ($j_0 \equiv j(T = 0) = 1$) if the integral on the right-hand side of Eq. (4) equals unity at $j = 1$. With allowance for the normalization of the distribution function, this condition means that the random fields H_0 must be positive at all lattice sites. It is fulfilled if $F_p(1; 4\pi I/3 + H_3 < 0) = 0$.

The limiting case of a lattice whose sites are completely filled with dipoles ($p = 1$) was considered in [6], where it was shown that the character of the ground state of a long sample with a cubic dipole lattice depends on the lattice type; a simple lattice is always antiferromagnetic, whereas body-centered and face-centered lattices are ferromagnetic. In the two latter cases, the magnetic field H_3 is zero at all lattice sites if $p = 1$. According to the abovesaid, this corresponds to the distribution function $F_p(1; H_3) = \delta(0)$, which, clearly, satisfies the above- mentioned condition for ferromagnetism.

To answer the question of whether the ferromagnetic state can be the ground state of a partially filled random lattice ($p < 1$), one must know how the distribution function $F_p(j; H_3)$ changes its form with a decrease in p. Inasmuch as no exact methods for determining the form of this function are presently available, we calculated it numerically for a body-centered cubic lattice of Ising point dipoles, whose magnetic moments were directed along one of the lattice faces. The dipoles were distributed uniformly and randomly (with probability p) over the sites of a $21 \times 21 \times 21$ lattice, and the magnetic field H_3 was calculated for the central site. The functions $F_p(1; H_3)$ were found by exhausting a large number (about 10^4) of realizations for this system. The resulting distribution functions $F_p(1; H_3)$ are shown in Fig. 1.

At $p \approx 1$, the distribution function has a quasi-delta-like form and is centered near zero. As the fraction p of filled sites decreases, the width of the distribution first increases and then decreases. This follows from the fact that the distribution functions $F_p(1; H_3)$ and $F_{1-p}(1; H_3)$ for the complementary systems with, respectively, the fractions p and $(1 - p)$ of filled sites are related to each other as $F_p(1; H_3) = F_{1-p}(1; -H_3)$.

One can see from Fig. 1 that, when p is close to unity, the distribution function corresponds to the ferro-

magnetic ground state. However, at relatively small p values, this function becomes nonzero in a broader range of H_3 fields, which, according to the abovesaid, precludes the formation of a ferromagnetic state with $j_0 = 1$. Therefore, with a decrease in p, the system undergoes a percolation magnetic phase transition from the ferromagnetic state to the magnetic (spin) glass state with $j_0 < 1$.

To determine the percolation threshold p_{c1} for this transition, we introduce the parameter $\Omega(p)$ characterizing the degree of penetration of the distribution function $F_p(1; H_0)$ into the region with $H_3 < 4\pi I/3$. It is equal to the probability of a dipole configuration with such an H_3 value occurring among various configurations with a given p value. In other words, $\Omega(p)$ is the fraction of configurations with $H_3 < 4\pi I/3$ among all studied (for a given p) dipole configurations. The corresponding (numerically found) dependence is presented in Fig. 2.

As in the standard percolation theory [4], the $\Omega(p)$ dependence follows the power law (it is linear in our case): $\Omega(p) \propto (p_{c1} - p)$ with the percolation threshold $p_{c1} = 0.55 \pm 0.02$. This value considerably (more than twofold) exceeds the value $p_c = 0.25$ corresponding to the percolation magnetic phase transition from the ferromagnetic to paramagnetic state in a body-centered cubic magnetic-moment lattice with short-range (pair) interactions [4]. This is so because the net result of the long-range dipole–dipole interactions is more sensitive to the disorder in the system.

Analogous calculations suggest that the face-centered cubic Ising-dipole lattice is even more sensitive to disorder; in the ground state, it remains a genuine ferromagnet (i.e., characterized by the magnetization $j_0 = 1$) only in a very narrow interval $p_{c1} < p < 1$, where $p_{c1} \approx 0.95$ (recall, in this connection, that the ground state of a simple cubic Ising-dipole lattice is not ferromagnetic at $p = 1$).

3. MAGNETIC PHASE DIAGRAM

It was established above that, at $p > p_{c1}$, the ground state ($T = 0$) of our system corresponds to a magnetic glass with magnetization $j_0 < 1$. The temperature dependence of magnetization and the Curie temperature of the system for a chosen p value is determined by Eq. (4). To find its solution, one should trace how the corresponding distribution function $F_p(j; H_0)$ changes upon varying j. An example of such evolution is shown in Fig. 3 for the distribution function $F_{0.9}(j, H_3)$. In the numerical calculations, the sign of the dipole magnetic moment was chosen at random on the condition that the fraction of dipoles with upward directed moments is $\eta = (1 + j)/2$. It is seen that the distribution width increases monotonically with decreasing magnetization (cf. Fig. 1 relating to the systems with $j = 1$ but various p), leading to a decrease in the Curie temperature.

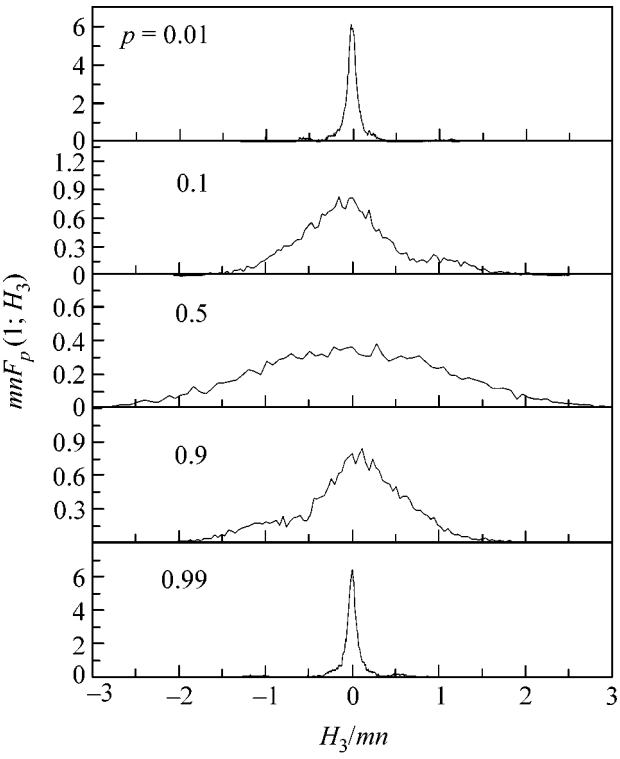

Fig. 1. Local-magnetic-field distribution functions $F_p(1; H_0)$ over the sites of a body-centered cubic Ising-dipole lattice for dipoles of the same sign ($j = 1$) and various fractions p of randomly occupied sites.

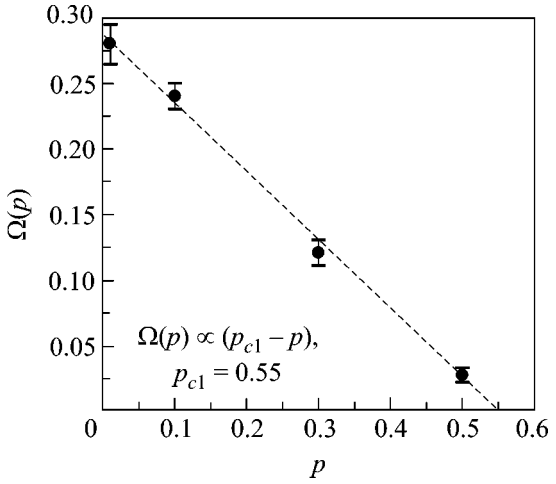

Fig. 2. Extrapolation method for determining the percolation threshold. Points are for the results of numerical calculations, and the dashed line represents the linear dependence $\Omega(p) \propto (p_{c1} - p)$ ($p_{c1} = 0.55$).

Using the calculated distribution functions F_p, one can evaluate the integral on the right-hand side of Eq. (4) and find its solution for different values of magnetization j and temperature. The temperature depen-

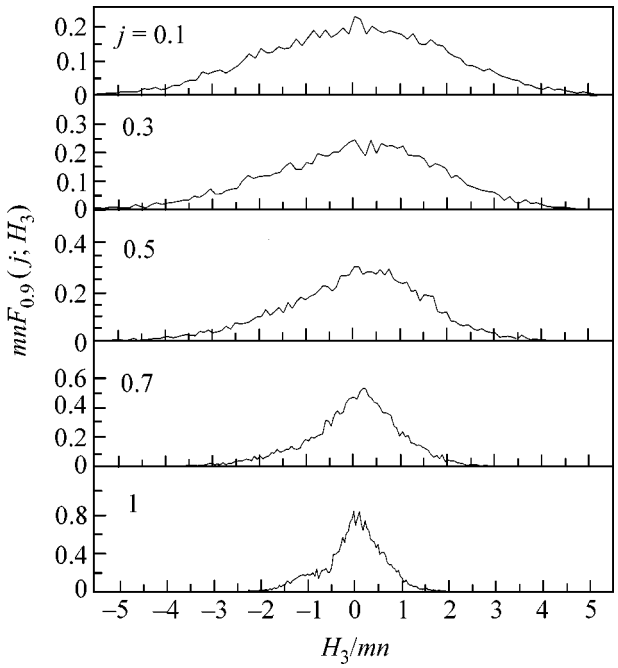

Fig. 3. Local-magnetic-field distribution functions $F_{0.9}(j, H_0)$ over the sites of a random ($p = 0.9$) body-centered cubic Ising-dipole lattice for dipoles of different sign.

dences of magnetization determined for two p values, one of which ($p = 0.9 > p_{c1}$) corresponds to the ferromagnetic phase and the other ($p = 0.5 < p_{c1}$), to the glass phase, are shown in Fig. 4.

The width of the temperature range ($0 < \Theta < \Theta_C$) where the random system of interest possesses spontaneous magnetization $j > 0$ decreases with decreasing p, and the system becomes paramagnetic in its ground state at dipole concentrations smaller than a certain critical value ($p < p_{c2}$; see below).

To describe the properties of the paramagnetic system in an external magnetic field H_e, one can again use the mean-field Eq. (4) with the replacement $H_3 \longrightarrow H_e + H_3$ in the argument of tanh, following which this equation takes the form

$$j = \int_{-\infty}^{\infty} \tanh\left[\frac{1}{\Theta}\left(\frac{4\pi}{3}pj + \frac{H_e + H_3}{mn}\right)\right] F_p(j; H_3)\,dH_3. \quad (5)$$

As before, of greatest interest is the low-field magnetic susceptibility $\chi = \lim_{H_e \to 0}(\partial I/\partial H_e)$, for which one obtains from Eq. (5)

$$\chi = \frac{pJ_1(p, \Theta)}{\Theta - [(4\pi p/3)J_1(p, \Theta) + \Theta J_2(p, \Theta)]}, \quad (6)$$

where

$$J_1(p, \Theta) = \int_{-\infty}^{\infty} \frac{F_p(0; H_3)\,dH_3}{\cosh^2(H_3/\Theta mn)},$$
$$J_2(p, \Theta) = \int_{-\infty}^{\infty} \tanh(H_3/\Theta mn)\left(\frac{\partial F_p(j; H_3)}{\partial j}\right)_{j=0} dH_3. \quad (7)$$

Analysis of the calculated distribution functions $F_p(j; H_3)$ showed that $J_2 \ll J_1$; this greatly simplifies Eq. (6) for the susceptibility and the Curie temperature of the system. The Curie temperature is found from the condition that the denominator in Eq. (6) turn to zero; i.e., it is the root of the equation

$$\Theta = (4\pi p/3)J_1(p, \Theta). \quad (8)$$

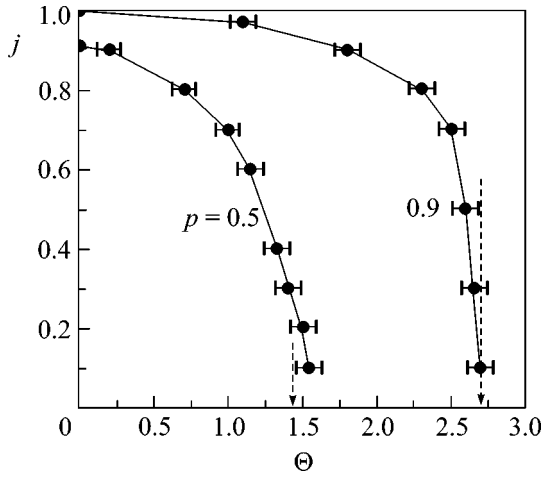

Fig. 4. Temperature dependences of the magnetization of random ($p = 0.9, 0.5$) body-centered cubic Ising-dipole lattices. The dashed lines indicate the corresponding Curie temperatures calculated by Eq. (8).

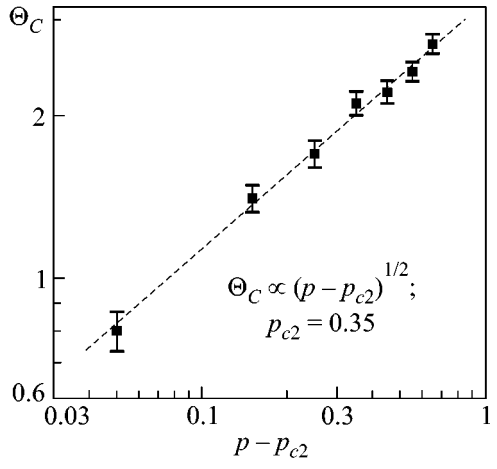

Fig. 5. Concentration dependence of the Curie temperature of a random body-centered cubic Ising-dipole lattice.

The concentration dependence of the reduced Curie temperature $\Theta_C(p)$ calculated by Eq. (8) is shown in Fig. 5. It fits well the power law $\Theta_C \propto (p - p_{c2})^{1/2}$, where $p_{c2} = 0.35$. The value $\Theta_C \approx 3$ found for the maximal Curie temperature for $p = 1$ corresponds to the characteristic dipole-dipole interaction energy $kT_C \sim m^2 n$ (for $LiHoF_4$, $m \approx 13\mu_B$ and $n \approx 1.4 \times 10^{22}$ cm^{-3} [5], which gives $T_C \sim 1$ K, in agreement with the experiment).

These results can be used to construct the magnetic phase diagram for the random system considered (Fig. 6). In this diagram, the regions of ferromagnetic, glass, and paramagnetic states are plotted in the coordinates "dipole concentration–temperature."

To what degree this diagram is correct in describing the magnetic behavior of the systems of interest, one need only compare it with the experimental data on the properties of the $LiHo_xY_{1-x}F_4$ compound. The experimental magnetic phase diagram for $LiHo_xY_{1-x}F_4$ (inset in Fig. 6) closely resembles the diagram obtained in this work. One can thus believe that the magnetic properties of $LiHo_xY_{1-x}F_4$ can be adequately described by the model of a random Ising-dipole lattice considered in this work.

The temperature dependence of the susceptibility in the paramagnetic phase is given by Eq. (6). The corresponding $\chi(T)$ curves shown in Fig. 7 indicate that the temperature behavior of the susceptibility at $\Theta \gg \Theta_C$ obeys the Curie law. However, the susceptibility of a system with nonzero ground-state magnetization does not fit the standard linear law $\chi^{-1} \propto (T - T_C)$; as $T \longrightarrow T_C$, it increases more slowly because of the "destructive" effect of configurational disorder.

CONCLUSIONS

For random systems with magnetic interactions, the mean-field theory requires generalization and the taking into account the nonequivalence of individual magnetic moments, because their surroundings are different (random). As the fraction p of the sites occupied by dipoles decreases in a configurationally disordered three-dimensional Ising point-dipole lattice, the system undergoes a percolation transition from the ferromagnetic state to the glass state and then to the paramagnetic state. In contrast to the percolation phase transition in a system with short-range exchange interactions, our system provides an example of long-range percolation. The percolation thresholds for these two cases are substantially different.

All of the results of this work were obtained within the framework of a modified mean-field theory, which, like the traditional approximation, disregards spin correlations. In a system with long-range interactions, to which the three-dimensional dipole–dipole interaction belongs, only long-range correlations are possible. The latter can be taken into account using the Ginzburg–Landau (GL) theory. As known [7], the GL theory brings about results that differ from the mean-field results only in the temperature range near the critical temperature and which change only slightly the mean-field T_C value and, hence, the magnetic phase diagram obtained in this work. One of the possible manifestations of spin correlations is that, in certain local configurations, the moments of some dipoles are in opposition to the magnetization of the system (i.e., $j_0 < 1$ even at $p_{c1} < p < 1$). The magnetization of the system differs

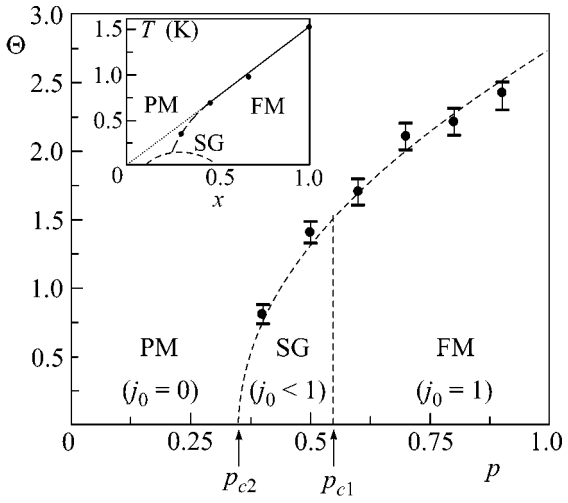

Fig. 6. Magnetic phase diagram of a random body-centered Ising-dipole lattice (FM = ferromagnet, SG = spin glass, PM = paramagnet). Inset: experimental magnetic phase diagram of the $LiHo_xY_{1-x}F_4$ compound.

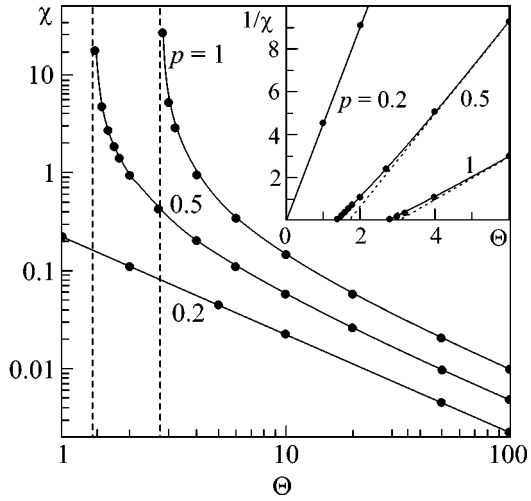

Fig. 7. Temperature dependences of low-field magnetic susceptibility in the paramagnetic state of random ($p = 0.99$, 0.5, 0.2) body-centered Ising-dipole lattices. The vertical dashed lines indicate the corresponding Curie temperatures calculated by Eq. (8). Inset: the same for the reciprocal of magnetic susceptibility; the inclined dashed straight lines are the extrapolations of the linear high-temperature curves $\chi^{-1} \propto (\Theta - \Theta_C)$.

from unity if the distribution function $F_p(1; H_0)$ is nonzero in the region of large negative magnetic fields. Numerical calculations could have provided the answer to the question of how much this function is different from zero and how fast it decreases in this region. However, any numerical calculation based on exhausting a finite number of random realizations cannot give an answer to the question about the degree of penetration of the distribution function $F_p(1; H_0)$ into the region of large negative fields. It is seen only that this degree is exceedingly small, because the functions $F_p(1; H_0)$ resemble Gaussian functions (Figs. 2, 4), for which the system magnetization is close to unity with exponential accuracy.

This work was supported by the Russian Foundation for Basic Research, project no. 03-02-17029.

REFERENCES

1. S. Chandrasekhar, Rev. Mod. Phys. **15**, 1 (1943).
2. E. Z. Meĭlikhov and R. M. Farzetdinova, Zh. Éksp. Teor. Fiz. (2003) (in press).
3. T. L. Hill, *Statistical Mechanics: Principles and Selected Applications* (McGraw-Hill, New York, 1956; Inostrannaya Literatura, Moscow, 1960).
4. B. I. Shklovskiĭ and A. L. Éfros, *Electronic Properties of Doped Semiconductors* (Nauka, Moscow, 1979; Springer, New York, 1984).
5. D. H. Reich, B. Ellman, J. Yang, *et al.*, Phys. Rev. B **42**, 4631 (1990).
6. J. A. Sauer, Phys. Rev. **57**, 142 (1940).
7. V. S. Dotsenko, Usp. Fiz. Nauk **165**, 481 (1995) [Phys. Usp. **38**, 457 (1995)].

Translated by V. Sakun

JETP Letters, Vol. 77, No. 10, 2003, pp. 577–581. From Pis'ma v Zhurnal Éksperimental'noĭ i Teoreticheskoĭ Fiziki, Vol. 77, No. 10, 2003, pp. 681–685.
Original English Text Copyright © 2003 by Dorozhkin.

Giant Magnetoresistance Oscillations Caused by Cyclotron Resonance Harmonics¶

S. I. Dorozhkin

Institute of Solid State Physics, Russian Academy of Sciences, Chernogolovka, Moscow region, 142432 Russia
e-mail: dorozh@issp.ac.ru

Received April 17, 2003

For high-mobility two-dimensional electrons at a GaAs/AlGaAs heterojunction, we have studied, both experimentally and theoretically, the recently discovered giant magnetoresistance oscillations with nearly zero resistance in the oscillation minima which appear under microwave radiation. We have proposed a model based on nonequilibrium occupation of Landau levels caused by radiation which describes the oscillation picture. © *2003 MAIK "Nauka/Interperiodica".*

PACS numbers: 73.40.-c; 73.43.Qt; 75.47.De

Recent observations in high-quality two-dimensional electron systems of microwave-stimulated giant magnetoresistance oscillations (MSGMO) [1, 2] with positions corresponding to subharmonics of the cyclotron resonance [3] and especially the discovery of zero-resistance states in the MSGMO minima [4, 5] attract great attention to this spectacular phenomenon [6–14]. Observation of zero-resistance states was a reason to assume [4, 5] their collective origin, such as photon-stimulated superconductivity [4]. An alternative approach to the explanation of zero-resistance states is based on the peculiarities of electron motion in crossed electric and magnetic fields, when electron drift along an electric field can occur only as a result of scattering events. In recent preprint [7], it has been demonstrated that MSGMO with negative magnetoresistance in minima can result from transitions between broadened Landau levels caused by photon absorption and accompanied by elastic scattering on short-range scatterers. A similar effect was shown rather long ago [15] to give a sequence of photocurrent peaks of different signs for unbroadened Landau levels and nonlinear conditions with respect to an electric field. For bulk semiconductors and quantizing magnetic fields, photocurrent oscillations with negative conductivity in minima were predicted in [16] for δ-type photoelectron energy distribution function. A link between states with negative dissipative conductivity and the zero-resistance states was proposed in [8] (see also [11]). It implies that negative dissipative resistivity gives rise to instability in a system which finally breaks its symmetry and produces inhomogeneous states with nearly zero average resistance. This result allows one to associate theoretical states with negative dissipative resistivity and the experimental zero-resistance states. The inhomogeneous states are characterized by high local current density even at zero net current through a sample. One more approach to the explanation of MSGMO based on edge magnetoplasma instability was considered in preprint [13].

In this paper, we reproduce previous experimental observations [1, 2, 4, 5] of MSGMO with some additional data and compare them with our calculations, based on the results of the self-consistent Born approximation (SCBA), which are capable of explaining the main features of MSGMO in terms of nonequilibrium occupation of broadened Landau levels under microwave radiation. Additionally, our model predicts the appearance of the second harmonic in Shubnikov–de Haas oscillations for an appropriate choice of microwave frequency and sample parameters.

We have measured a Hall bar sample with an *L*-shaped conducting channel. Channel width was equal to 0.2 mm, and the distances between neighboring potential probes were either 0.4 or 0.6 mm. Magnetoresistance per square R_{xx} and Hall resistance R_{xy} have been measured by the standard technique exploiting the low-frequency AC current excitation and phase-sensitive detection of a voltage between potential probes with the use of a lock-in amplifier. We used the frequency 9.2 Hz and amplitude of the current 1 μA, well within the ohmic regime. The results for R_{xx} and R_{xy} presented in this paper do not depend on pairs of potential probes used for measurements. The sample was produced from a GaAs/AlGaAs wafer of the standard structure containing a two-dimensional electron system at a single remotely doped GaAs/AlGaAs heterojunction with the spacer width about 55 nm. The most pronounced MSGMO were observed after illumination of the sample until saturation of electron density at about $n_s = 3 \times 10^{11}$ cm^{-2}. The corresponding mobility of elec-

¶ This article was submitted by the author in English.

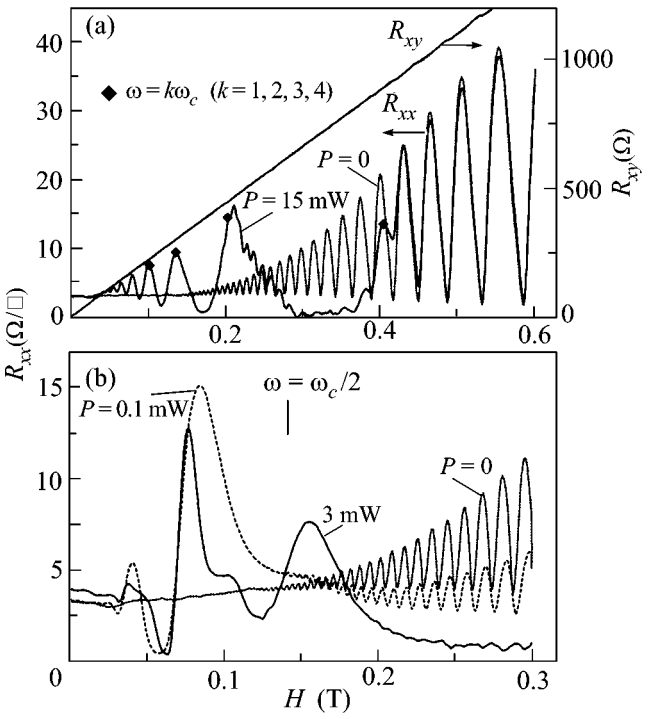

Fig. 1. Magnetoresistance R_{xx} Hall resistance R_{xy} measured with excitation current $I = 1$ μA versus magnetic field H in the absence of microwave radiation (dotted lines) and under microwave radiation (dashed and solid lines). Data in (a) and (b) were measured at frequencies 168 and 30 GHz, respectively, at temperature $T = 0.4$ K. Power P shown in Figs. corresponds to the oscillator output. Positions of magnetic fields corresponding to subharmonics of the cyclotron resonance are marked in (a) by diamonds. $n_s = 2.84 \times 10^{11}$ cm^{-2}.

trons was $\mu = 7 \times 10^6$ cm^2/(V s). The sample was placed in a close ended rectangular waveguide of the WR-62 type with cross-section 16×8 mm, which was placed in a ^{3}He refrigerator. The two arms of the L-shaped sample were parallel to the long and the short sides of the rectangular. The microwave radiation in the frequency range 10–170 GHz was produced by a set of oscillators. The microwave power reaching the low-temperature end of the waveguide was estimated to be always below 2 mW. At frequencies greater than 50 GHz, the transmission coefficient between oscillator output and the low-temperature part of the waveguide was rather low, falling down to values on the order of 0.01.

Typical experimental data are shown in Fig. 1. In the absence of microwave radiation, magnetoresistance R_{xx} demonstrates at $H \geq 0.15$ T standard Shubnikov–de Haas oscillations periodic in the inverse magnetic field with the period determined by the areal density of electrons n_s in a two-dimensional system. Corresponding oscillations in R_{xy} become visible only at magnetic fields higher than 0.4 T. Microwave radiation suppresses Shubnikov–de Haas oscillations at low magnetic fields and gives rise to new oscillations (microwave stimulated giant magnetoresistance oscillations) also periodic in the inverse magnetic field with the period determined by microwave frequency (compare Fig. 1a and 1b). Positions of MSGMO follow those of subharmonics of the cyclotron resonance $\omega = k\omega_c^{(k)} \equiv k(eH^{(k)}/m^*c)$. Here, $m^* = 0.067m_e$ is the effective mass of electrons in GaAs. The main minima and maxima of MSGMO are shifted to different sides from the corresponding subharmonic. Additional weaker oscillation arises at comparatively low-frequency and high-power radiation at $\omega < \omega_c$ and can be associated with the cyclotron resonance harmonic $\omega < \omega_c/2$ (see Fig. 1b). In the main MSGMO minima, the magnetoresistance can become rather close to zero (see also [4, 5]). MSGMO peaks have a characteristic asymmetric triangular form with a steep drop at the low-magnetic-field side. At the same time, the microwave radiation has practically no effect on the Hall resistance (in Fig. 1a the solid R_{xy} curve measured in the presence of the microwaves is practically indistinguishable from the "dark" dotted curve).

Our calculations of magnetoconductivity tensor components σ_{xx} and σ_{xy} are based on formulas obtained within the self-consistent Born approximation in the absence of Landau level mixing (see [17] and references therein):

$$D(\epsilon) = \sum_{n=0}^{\infty} \frac{2N_0}{\pi\Gamma_n}\left[1 - \left(\frac{\epsilon - \epsilon_n}{\Gamma_n}\right)^2\right]^{1/2} \equiv \sum_{n=0}^{\infty} \frac{2N_0}{\pi\Gamma_n} Z_n^{1/2}(\epsilon), \quad (1)$$

$$\sigma_{xx} = \frac{e^2}{\pi^2\hbar}\sum_{n=0}^{\infty}\left(\frac{\Gamma_n^{xx}}{\Gamma_n}\right)^2 \int_{\epsilon_n - \Gamma_n}^{\epsilon_n + \Gamma_n} \left(-\frac{df}{d\epsilon}\right) Z_n(\epsilon)\, d\epsilon, \quad (2)$$

$$\sigma_{xy} = -\frac{n_s ec}{H} + \frac{e^2}{\pi^2\hbar}\sum_{n=0}^{\infty}\frac{(\Gamma_n^{xy})^4}{\Gamma_n^3\hbar\omega_c}\int_{\epsilon_n - \Gamma_n}^{\epsilon_n + \Gamma_n}\left(-\frac{df}{d\epsilon}\right) Z_n^{3/2}(\epsilon)\, d\epsilon. \quad (3)$$

Here, $D(\epsilon)$ is the density of states and $\epsilon_n = \hbar\omega_c(n + 1/2)$ is the energy of the nth spin-degenerate Landau level with the width Γ_n and the total number of states on the level $N_0 = 2eH/hc$. Contributions of this level to σ_{xx} and σ_{xy} are characterized by the parameters Γ_n^{xx} and Γ_n^{xy}, respectively. Our modification of the equations of [17] is the use of nonequilibrium distribution function $f(\epsilon)$, which is formed, at zero temperature, as a result of direct one-photon transitions (induced and spontaneous), i.e., transitions accompanied by the energy change by $\hbar\omega$ and the nearly zero momentum variation equal to the photon momentum. We neglect all other excitation and relaxation processes. Such a function

can arise if the lifetime of a photoexcited electron is the shortest time in the problem. This condition is normally justified if the energy of this electron is less than the energy of optical phonon (see, for example, [18]), which is fulfilled in our experiment. As can be shown, the distribution function obtained under these conditions is appropriate for calculations of the magnetoconductivity in accordance with Eqs. (2) and (3).

At zero temperature, it is easy to write down the condition of the steady state which relates values of the distribution function $f(\epsilon)$ at energies differing by $\hbar\omega$:

$$f(\epsilon) = \frac{\lambda f(\epsilon - \hbar\omega)}{\lambda + 1 - f(\epsilon - \hbar\omega)}. \quad (4)$$

Here, the parameter λ characterizes microwave intensity. This relation is applicable at nonzero densities of states $D(\epsilon)$ and $D(\epsilon - \hbar\omega)$. If $D(\epsilon) = 0$ or $D(\epsilon - \hbar\omega) = 0$, we set $f(\epsilon) = f_0(\epsilon)$, where f_0 is the Fermi distribution function at $T = 0$. Eq. (4) and condition $\int_{-\infty}^{+\infty} f(\epsilon)D(\epsilon)d\epsilon = n_s$ define the nonequilibrium distribution function that was used for calculations of the conductivity. Figure 2 demonstrates that, in some ranges of energy, photon-stimulated interlevel transitions can give rise to an inverted population of electron states ($df/d\epsilon > 0$) leading to negative contributions to the conductivity σ_{xx}. The inversion is possible only when $\omega > \omega_c$. The inverted occupation shown in the right panel of Fig. 2 is obviously independent of the position of the Fermi energy on the lower level, i.e., of the filling factor of Landau levels. Our computation shows (see Fig. 3) that the appearance of energy regions with inverted population of broadened Landau levels can lead to the negative sign of σ_{xx} and, consequently, to the negative magnetoresistance $R_{xx} = \sigma_{xx}/(\sigma_{xx}^2 + \sigma_{xy}^2)$. We have considered two limiting cases of the short- and long-range scatterers when analytical formulas are available for dependences of the parameters Γ_n, Γ_n^{xx}, and Γ_n^{xy} on n and magnetic field [17]. For the short-range (long-range) scatterers there is only one (two) independent parameter (s). Figure 3 shows the results of our calculations. To get data corresponding to the absence of radiation, we have set the parameter λ to the very low value $\lambda = 1 \times 10^{-10}$. The results obtained under radiation provide MSGMO with both the form of the oscillations and their positions, in reasonable agreement with the experiment (namely, the minimum (maximum) associated with a particular subharmonic lies at $\omega > k\omega_c^{(k)}$ ($\omega < k\omega_c^{(k)}$). The main difference from the experiment is the fact that the calculated magnetoresistance in the MSGMO minima is negative. Elimination of this discrepancy lies beyond our model, which is applicable for macroscopically homogeneous systems, and could be referred to the results of [8]. Additionally, there are at least two more mechanisms leading to suppression of the negative conductivity, which are finite temperature

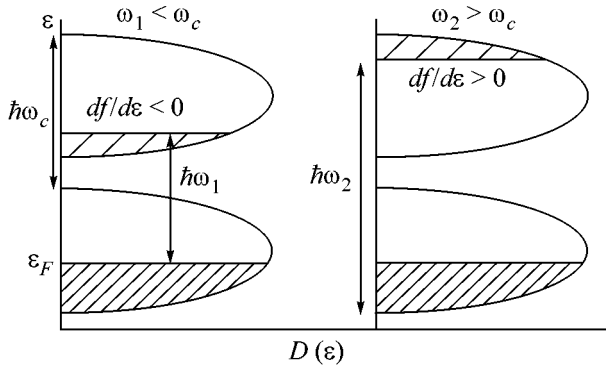

Fig. 2. Schematic of the electron redistributions between two neighboring broadened Landau levels, which are caused by microwave radiation of two frequencies $\omega_1 < \omega_c$ (left panel) and $\omega_2 > \omega_c$ (right panel). Partly occupied states are shaded. The lowest level contains the Fermi energy ϵ_F at zero temperature. Assumptions concerning relaxation processes are discussed in the text.

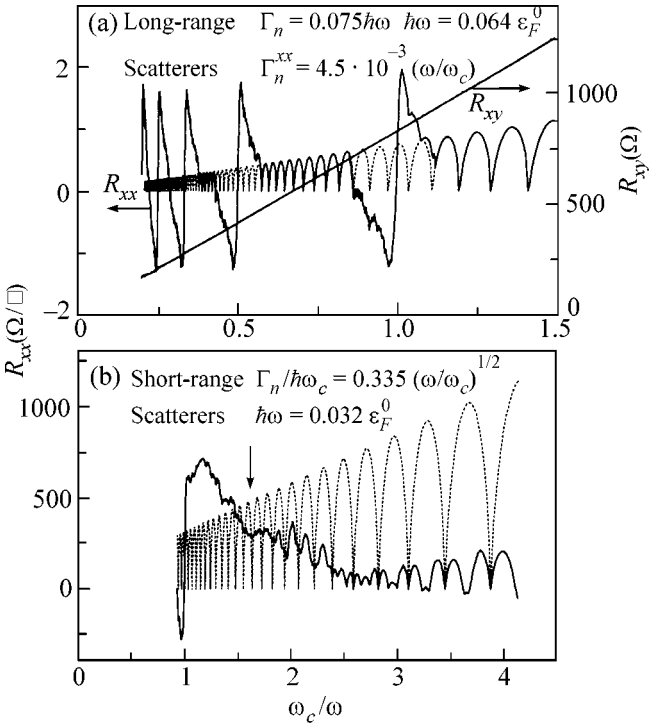

Fig. 3. Calculated magnetoresistance R_{xx} and Hall resistance R_{xy} versus ratio ω_c/ω proportional to magnetic field for two very different intensities of microwave radiation, characterizing by parameter $\lambda = 1 \times 10^{-10}$ (dotted line) and $\lambda = 2$ (solid line). The solid and dotted R_{xy} lines overlap, (a) and (b)—correspond to two limiting cases of the scatterer range, different values of the microwave frequency, and different values of Landau level width (corresponding parameters are shown in the figure).

and all kinds of relaxation processes. These arguments show that the calculated regions of negative magnetoresistance can be associated with the experimental minima of MSGMO. For $\omega = k\omega_c^{(k)}$, our model predicts the absence of the photoresponse in magnetoresistance. But this is valid only for the two limiting cases of short-range and long-range scatterers, when the width of a Landau level Γ_n is independent of a level number n [17]. For the intermediate-range scatterers, points where $R_{xx}|_{P=0} = R_{xx}|_{P\neq 0}$ should depend on the radiation power P and be shifted from the positions of the subharmonics, which is consistent with our experimental data, where these points always appear at lower magnetic fields than the corresponding subharmonics. Additional shift of these points can result from relaxation processes.

It is necessary to discuss the role of different unknown parameters that enter our model. Absolute values of Γ_n, Γ_n^{xx}, Γ_n^{xy}, and λ affect only amplitude and the detailed form of the Shubnikov–de Haas oscillations and MSGMO. Neither of these parameters influences the positions of the oscillations. Explanation of the experimentally established absence of the photoresponse in the Hall resistance is closely related to the absolute values of parameters Γ_n, Γ_n^{xx}, and Γ_n^{xy}. Within SCBA this result appears rather natural for the case of long-range scatterers (in Fig. 3a the solid and dotted R_{xy} lines overlap) and needs very narrow Landau levels in the other limiting case. A problem arises with the absolute values of the magnetoresistance even in the absence of microwaves (see also the results of [7] obtained within SCBA for short-range scatterers). In comparison with experiment, SCBA gives either too high or too low values of magnetoresistance for two limiting cases of short-range and long-range scatterers, respectively. But it seems to be possible to get reasonable absolute values of the magnetoresistance together with the absence of the photoresponse in the Hall resistance for intermediate-range scatterers. Comparison of the lower limit for the range of potential fluctuations, given by the spacer width, with the cyclotron radius in magnetic fields involved shows that, in our experimental conditions, intermediate-range scatterers are of great importance.

An important aspect of the experimental results is the existence of MSGMO in very weak magnetic fields, where Shubnikov–de Haas oscillations are not observed. Obviously, the appearance of MSGMO proves the existence of the Landau quantization in corresponding magnetic fields. We explain the absence of the Shubnikov–de Haas oscillations in these fields by inhomogeneous broadening of the oscillations picture caused by long-range carrier density fluctuations in a sample. MSGMOs are much less affected by this broadening because of the larger period of these oscillations measured in the filling factors of Landau levels. Inhomogeneous broadening is not included in our model, and Shubnikov–de Haas oscillations and MSGMO coexist at the same magnetic fields.

It is interesting to note that, in addition to MSGMO, the results of our calculations describe some additional features of the experimental data. In the case of comparatively narrow Landau levels, the Shubnikov–de Haas oscillations are only slightly modified by microwave radiation at $\omega \lesssim \omega_c$ and in between the $k = 1$ minimum and $k = 2$ maximum of MSGMO (compare Figs. 1a and 3a). At rather wide Landau levels, experimentally realized at weaker magnetic fields, our model describes strong suppression of the magnetoresistance at $\omega \ll \omega_c$ in very good agreement with our observations (compare Figs. 1b and 3b) and leads to the appearance of additional minima related to the $\omega = \omega_c/2$ harmonic (shown by arrow in Fig. 3b). Note that the latter effect appears in our model without two-photon processes. Our model predicts that, for the appropriate choice of Landau level width and microwave frequency and power, a great second harmonic can appear in the Shubnikov–de Haas oscillation picture (in Fig. 3b it occurs at $\omega_c/\omega > 2.5$).

In summary, we have shown that the experimentally measured photoresponse of two-dimensional electrons on microwave radiation, including MSGMO, is consistent with our theory considering conventional magnetotransport effects under conditions of nonequilibrium occupation of electronic states.

The author thanks Professor K. von Klitzing and Dr. J.H. Smet for the kind opportunity to carry out the experimental part of this research in the Max Planck Insitut für Festkörperforschung (Stuttgart, Germany) and Dr. V. Umansky for providing the author with GaAs/AlGaAs material. The author gratefully acknowledges valuable discussion with S.V. Iordansky and the partial support of this work by INTAS and the Russian Foundation for Basic Research.

REFERENCES

1. M. A. Zudov, R. R. Du, J. A. Simmons, and J. L. Reno, Phys. Rev. B **64**, 201311(R) (2001).
2. P. D. Ye, L. W. Engel, D. C. Tsui, *et al.*, Appl. Phys. Lett. **79**, 2193 (2001).
3. In this paper, we use the definition of the cyclotron resonance subharmonics as $\omega = k\omega_c^{(k)}$, in accordance with that in [17]. Here, k is an integer, $\omega/2\pi$ is the microwave frequency, and $\omega_c = eH/m^*c$ is the cyclotron frequency in magnetic field H for carriers with effective mass m^*.
4. R. G. Mani, J. H. Smet, K. von Klitzing, *et al.*, Nature **420**, 646 (2002).
5. M. A. Zudov, R. R. Du, L. N. Pfeiffer, and K. W. West, Phys. Rev. Lett. **90**, 046807 (2003).
6. J. C. Phillips, cond-mat/0212416; V. Shikin, Pis'ma Zh. Éksp. Teor. Fiz. **77**, 281 (2003) [JETP Lett. **77**, 236 (2003)].

7. A. C. Durst, S. Sachdev, N. Read, and S. M. Girvin, cond-mat/0301569.
8. A. V. Andreev, I. L. Aleiner, and A. J. Millis, cond-mat/0302063.
9. P. W. Anderson and W. F. Brinkman, cond-mat/0302129.
10. J. Shi and X. C. Xie, cond-mat/0302393.
11. A. F. Volkov, cond-mat/0302615.
12. A. A. Koulakov and M. E. Raikh, cond-mat/0302465.
13. S. A. Mikhailov, cond-mat/0303130.
14. C. L. Yang, M. A. Zudov, T. A. Knuuttila, *et al.*, cond-mat/0303472.
15. V. I. Ryzhiĭ, Fiz. Tverd. Tela (Leningrad) **11**, 2577 (1969) [Sov. Phys. Solid State **11**, 2078 (1970)].
16. V. Elesin, Pis'ma Zh. Éksp. Teor. Fiz. **7**, 229 (1968) [JETP Lett. **7**, 176 (1968)]; Zh. Éksp. Teor. Fiz. **55**, 792 (1968) [Sov. Phys. JETP **28**, 410 (1968)].
17. T. Ando, A. B. Fowler, and F. Stern, Rev. Mod. Phys. **54**, 437 (1982).
18. M. A. Habbeger and H. Y. Fan, Phys. Rev. Lett. **12**, 99 (1964).

JETP Letters, Vol. 77, No. 10, 2003, pp. 582–586. Translated from Pis'ma v Zhurnal Éksperimental'noĭ i Teoreticheskoĭ Fiziki, Vol. 77, No. 10, 2003, pp. 686–690.
Original Russian Text Copyright © 2003 by Baranov, Goloshchapov, Medvedkin, Voevodin.

Detection of Magnetic Resonance Signals with Anomalous Dispersion and Two Types of Isolated Manganese Centers in the Chalcopyrite Crystal (Zn,Mn)GeP_2

P. G. Baranov*, S. I. Goloshchapov*, G. A. Medvedkin*, and V. G. Voevodin**

** Ioffe Physicotechnical Institute, Russian Academy of Sciences, St. Petersburg, 194021 Russia*
e-mail: stanislav.goloshchapov@mail.ioffe.ru
*** Siberian Physicotechnical Institute, Tomsk, 634050 Russia*

Received April 21, 2003

Anomalously intense dispersion was observed in the magnetic resonance signals of manganese clusters in the chalcopyrite crystal $ZnGeP_2$:Mn with a high concentration of manganese. The EPR signals detected corresponded to two types of isolated manganese ions. One of these apparently possesses acceptor properties, which makes manganese a self-contained impurity for the formation of a ferromagnetic state in accordance with recent theoretical predictions. © *2003 MAIK "Nauka/Interperiodica".*

PACS numbers: 76.30.Da; 75.30.-m; 75.50.Pp

Electron charge and spin are the basis of modern information technology; however, charge and spin properties are used in different materials: semiconductors (Si, GaAs) and ferromagnets, respectively. It is natural to suggest that the use of electron charge and spin properties in the same material holds the greatest promise. In this case, inasmuch as the electronic properties (conductivity) are controlled by doping donor or acceptor impurities, the magnetic properties can be changed by introducing magnetic impurities; in other words, the solution of the problem resides in the creation of a new class of materials, namely, magnetic semiconductors. Originally, it seemed that compounds of the II–VI type were the most suitable semiconductors. These compounds can readily be doped with magnetic ions, for example, manganese, in high concentrations, because manganese readily replaces a cation, for example, zinc. However, it is difficult to control *n* and *p* types of conductivity in such materials. At the same time, compounds of the III–V type are difficult to dope with Mn ions in sufficient concentrations because of the low solubility of these elements. The development of methods for doping such compounds with the use of molecular-beam epitaxy (MBE) is one of the ways for solving this problem [1]; however, the use of ternary compounds of the chalcopyrite type (for example, $ZnGeP_2$) is also promising. On the one hand, these compounds are analogues of III–V compounds, on the other hand, manganese can replace zinc in a natural way. In this case, high concentrations of manganese can be obtained under equilibrium conditions, in contrast to oversaturated solutions of III–V (Mn) compounds obtained by MBE. It should be noted that, at one time the use of ternary compounds (for example, yttrium–aluminum garnets) instead of binary ones (sapphire) solved the problem of introducing high concentrations of rare-earth element impurities into crystals for creating lasers based on them.

Electron paramagnetic resonance (EPR) is one of the most direct methods for studying magnetic impurity ions. A number of papers have been published in which manganese was studied by the EPR method in III–V crystals [2–4] and in a number of chalcopyrites [5, 6]. In all the materials, except for GaAs, the EPR spectra of only Mn^{2+} ions were observed. Signals of the Mn^{2+}–hole complex were detected in the GaAs crystal along with Mn^{2+} spectra. The hole occupied a delocalized orbital centered at the Mn^{2+} ion [2, 3]; that is, Mn^{2+} is a negatively charged acceptor $A^-(3d^5)$.

In recent years, a number of works have appeared in which the observation of magnetic ordering (ferromagnetism) at room temperature is reported for chalcopyrite films doped with manganese in high concentrations [7–9], in particular, in (Zn,Mn)GeP_2 films grown on single crystal $ZnGeP_2$ substrates [8, 9]. Recently, ferromagnetism at room temperature has been observed in bulk (Zn,Mn)GeP_2 materials [10]. Studies of magnetic resonance in the (Zn,Mn)GeP_2/$ZnGeP_2$ system are presented in [11]. EPR signals of isolated Mn^{2+} ions replacing zinc were detected in the $ZnGeP_2$ substrate. In this case, in the process of manufacturing the magnetic film, manganese diffused into the substrate containing, according to the EPR data [11], a high concentration of zinc vacancies. It was also suggested that more than one type of manganese centers are contained in the substrate. The occurrence of two types of manganese in (Zn,Mn)GeP_2 is a principal problem, because,

0021-3640/03/7710-0582$24.00 © 2003 MAIK "Nauka/Interperiodica"

according to the new theory [12], manganese can replace germanium and create holes, which just leads to ferromagnetism in these compounds. Thus, searching for EPR signals of manganese replacing germanium is an urgent problem. The goal of this work is to perform studies of bulk $ZnGeP_2$:Mn crystals containing high concentrations of magnesium (~2%) using magnetic resonance techniques.

The experiments were carried out on a commercial EPR spectrometer (Jeol) at a frequency of 9.3 GHz (X-range) with the use of a laboratory-made flow helium cryostat, which allowed the temperature to be varied in the range of 4–300 K. All EPR spectra presented in the figures were recorded without accumulation as a result of one sweep.

Several types of magnetic resonance signals were detected in $ZnGeP_2$:Mn (~2%) crystals. Part of the signals represented EPR absorption spectra of isolated manganese ions. These signals were characterized by the conventional hyperfine (HF) structure in the form of a sextet of lines due to the HF interaction of unpaired electrons with the nuclear magnetic moment of manganese $I = 5/2$; the signals were observed without significant changes throughout the entire range of temperatures at which the studies were performed (4–300 K). A signal in the form of a broad (~30 mT) unresolved line was also observed. This signal significantly differed from the conventional EPR signal, because it was characterized by anomalously intense dispersion.

Figure 1 presents EPR spectra of the $(Zn,Mn)GeP_2/ZnGeP_2$ structure (curves *1a* and *1b*) and the $ZnGeP_2$:Mn crystal containing ~2% Mn (curve *2*). EPR spectra *1a* and *1b* were measured at a temperature of 4.2 K in the $ZnGeP_2$ substrate of the structure (because of the small thickness of the $(Zn,Mn)GeP_2$ film, EPR spectra cannot be observed in it) in orientations close to $\mathbf{B} \parallel c$ (five groups of fine-structure lines corresponding to transitions $M_S = 1/2 \longleftrightarrow M_S = -1/2$, $M_S = \pm 3/2 \longleftrightarrow M_S = \pm 1/2$, and $M_S = \pm 5/2 \longleftrightarrow M_S = \pm 3/2$ are shown only for the $\mathbf{B} \parallel c$ orientation; see [11]) and $\mathbf{B} \perp c$, respectively. Spectrum *2* was measured in the $ZnGeP_2$:Mn crystal (~2%) at a temperature of 30 K. EPR signals *1a* and *1b* belong to isolated Mn^{2+} ions replacing zinc ions (Mn^{2+}_{Zn}), and the broad unresolved line in the form of absorption belongs to saturated EPR signals of zinc vacancies (a low temperature of 4.2 K was used precisely for the saturation of this line overlapping with the Mn^{2+} signals, and the EPR signal of zinc vacancies was used for the detection of the crystal orientation).

Six virtually equidistant narrow lines are observed in the spectrum in Fig. 1, curve *2*. These lines are of approximately the same intensity, and an additional five pairs of lines are seen between them. This EPR signal (we designate it as Mn(I)) is typical of the central transition $M_S = 1/2 \longleftrightarrow M_S = -1/2$ for Mn^{2+} ions ($S = 5/2$),

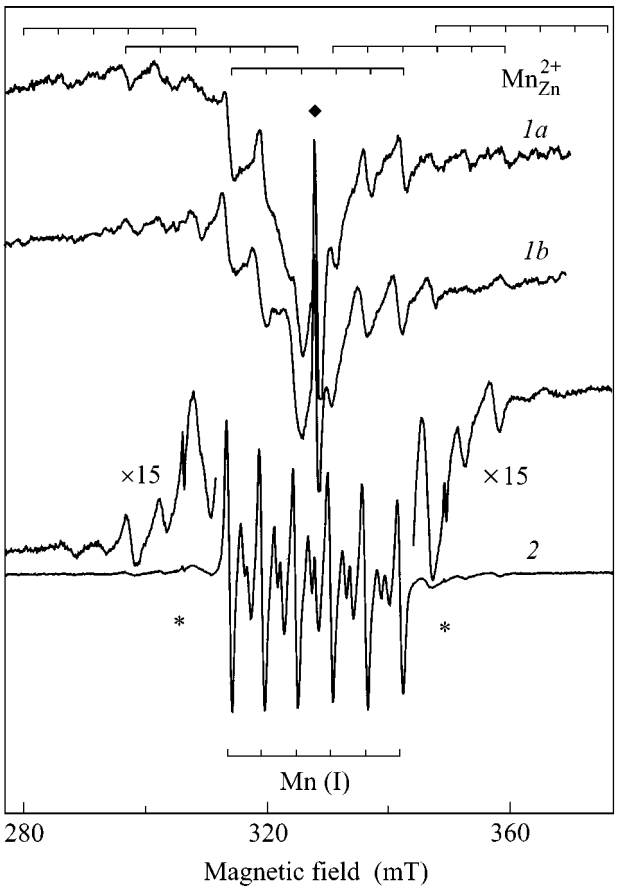

Fig. 1. EPR spectra of (*1a*, *1b*) the $(Zn,Mn)GeP_2/ZnGeP_2$ structure and (*2*) the $ZnGeP_2$:Mn crystal containing ~2% Mn. EPR spectra *1a* and *1b* were measured in the $ZnGeP_2$ substrate of the structure at a temperature of 4.2 K for orientations close to $\mathbf{B} \parallel c$ (five fine-structure-line groups are shown only for the $\mathbf{B} \parallel c$ orientation); spectrum *2* was measured in the $ZnGeP_2$:Mn crystal (~2%) at a temperature of 30 K for the orientation of the magnetic field corresponding to the maximum splitting of the fine structure assigned to the Mn(II) spectrum. The low-field and high-field parts of signal *2* are shown separately with 15× magnification. The sextet of lines of the HF structure with forbidden transitions between them is assigned to Mn(I) centers. The narrow line in curves *1a* and *1b* with $g = 2.00237$ designated by a rhombus belongs to quartz, and narrow lines designated by stars in spectrum *2* belong to boundary lines in the EPR spectrum of Mn^{2+} ions in MgO, which we used as a reference.

where the lines arranged between the six main transitions correspond to forbidden transitions $\Delta M_S = 1$, $\Delta m_I = \pm 1$. Additional lines of lower intensity are seen in spectrum *2* (also shown with 15× magnification). These lines are arranged symmetrically about the central line and represent the fine structure of isolated manganese centers (spectrum *2* was recorded for the orientation with the largest splitting of this fine structure). Apparently, the fine-structure lines do not belong to Mn(I) centers because of the large difference in intensities; therefore, we designate them as Mn(II). The narrow

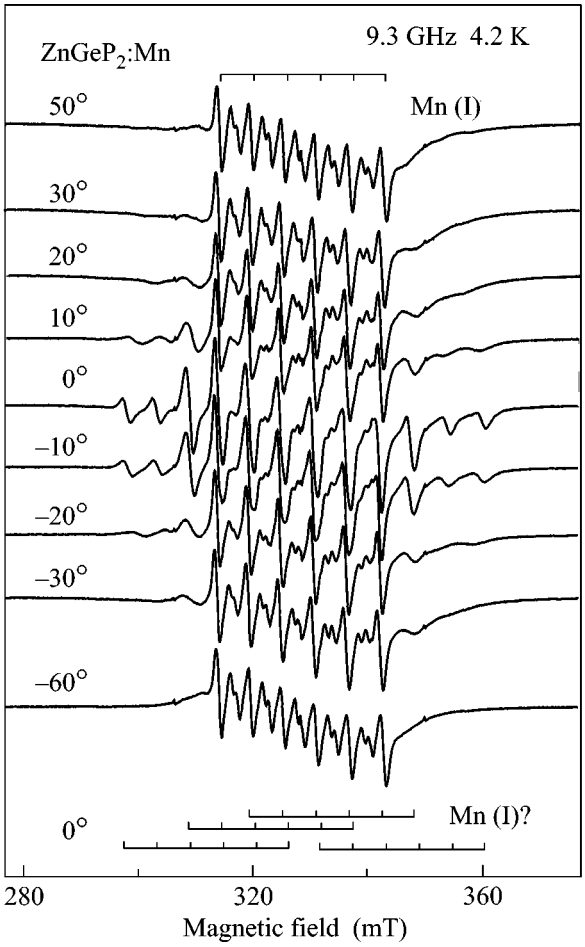

Fig. 2. Orientation dependences of the EPR signals observed in the $ZnGeP_2$:Mn crystal (~2%) recorded at 4.2 K. The orientation at which the fine structure splitting is a maximum and the line width is a minimum corresponds to 0°. The sextet of lines above is designated as Mn(I), and its position insignificantly varies with orientation. At the bottom, the four groups of six lines correspond to the position of the fine structure lines for an angle of 0°. Their correspondence to the Mn(I) center or a center with $S = 2$ is discussed in the text.

line with $g = 2.00237$ designated by a rhombus belongs to quartz, and narrow lines designated by stars belong to boundary lines in the EPR spectrum of Mn^{2+} ions in MgO. These lines were used as reference signals.

Orientation dependences of the EPR signals in the $ZnGeP_2$:Mn crystal (~2%) recorded at 4.2 K are shown in Fig. 2. A fine structure is seen in the spectrum (shown below for an angle of 0° as four sextets). Its distinctive feature is a strong broadening and, as a consequence, a sharp decrease in the intensity of these lines upon deviation from the orientation with maximum splitting. This behavior can be observed in the presence of a certain defect in the nearest environment of manganese (for example, a hole center), which causes symmetry lowering and reduces strain in the vicinity of the Mn ion (deviation from the axial symmetry). In this case, a defect can be located at several positions with respect to the manganese ion. The fine structure is characterized in the standard designations [13] by the spin Hamiltonian parameters D (axial symmetry) and E (deviation from the axial symmetry). The sharp broadening of the lines upon variation of the angle proves that an angle of 0° approximately corresponds to the magnetic-field direction along the symmetry axis of the manganese center. Only for this orientation does parameter E make no contribution to the position of the EPR line. This contribution increases with increasing angle and reaches a maximum at an angle of 90°. The greatest effect is observed for the outer groups of the fine structure; therefore, the signal is hardly seen at angles exceeding ~40° and the outer lines are broadened more rapidly. Exchange interactions between manganese ions can also make a certain contribution to the broadening of fine-structure lines. In addition, relatively intense EPR signals were detected as a group of six lines of the manganese HF structure in the region of fields of 150–160 mT ($g \sim 4$), which, probably, correspond to the transitions forbidden for Mn(I) centers with the selection rules $\Delta M_S = 2$, $\Delta m_I = 0, \pm 1$. Significant orientation dependences of the intensity were observed for these forbidden EPR signals. It was also found that EPR signals for some orientations exhibited splitting into a larger number of lines. The EPR spectra presented in Fig. 2 essentially differ from the conventional signals of Mn_{Zn}^{2+}; therefore, we believe that these spectra belong to isolated manganese ions located at a different crystal lattice position. Two suggestions can be made concerning the observed fine structure in Fig. 2. The first suggestion is that this line is associated with the central sextet of lines (Mn(I), shown above in Fig. 2) and belongs to a center with $S = 5/2$, that is, to an Mn^{2+} ion, because the appearance of this fine structure correlates with the disappearance of the lines of the forbidden transitions and because all the lines are comparable in intensity. The hyperfine structure constant of Mn(I) manganese centers is comparable with the corresponding constant for Mn_{Zn}^{2+} (~5.6 mT), which may point to a high degree of covalence [14]. Thus, the interstitial position of manganese can be excluded from consideration, and it is very likely that manganese occupies a germanium position in the lattice. According to the second suggestion, the fine-structure lines observed in Fig. 2 can be considered separately from the central sextet of lines if it is assumed that the fine structure for Mn(I) is completely averaged, for example, due to strong exchange interactions. Then, the fine structure in Fig. 2 in the form of four mutually overlapping groups of lines by six lines in each group may belong to Mn^{3+} centers with a spin $S = 2$, which also confirms the germanium position of manganese.

The charge and spin state of Mn(II) centers cannot be unambiguously determined because of the strong overlap of their EPR signals with more intense lines of

Mn(I) centers. It is important to emphasize that the fine structures presented in Fig. 1 (curve *2*) and Fig. 2 are observed for different orientations of the magnetic field; that is, the symmetry axes of these centers do not coincide. Along with the natural suggestion that these signals belong to Mn^{2+} centers, the occurrence of the state with an integer spin S cannot be excluded, which excludes the charge state Mn^{2+} and corresponds to the state Mn^{3+} or Mn^{+}. However, additional investigations with precisely oriented crystals are necessary. The main challenge of this work was to show that several different EPR spectra of isolated manganese ions are observed in the crystal. The occurrence of twins in the crystal cannot be excluded, which complicates the interpretation of the EPR spectra; however, we investigated crystals of different sizes (differing by approximately an order of magnitude) and observed no significant difference in the EPR spectra.

Figure 3 presents the magnetic resonance spectrum for the $ZnGeP_2$:Mn crystal (~2%) measured at a temperature of 25 K by absorption (curve *1*) and by dispersion (by the change in the microwave frequency at the instant of resonance) (curve *2*). A broad unresolved line is seen in the spectrum, which overlaps with the signals of isolated manganese ions shown previously in Fig. 1 (curve *2*) and Fig. 2. In the case of conventional measurements by the absorption of the microwave power (curve *1*), these signals are observed as the derivative; however, the intensity of the broad line was significantly lower than that of the EPR signals of isolated manganese ions. Thus, the signals with broad lines are characterized by anomalously large dispersion and, apparently, belong to clusters of manganese ions occupying zinc positions. It is not excluded that the manganese ions are magnetically ordered. The temperature dependence of the intensity of this signal qualitatively corresponds to the temperature dependence of magnetization observed in [10], where a relatively fast decrease in magnetization was observed for a close concentration of manganese (~2%) in the temperature range of 4–50 K, followed by a smooth decrease in magnetization up to 300 K.

Thus, it is rather probable that at least two types of manganese ions differing in their charge state with respect to the lattice occur in $ZnGeP_2$:Mn (~2%): (i) Mn_{Zn}^{2+}, which may be conceived as a neutral $A^0(3d^5)$ site, and (ii) Mn_{Ge}^{2+} (or Mn_{Ge}^{3+}), which corresponds to the $A^{2-}(3d^5)$ (or $A^{-}(3d^4)$ state in the lattice and represents a double acceptor, similarly to the way the Mn^{2+} state in GaAs represents a negatively charged $A^{-}(3d^5)$ acceptor [2, 3]. It may be suggested that anomalous orientation dependences in the EPR spectra associated with Mn_{Ge} are due to the occurrence of a defect, possibly a hole, delocalized in the vicinity of Mn, which is similar to what takes place in the GaAs:Mn crystal [2, 3]. The broad line with anomalous dispersion most likely

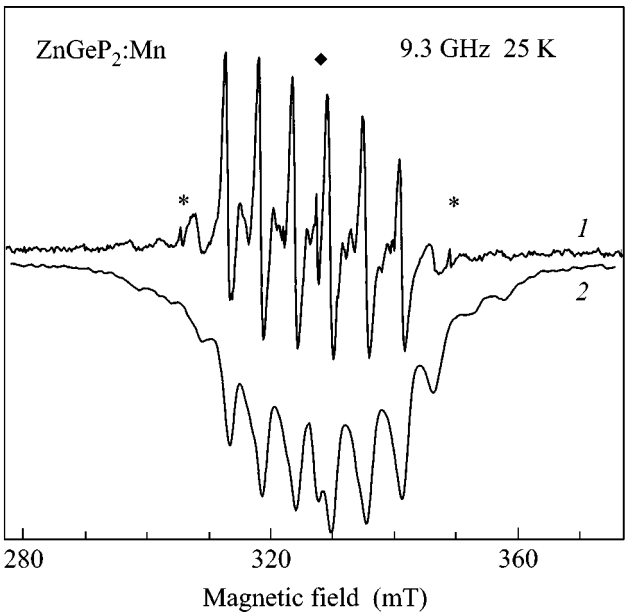

Fig. 3. EPR spectra of the $ZnGeP_2$:Mn crystal containing ~2% Mn measured at 25 K (*1*) by absorption and (*2*) by dispersion. The orientation of the crystal approximately corresponds to an angle of 10° in Fig. 2. The meaning of the narrow lines designated by the rhombus and stars is the same as in Fig. 1.

belongs to Mn_{Zn}^{2+} ions coupled with strong exchange interactions, because the concentration of these ions is high. The HF structure is unresolved because of these interactions. The occurrence of inclusions of the MnP type, which may be responsible for the broad line in a way similar to the inclusions of MnAs in GaMnAs compounds [15], cannot be completely excluded. However, studies of the photoemission of electrons from film samples of $(Zn,Mn)GeP_2$ showed the absence of chemical states typical for the MnP compound.

The results of this work corroborate the theoretical prediction [12] of the existence of stable defects in the material. These defects generate holes, which can form complexes with manganese ions replacing zinc. Hence, it may be suggested that manganese is a self-contained impurity for the creation of a ferromagnetic state, which is in agreement with the theory [12]. At the same time, the conclusion made by the authors of [10] that ferromagnetism in chalcopyrites, as distinct from the GaMnAs system, may not have a hole nature cannot be considered sufficiently justified in light of the results presented in this work.

This work was supported in part by the Russian Foundation for Basic Research, project no. 03-02-17645; the St. Petersburg Committee on Science and Higher Educational Institutions (project no. 8V145); and the program "Physics of Solid-State Nanostructures."

REFERENCES

1. H. Ohno, Science **281**, 951 (1998) and references therein.
2. V. F. Masterov, S. B. Mikhrin, B. E. Samorukov, and K. F. Shtelmakh, Fiz. Tekh. Poluprovodn. (Leningrad) **17**, 1259 (1983) [Sov. Phys. Semicond. **17**, 796 (1983)].
3. J. Schneider, U. Kaufmann, W. Wilkening, *et al.*, Phys. Rev. Lett. **59**, 240 (1987).
4. P. G. Baranov, I. V. Ilyin, and E. N. Mokhov, Solid State Commun. **101**, 611 (1997).
5. U. Kaufmann, A. Raeuber, and J. Schneider, Phys. Status Solidi B **74**, 169 (1976).
6. N. P. Baran, I. I. Tychina, I. G. Tregub, *et al.*, Fiz. Tekh. Poluprovodn. (Leningrad) **9**, 2366 (1975) [Sov. Phys. Semicond. **9**, 1527 (1975)].
7. G. A. Medvedkin, T. Ishibashi, T. Nishi, *et al.*, Jpn. J. Appl. Phys. **39**, L949 (2000).
8. G. A. Medvedkin, K. Hirose, T. Ishibashi, *et al.*, J. Cryst. Growth **236**, 609 (2002).
9. K. Sato, G. A. Medvedkin, and T. Ishibashi, J. Cryst. Growth **237–239**, 1363 (2002).
10. Sunglae Cho, Sungyoul Choi, Gi-Beom Cha, *et al.*, Phys. Rev. Lett. **88**, 257203 (2002).
11. P. G. Baranov, S. I. Goloshchapov, G. A. Medvedkin, *et al.*, J. Supercond. **16**, 131 (2003).
12. Priya Mahadevan and Alex Zunger, Phys. Rev. Lett. **88**, 047205 (2002).
13. A. Abragam and B. Bleaney, *Electron Paramagnetic Resonance of Transition Ions* (Clarendon Press, Oxford, 1970; Mir, Moscow, 1972).
14. S. J. C. H. M. van Gisbergen, M. Godlewski, T. Gregorkiewicz, and C. A. J. Ammerlaan, Phys. Rev. B **44**, 3012 (1991); J. C. M. Henning, Phys. Lett. A **24A**, 40 (1967).
15. K. M. Yu, W. Walukiewicz, T. Wojtowicz, *et al.*, Phys. Rev. B **65**, 201303 (2002).

Translated by A. Bagatur'yants

JETP Letters, Vol. 77, No. 10, 2003, pp. 587–591. From Pis'ma v Zhurnal Éksperimental'noĭ i Teoreticheskoĭ Fiziki, Vol. 77, No. 10, 2003, pp. 691–695.
Original English Text Copyright © 2003 by Fominov, Golubov, Kupriyanov.

Decoherence Due to Nodal Quasiparticles in *d*-wave Qubits¶

Ya. V. Fominov*, **, A. A. Golubov, and M. Yu. Kupriyanov*****

** Landau Institute for Theoretical Physics, Russian Academy of Sciences, Moscow, 117940 Russia*

*** Department of Applied Physics, University of Twente, 7500 AE Enschede, The Netherlands*

**** Nuclear Physics Institute, Moscow State University, Moscow, 119992 Russia*

e-mail: fominov@landau.ac.ru, a.golubov@tn.utwente.nl, mkupr@pn.sinp.msu.ru

Received April 21, 2003

We study the Josephson junction between two *d*-wave superconductors, which is discussed as an implementation of a qubit. We propose an approach to calculate the decoherence time due to an intrinsic dissipative process: quantum tunneling between the two minima of the double-well potential excites nodal quasiparticles, which lead to incoherent damping of quantum oscillations. The decoherence is weakest in the mirror junction, where the contribution of nodal quasiparticles corresponds to the superohmic dissipation and becomes small at small tunnel splitting of the energy level in the double-well potential. For available experimental data, we estimate the quality factor. *© 2003 MAIK "Nauka/Interperiodica".*

PACS numbers: 74.50.+r; 85.25.Cp; 03.67.Pp

Among various candidates for physical implementation of quantum bits, solid-state proposals, and in particular superconducting devices, have a number of advantages, e.g., scalability and variability [1]. Particularly interesting are the so-called quiet qubits, which are intrinsically degenerate, i.e., do not require any external source for maintaining the degeneracy. Such qubits can be realized in systems involving *d*-wave superconductors [2]. Recently, it was experimentally demonstrated that a double-well potential is indeed realized in the Josephson junctions between *d*-wave superconductors [3]. The qubit variable in this case is the phase difference φ across the junction. The energy of the phase qubit has two nontrivial minima as a function of the phase difference (see Fig. 1). Alternatively, a quiet flux qubit can be realized if the spontaneous flux is generated in the loop of *d*-wave superconductors [4]. The two qubit implementations are quite similar; for definiteness we shall speak about the phase qubit.

In such intrinsic qubits, there are also intrinsic mechanisms of decoherence even at low temperatures. The quantum tunneling of the phase between the two minima leads to fluctuating voltage across the junction, which excites quasiparticles. Dissipative current across the interface arises, leading to a finite decoherence time τ_φ. The knowledge of τ_φ is essential for estimating the efficiency of the qubit: short decoherence time makes the qubit senseless, while a long enough decoherence time opens the way for quantum correction algorithms that in principle allow one to perform an infinitely long computation [5].

The relevance of quasiparticle processes at low temperatures is specific for *d*-wave superconductors. In the conventional *s*-wave case, the quasiparticle transport below the gap is suppressed. At the same time, in gapless anisotropic superconductors, the gap vanishes in certain directions (the nodal directions); hence, low-energy quasiparticles appear. In the present letter, we consider a DID Josephson junction (D = *d*-wave superconductor, I = insulator) and study the decoherence due to nodal quasiparticles (quasiparticles moving along the nodal directions).

Decoherence time (general strategy). Theoretical description of the quantum dynamics of a tunnel junction between two *s*-wave superconductors was developed in [6] (see [7] for a review). The effective action for the phase difference φ was obtained. Later this description was generalized to the case of *d*-wave superconductors in [8, 9]. The effective action for φ is

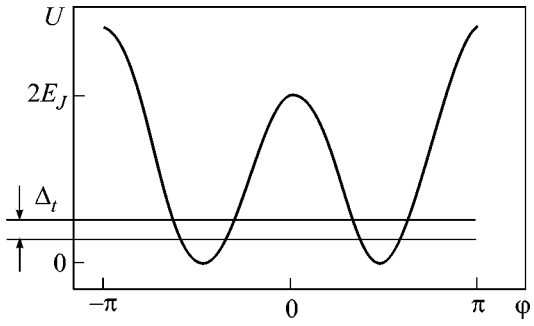

Fig. 1. Schematic dependence of the Josephson energy U on the phase difference φ (in the flux qubit φ is substituted by $2\pi\Phi/\Phi_0$, with Φ_0 the flux quantum). The barrier of the height $2E_J$ separates two nontrivial minima. The splitting of the lowest energy level due to the tunneling across the barrier is denoted Δ_t.

¶ This article was submitted by the authors in English.

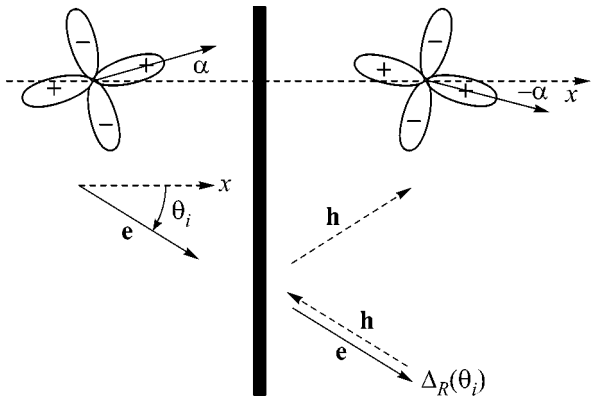

Fig. 2. DID junction of mirror orientation α/–α. An electron **e** moving along a truly nodal direction θ_i of the left superconductor tunnels into an induced nodal direction of the right superconductor. $\Delta_R(\theta_i) \neq 0$, therefore the electron experiences Andreev reflection; the hole **h** returns to the interface and, after reflection at the interface, escapes into the bulk along the truly nodal direction $-\theta_i$. In this process, the total current into the bulk of the right superconductor is composed of the Cooper pair along θ_i and the hole along $-\theta_i$.

similar to the general case considered by Caldeira and Leggett [10, 11], who studied the influence of dissipation on quantum tunneling in macroscopic systems. The dissipation was described as being due to the interaction with a bath of oscillators (the environment). The "strength" of the environment, depending on the frequency ω, is characterized by the spectral function $J(\omega)$. In the Josephson junction, the environment is represented by the quasiparticles, and the spectral function is given by $\hbar I(\hbar\omega/e)/e$, where I is the dissipative quasiparticle current taken at "voltage" $\hbar\omega/e$ [6].

A system living in a double-well potential and described by an extended coordinate can be "truncated" to the two-state system (spin 1/2) with the two states ($\sigma_z = \pm 1$) corresponding to the minima of the potential (see Fig. 1). The theory of dissipative two-state systems is thoroughly elaborated [11] for the cases when the spectral function behaves as $J(\omega) \propto \omega^s$ up to some high-frequency cutoff. The situations when $s = 1$, $s > 1$, and $0 < s < 1$ are called ohmic, superohmic, and subohmic, respectively. In this language, the dissipation due to nodal quasiparticles in the Josephson junction is superohmic, as we demonstrate below.

What is the decoherence in such a system? Assume that during the time $t < 0$ the system is held in the right well (i.e., at $\sigma_z = 1$). At $t = 0$ the constraint is released, and we consider the expectation value of the system coordinate: $P(t) = \langle\sigma_z(t)\rangle$. Below we shall encounter the superohmic case at zero temperature. Then [11]

$$P(t) = \cos(\Delta_t t/\hbar)\exp(-t/\tau_\varphi), \qquad (1)$$

where the cosine describes coherent oscillations between the two wells (Δ_t is the tunnel splitting of levels; see Fig. 1) while the exponential leads to their incoherent damping.

The decoherence time τ_φ is expressed in terms of the spectral function [11]. Returning from the general theory to the particular case of the Josephson junction, we write the corresponding result as

$$\tau_\varphi = \frac{4e}{\delta\varphi^2 I(\Delta_t/e)} = \frac{4\pi\hbar}{\delta\varphi^2 e R_q I(\Delta_t/e)}, \qquad (2)$$

where $\delta\varphi$ is the distance between the potential minima and $R_q = h/2e^2 \approx 13\ \mathrm{k}\Omega$ is the quantum resistance. Comparing the decoherence time with the characteristic time of oscillations between the wells, $\hbar/\Delta_t$, we obtain the quality factor

$$Q = \frac{\tau_\varphi \Delta_t}{2\hbar} = \frac{2\pi\Delta_t}{\delta\varphi^2 e R_q I(\Delta_t/e)}, \qquad (3)$$

which must be large for successful operating of the qubit.

In the DID junction, the tunnel splitting Δ_t is much smaller than the order parameter Δ; hence, τ_φ is determined by the quasiparticle current at low "voltage."

Quasiparticle current. Motivated by experiment [3], we consider the grain-boundary Josephson junction between two quasi-two-dimensional $d_{x^2-y^2}$-wave superconductors with cylindrical Fermi surfaces. The orientations of the superconductors are characterized by the angles between the *a* axes and the normal to the interface (the *x* axis); see Fig. 2. According to [3], we consider the mirror junction, in which the misorientation angles on both sides are equal in magnitude but opposite in sign, α/–α (we take $-45° \le \alpha \le 45°$ because all physically different situations in the mirror junction are realized in this interval). The order parameter depends on the direction (parametrized by the angle θ) and the distance to the interface:

$$\Delta_{L,R}(x, \theta) = \tilde{\Delta}_{L,R}(x) e^{i\varphi_{L,R}} \cos(2(\theta \mp \alpha)), \qquad (4)$$

where the indices L and R refer to the left- and right-hand side of the junction, respectively.

The quasiparticle current in the tunneling limit at low temperatures, $k_B T \ll \hbar\omega$, is given by

$$I(\hbar\omega/e) = \frac{1}{eR_N}\int_{-\pi/2}^{\pi/2} d\theta \frac{D(\theta)\cos\theta}{\tilde{D}} \times \int_0^{\hbar\omega} dE N(E - \hbar\omega, \theta) N(E, \theta), \qquad (5)$$

$$\tilde{D} = \int_{-\pi/2}^{\pi/2} d\theta D(\theta)\cos\theta.$$

Here, R_N is the normal-state resistance of the interface, $N(E, \theta)$ is the density of states (DoS) at the interface normalized to the normal-metal value, and $D(\theta)$ is the angle-dependent transparency of the interface. We have not labeled the DoS by the indices L and R because $N_L(E, \theta) = N_R(E, \theta)$ in the mirror junction.

Below we calculate the nodal contribution to the current (5) at $\hbar\omega \ll \tilde{\Delta}_0$, where $\tilde{\Delta}_0 = \tilde{\Delta}(\pm\infty)$ is the bulk amplitude of the order parameter. The angle integration contributing to the current is then limited to narrow angles around the nodal directions, where the low-energy DoS is nonzero (as we shall see below, the width of the angles is $\delta\theta = \hbar\omega/\tilde{\Delta}_0$).

To calculate the DoS, we employ the quasiclassical approach. The quasiclassical matrix Green's function

$$\hat{G} = \begin{pmatrix} g & f \\ \bar{f} & -g \end{pmatrix} \tag{6}$$

obeys the Eilenberger equation [12] and satisfies the normalization condition $\hat{G}^2 = \hat{1}$. It can be parametrized as

$$g = \frac{1-ab}{1+ab}, \quad f = \frac{2a}{1+ab}, \quad \bar{f} = \frac{2b}{1+ab}. \tag{7}$$

Then the normalization condition is automatically satisfied. The equations for the new functions $a(x, \theta)$ and $b(x, \theta)$ take the form of the Riccati equations [13]:

$$\begin{aligned} \hbar v_F \cos\theta (da/dx) - 2iEa + \Delta^* a^2 - \Delta &= 0, \\ \hbar v_F \cos\theta (db/dx) + 2iEb - \Delta b^2 + \Delta^* &= 0, \end{aligned} \tag{8}$$

where v_F is the absolute value of the Fermi velocity $\mathbf{v}_F$ and θ denotes the angle between $\mathbf{v}_F$ and the x axis.

In the tunneling limit, the DoS is calculated at an impenetrable interface. Let us consider, e.g., the right superconductor (the right half-space). We need to find the low-energy DoS in two cases: (1) in the vicinity of a nodal direction, so that $E, \Delta(\theta) \ll \tilde{\Delta}_0$, and (2) at a gapped direction, so that $E \ll \Delta(\theta)$. In the first case, the spatial scale $\xi_E = \hbar v_F \cos\theta/|\mathscr{E}_+|$ on which the quasiclassical Green's functions vary (we denote $\mathscr{E}_\pm = \sqrt{E^2 - |\Delta(\infty, \pm\theta)|^2}$) is much larger than the coherence length $\xi = \hbar v_F/2\pi k_B T_c$ on which variations of Δ occur. This allows us to regard Δ as constant when integrating Eqs. (8) over x. In other words, the functions a and b at low energies do not feel the suppression of Δ near the interface, because it takes place on a small scale. In the second case, the spatially dependent parts of a and b are proportional to $E/\Delta(\theta) \ll 1$ and hence small. Thus, a and b at the interface are equal to their bulk values, as if Δ was constant.

Thus, we can regard $\Delta(x, \theta)$ as equal to the bulk value $\Delta_0(\theta) = \Delta(\infty, \theta)$. The integration of the functions a and b over x in Eqs. (8) is stable only in the directions determined by the sign of $\cos\theta$. At $\cos\theta > 0$, the function $b(x, \theta)$ is stably integrated from $x = \infty$ to the interface ($x = 0$); hence,

$$b(0, \theta) = b(\infty, \theta) = i(E - \mathscr{E}_+ \operatorname{sgn} E)/\Delta_0(\theta). \tag{9}$$

At the same time at $\cos\theta > 0$, the function a is stably integrated from the interface to $x = \infty$. Therefore, to find $a(0, \theta)$, we consider the trajectory directed along $\pi - \theta$. Since $\cos(\pi - \theta) < 0$, the function a is stably integrated from $x = \infty$ to the interface. Finally, the direction $\pi - \theta$ is converted to θ upon reflection at the specular interface:

$$\begin{aligned} a(0, \theta) &= a(0, \pi - \theta) = a(\infty, \pi - \theta) \\ &= i(E - \mathscr{E}_- \operatorname{sgn} E)/\Delta_0^*(-\theta). \end{aligned} \tag{10}$$

As a result, the DoS $N = \operatorname{Re} g$ at the interface is

$$N(E, \theta) = \operatorname{Re} \frac{|E|(\mathscr{E}_+ + \mathscr{E}_-)}{E^2 - \Delta_0(\theta)\Delta_0^*(-\theta) + \mathscr{E}_+ \mathscr{E}_-}. \tag{11}$$

The gap in the spectrum is $E_g(\theta) = \min(|\Delta_0(\theta)|, |\Delta_0(-\theta)|)$.

The DoS is symmetric, $N(\theta) = N(-\theta)$, because the Green's functions are continuous upon reflection. Thus in each superconductor there are two "truly" nodal directions θ_i ($i = 1, 2$) in the interval $-\pi/2 < \theta < \pi/2$, and also two "induced" nodal directions $-\theta_i$. Near a nodal direction $E_g(\theta) = 2\tilde{\Delta}_0 |\theta - \theta_i|$. Along a truly nodal direction, the gap vanishes and the DoS is the same as in the normal metal, $N(E) = 1$. For an "induced" nodal direction, this is so only near the interface.

In the left superconductor, the truly nodal directions are $\theta_{1,2} = \alpha \pm 45°$. Due to the mirror symmetry, the truly nodal directions of the right superconductor coincide with the induced nodal directions of the left one, and vice versa. In total, there are four nodal directions in the junction, which are symmetric with respect to the interface normal.

In this situation, the transport is due to the processes of the following type. An electron moving along a truly nodal direction θ_i of the left superconductor tunnels into an induced nodal direction of the right superconductor (see Fig. 2). However, the electron cannot escape into the bulk of the right superconductor because $\Delta_R(\theta_i) \neq 0$. Therefore, the electron experiences Andreev reflection; the hole returns to the interface and, after reflection at the interface, escapes into the bulk along the truly nodal direction $-\theta_i$. In this process, the total current into the bulk of the right superconductor is composed of the Cooper pair along θ_i and the hole along $-\theta_i$, which is overall equivalent to the transfer of one electron.

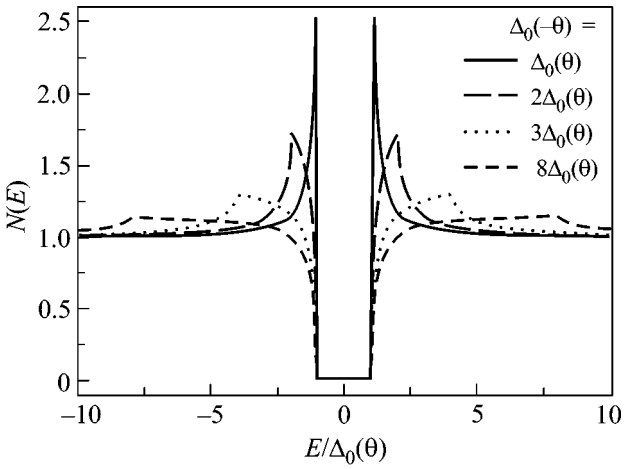

Fig. 3. Density of states following from Eq. (11). The energy is normalized to $\Delta_0(\theta)$, while $\Delta_0(-\theta)$ is varied.

The nodal contribution to the current (5) appears only due to integrating in the vicinity of the nodal directions where $E_g < \hbar\omega$. The DoS near the nodal directions at small energies can be found from Eq. (11). Below, we distinguish the general case when $\Delta_0(\theta) \neq \pm\Delta_0(-\theta)$, and two special cases: $\Delta_0(\theta) = \Delta_0(-\theta)$ (at $\alpha = 0°$) and $\Delta_0(\theta) = -\Delta_0(-\theta)$ (at $\alpha = 45°$).

At $\alpha = 0°$, the truly nodal and induced nodal directions coincide in each superconductor, and Eq. (11) yields the BCS-like DoS:

$$N_{0°}(E, \theta) = \mathrm{Re}(|E|/\sqrt{E^2 - |\Delta_0(\theta)|^2}). \qquad (12)$$

At $\alpha = 45°$, the truly nodal and induced nodal directions again coincide, and Eq. (11) yields the DoS of the inverse BCS type:

$$N_{45°}(E, \theta) = \mathrm{Re}(\sqrt{E^2 - |\Delta_0(\theta)|^2}/|E|). \qquad (13)$$

Finally, if $|\alpha| \gg \hbar\omega/\tilde{\Delta}_0$ and $45° - |\alpha| \gg \hbar\omega/\tilde{\Delta}_0$ (i.e., α is not too close to 0° and ±45°), then $\Delta_0(\theta)$in the essential angle of the width $\delta\theta = \hbar\omega/\tilde{\Delta}_0$ around a nodal direction is much smaller than $\Delta_0(-\theta)$. Then in the region of energies that contribute to the quasiparticle current, $|\Delta_0(\theta)| < |E| < \hbar\omega \ll |\Delta_0(-\theta)|$, the DoS is again given by the inverse BCS formula:

$$N_g(E, \theta \approx \theta_i) = \mathrm{Re}(\sqrt{E^2 - |\Delta_0(\theta)|^2}/|E|). \qquad (14)$$

Figure 3 demonstrates the DoS at different angles θ, which are parametrized by different ratios $\Delta_0(-\theta)/\Delta_0(\theta)$. At $\Delta_0(-\theta) = \Delta_0(\theta)$, the DoS has a BCS-like square-root singularity near E_g [see Eq. (12)]. At $\Delta_0(-\theta) \neq \Delta_0(\theta)$, the DoS has the inverse-BCS behavior near E_g [see Eq. (14)].

Inserting Eqs. (12)–(14) into Eq. (5), we obtain

$$I(\hbar\omega/e) = \frac{A(\alpha)}{eR_N}\frac{(\hbar\omega)^2}{\tilde{\Delta}_0}\sum_{i=1,2}\frac{D(\theta_i)\cos\theta_i}{\tilde{D}}, \qquad (15)$$

where $\theta_{1,2} = \alpha \pm 45°$ and A is a number that depends on the orientation of crystals: $A(0°) \approx 0.46$, $A(45°) \approx 0.19$, and $A(\alpha) \approx 2A(45°) \approx 0.37$ when α is not too close to 0° or ±45°.

In [8, 9], the quadratic current–voltage characteristic, $I \propto \omega^2$, was obtained for the case of aligned nodal directions (i.e., for the α/α orientation).

Estimate. Equations (3) and (15) yield

$$Q = \left(\frac{2\pi}{\delta\varphi^2 A(\alpha)\sum_{i=1,2} D(\theta_i)\cos\theta_i/\tilde{D}}\right)\frac{R_N}{R_q}\frac{\tilde{\Delta}_0}{\Delta_t}. \qquad (16)$$

To proceed further, we need to estimate the tunnel splitting Δ_t (see Fig. 1). For the estimate, we assume that the second harmonic dominates in the energy–phase relation, $U(\varphi) = E_J(1 + \cos2\varphi)$, and the energy of the levels is small compared to E_J. Then the tunneling action is calculated between the points $\varphi = -\pi/2$ and $\pi/2$, and we obtain

$$\Delta_t = (4\sqrt{2E_JE_C}/\pi)\exp(-\sqrt{2E_J/E_C}), \qquad (17)$$

where $E_C = e^2/2C$ is the charging energy (C is the capacitance of the junction).

To obtain a numerical estimate, we take the characteristics of the junction as in the experiment of Il'ichev *et al.* [3]. The capacitance of the junction is $C \sim 10^{-14}$ F [14]; hence, $E_C/k_B \sim 0.1$ K. The characteristic Josephson energy is on the order of several Kelvin. For an estimate, we take $2E_J/k_B = 7$ K. The resistance of the interface is $R_N \sim 50\ \Omega$ [14].

As a result, $\Delta_t/k_B \sim 2.5 \times 10^{-4}$ K. Finally, we estimate $\delta\varphi \sim \pi$, $\tilde{\Delta}_0/k_B \sim 200$ K, and assume a thin δ-functional barrier with $D(\theta) = D_0\cos^2\theta$; then the quality factor is $Q \sim 10^3$–10^4. Here we have retained only the order of magnitude for Q, because we cannot expect a higher accuracy in the case when important characteristics of the junction (e.g., N and E_J) are known only by the order of magnitude. We also made an essential assumption that the second Josephson harmonic dominates.

The latter assumption can be realized under special conditions, while in a more common situation the first and the second harmonics are on the same order. Estimates for this case were made in a recent work [15], where the characteristics of mesoscopic junctions between high-T_c superconductors were experimentally studied and theoretically analyzed. A characteristic value of $\Delta_t \sim 0.1$ K was reported under the conditions that correspond to $R_N \sim 100\ \Omega$. Assuming such parameters for the mirror junction, we obtain $Q \sim 10$–10^2.

The above estimates for Q are very different. At the same time, a general consequence of Eq. (16) is that the quality factor grows as the splitting Δ_t becomes smaller. We note in this respect that the values of the critical current (and hence the Josephson energy) measured in [3, 15], are much smaller than expected. If the critical current is enhanced to the expected value, then Δ_t decreases, which finally leads to an increase in Q.

If $\alpha \neq 0°$, the low-energy quasiparticles are represented not only by the nodal quasiparticles, but also by the midgap states (MGS) with zero energy [16]. In the case of specular interface and clean superconductors considered in this paper, the DoS corresponding to the MGS is proportional to $\delta(E)$; hence, the MGS on the two sides of the interface do not overlap and do not contribute to the current at a finite voltage.

In the asymmetric case, when $\alpha_L \neq \pm\alpha_R$ (precisely speaking, when $||\alpha_L| - |\alpha_R|| > \hbar\omega/\tilde{\Delta}_0$), the nodal directions of the left and right superconductors do not match each other. Then the transport from nodal to nodal direction is suppressed. However, a more important transport "channel" arises between the nodal directions and the MGS. This leads to a stronger decoherence than in the symmetric case.

In the mirror junction, the MGS contribute to the quasiparticle current if they are split and/or broadened [17]. To take into account the contribution of the MGS into decoherence, the present approach should be considerably modified. This issue requires a separate study.

In conclusion, we have proposed an approach that allows to calculate the decoherence time due to nodal quasiparticles in the DID junctions, which can be used as phase or flux qubits. The dissipation in the mirror junctions is weaker than in the asymmetric ones. We find the superohmic dissipation with $s = 2$ in the mirror junction, which becomes weak at small tunnel splitting of the energy level in the double-well potential. For available experimental data, we estimate the quality factor.

The superohmic case is most favorable (compared to ohmic and subohmic) for possible qubit applications.

We thank M.V. Feigel'man for careful reading and comments on the manuscript. We are indebted to A.Ya. Tzalenchuk for communicating the results of his group to us before publication. We are grateful to M.H.S. Amin, Y. Makhlin, A. Shnirman, and A.M. Zagoskin for helpful discussions. The research was supported by the D-Wave Systems, Inc. and the ESF PiShift program Ya.V.F. was also supported by the Russian Foundation for Basic Research, grant no. 01-02-17759; the Swiss National Foundation; the Russian Ministry of Industry, Science and Technology (RMIST); and the program "Quantum Macrophysics" of the Russian Academy of Sciences. M.Yu.K. was also supported by RMIST.

REFERENCES

1. Y. Makhlin, G. Schön, and A. Shnirman, Rev. Mod. Phys. **73**, 357 (2001); G. Blatter, V. B. Geshkenbein, and L. B. Ioffe, Phys. Rev. B **63**, 174511 (2001).
2. L. B. Ioffe, V. B. Geshkenbein, M. V. Feigel'man, *et al.*, Nature **398**, 679 (1999); A. M. Zagoskin, cond-mat/9903170 (1999); A. Blais and A. M. Zagoskin, Phys. Rev. A **61**, 042308 (2000).
3. E. Il'ichev, M. Grajcar, R. Hlubina, *et al.*, Phys. Rev. Lett. **86**, 5369 (2001).
4. C. C. Tsuei, J. R. Kirtley, C. C. Chi, *et al.*, Phys. Rev. Lett. **73**, 593 (1994).
5. M. Nielsen and I. Chuang, *Quantum Computation and Quantum Information* (Cambridge Univ. Press, Cambridge, 2000).
6. U. Eckern, G. Schön, and V. Ambegaokar, Phys. Rev. B **30**, 6419 (1984).
7. G. Schön and A. D. Zaikin, Phys. Rep. **198**, 237 (1990).
8. C. Bruder, A. van Otterlo, and G. T. Zimanyi, Phys. Rev. B **51**, 12904 (1995).
9. Yu. S. Barash, A. V. Galaktionov, and A. D. Zaikin, Phys. Rev. B **52**, 665 (1995).
10. A. O. Caldeira and A. J. Leggett, Phys. Rev. Lett. **46**, 211 (1981).
11. A. J. Leggett, S. Chakravarty, A. T. Dorsey, *et al.*, Rev. Mod. Phys. **59**, 1 (1987).
12. G. Eilenberger, Z. Phys. **214**, 195 (1968).
13. N. Schopohl and K. Maki, Phys. Rev. B **52**, 490 (1995); N. Schopohl, cond-mat/9804064 (1998).
14. M. Grajcar, private communication.
15. A. Ya. Tzalenchuk, T. Lindström, S. A. Charlebois, *et al.*, Phys. Rev. B (in press).
16. C.-R. Hu, Phys. Rev. Lett. **72**, 1526 (1994).
17. Y. Tanaka and S. Kashiwaya, Phys. Rev. B **53**, 9371 (1996); R. A. Riedel and P. F. Bagwell, Phys. Rev. B **57**, 6084 (1998); Yu. S. Barash, Phys. Rev. B **61**, 678 (2000); A. A. Golubov and M. Yu. Kupriyanov, Pis'ma Zh. Éksp. Teor. Fiz. **69**, 242 (1999) [JETP Lett. **69**, 262 (1999)]; A. Poenicke, Yu. S. Barash, C. Bruder, and V. Istyukov, Phys. Rev. B **59**, 7102 (1999).

JETP Letters, Vol. 77, No. 10, 2003, pp. 592–597. Translated from Pis'ma v Zhurnal Éksperimental'noĭ i Teoreticheskoĭ Fiziki, Vol. 77, No. 10, 2003, pp. 696–701.
Original Russian Text Copyright © 2003 by Trunin, Nefedov.

Anisotropy of Microwave Conductivity in the Superconducting and Normal States of $YBa_2Cu_3O_{7-x}$: 3D–2D Crossover

M. R. Trunin* and Yu. A. Nefedov

Institute of Solid State Physics, Russian Academy of Sciences, Chernogolovka, Moscow region, 142432 Russia

**e-mail: trunin@issp.ac.ru*

Received April 23, 2003

The imaginary parts of microwave conductivity σ'' ($T < T_c$) and resistivity $\rho(T) = 1/\sigma(T > T_c)$ along (σ''_{ab} and ρ_{ab}) and across (σ''_c and ρ_c) the cuprate *ab* planes of a $YBa_2Cu_3O_{7-x}$ crystal with the oxygen doping level x varying from 0.07 to 0.47 were measured in the temperature range $5 \le T \le 200$ K. In the superconducting state, the $\sigma''_{ab}(T)/\sigma''_{ab}(0)$ and $\sigma''_c(T)/\sigma''_c(0)$ curves coincide for an optimally doped ($x = 0.07$) crystal, but, with an increase in x, the slopes of the $\sigma''_c(T)/\sigma''_c(0)$ curves decrease noticeably at $T < T_c/3$, on the background of small changes happening to the $\sigma''_{ab}(T)/\sigma''_{ab}(0)$ curves. The two-dimensional (2D) transport along the *ab* planes in the normal state of $YBa_2Cu_3O_{7-x}$ is always metallic, but there is a crossover (at $x = 0.07$) from the Drude to hopping (at $x > 0.07$) conductivity along the *c* axis. This is confirmed both by the estimates of the lowest metallic and the highest tunneling conductivities along the *c* axis and by quantitative comparison of the measured $\rho_c(T)$ curves with the curves calculated in the polaron model of quasiparticle transport along the *c* axis. © *2003 MAIK "Nauka/Interperiodica".*

PACS numbers: 74.25.Fy; 74.72.Bk

In recent years, growing interest has been shown in the evolution of transport properties of high-temperature superconductors (HTSCs) upon changing the level of doping with oxygen and other substitutional impurities or, in other words, upon changing the hole concentrations p per one copper atom in the CuO_2 plane. The p value and the superconducting transition temperature T_c in HTSC are related by the empirical formula [1] $T_c = T_{c,\max}[1 - 82.6(p - 0.16)^2]$.

A narrow region in the phase diagram of an optimally doped HTSC ($p \approx 0.16$) with maximal critical temperatures $T_c = T_{c,\max}$ has received most attention. In the normal state of an optimally doped HTSC, the resistivity $\rho_{ab}(T)$ in the cuprate *ab* planes increases linearly with temperature, $\Delta\rho_{ab}(T) \propto T$. The quantity $\rho_{ab}(T)$ is much smaller than the resistivity $\rho_c(T)$ in the perpendicular direction, which also has a metallic character (the derivatives of $\rho_{ab}(T)$ and $\rho_c(T)$ with respect to temperature are positive). The exception is provided by the most anisotropic HTSC compound Bi-2212 (the corresponding ratio is $\rho_c/\rho_{ab} \approx 10^5$ at $p \approx 0.16$), for which the resistivity $\rho_c(T)$ increases as T approaches T_c ($d\rho_c(T)/dT < 0$). This property of Bi-2212 agrees with the estimate of the lowest possible metallic conductivity in the *c* direction for anisotropic three-dimensional (3D) Fermi-liquid model [2]:

$$\sigma^{3D}_{c,\min} = \sqrt{\rho_{ab}/\rho_c}\, ne^2d^2/h, \qquad (1)$$

where $n \approx 10^{21}$ cm^{-3} is the carrier concentration, d is the lattice constant along the *c* axis, and h is Planck's constant. In Bi-2212, the conductivity $\sigma_c = 1/\rho_c \ll \sigma^{3D}_{c,\min}$ at $T = T_c$, but, in other optimally doped HTSCs, $\sigma_c(T) > \sigma^{3D}_{c,\min}(T_c)$. The conductivity $\sigma_{c,\min}$ in Eq. (1) is lower than the two-dimensional Ioffe–Regel limiting value $\sigma_{IR} = e^2k_F/h$: $\sigma_{c,\min} \approx \sqrt{\rho_{ab}/\rho_c}\,\sigma_{IR}d/a \ll \sigma_{IR}$ ($a \approx 2\pi/k_F$ is the lattice constant in the CuO_2 plane), whereas $\sigma_{ab,\min} \approx \sigma_{IR}$ [2].

The ratio of the superconducting liquid densities in the cuprate planes and in the perpendicular direction serves as a measure of HTSC anisotropy in the superconducting state. This ratio equals $\sigma''_{ab}(0)/\sigma''_c(0) = \lambda^2_c(0)/\lambda^2_{ab}(0)$, where σ''_{ab} and σ''_c are the imaginary parts of the corresponding conductivities and λ_{ab} and λ_c are the microwave-field penetration depths for the currents flowing, respectively, in the *ab* planes and perpendicularly to them. It is well known that, in high-quality optimally doped HTSC single crystals, $\Delta\lambda_{ab}(T) \propto T$ at $T < T_c/3$, and this experimental fact suggests a $d_{x^2-y^2}$ symmetry of the order parameter in them [3]. There is no agreement in the literature about the low-temperature behavior of $\Delta\lambda_c(T)$. Both the linear dependence $\Delta\lambda_c(T) \propto T$ at $T < T_c/3$ [4–6] and the quadratic dependence [7] have been observed for the most studied $YBa_2Cu_3O_{6.95}$ ($T_c \approx 93$ K) single crystals.

0021-3640/03/7710-0592$24.00 © 2003 MAIK "Nauka/Interperiodica"

Annealing temperatures, doping parameters, and characteristics of the superconducting and normal states of $YBa_2Cu_3O_{7-x}$

Annealing temperature T, °C	Critical temperature T_c, °C	Doping parameters		λ values at $T = 0$		$\Delta\lambda_c(T) \propto T^\alpha$ α	λ_c/λ_{ab} at $T = 0$	$\sqrt{\rho_c/\rho_{ab}}$ at $T = 200$ K
		p	x	λ_{ab}, nm	λ_c, μm			
500	92	0.15	0.07	152	1.55	1.0	10	11
520	80	0.12	0.26	170	3.0	1.1	18	18
550	70	0.105	0.33	178	5.2	1.2	29	16
600	57	0.092	0.40	190	6.9	1.3	36	16
720	41	0.078	0.47	198	16.3	1.8	83	35

A broad region of pseudogap states arising in the HTSC phase diagram at concentrations $p < 0.16$ has been studied to a much lesser extent. It follows from the measurements of dynamic susceptibility of oriented HTSC powders at $T < T_c$ [8] that, at $T \longrightarrow 0$, the slopes of $\sigma_c''(T)/\sigma_c''(0)$ for $\sigma_{ab}''(T)/\sigma_{ab}''(0)$. The nonmetallic behavior of resistivity $\rho_c(T)$ as T approaches T_c, the deviations from the linear dependence $\Delta\rho_{ab}(T) \propto T$, and a dramatic increase in the ratio ρ_c/ρ_{ab} with decreasing concentration p are common properties of underdoped HTSCs in their normal state. Although many theoretical models have been proposed for the explanation of these properties, none of them describes in full measure the evolution of the $\sigma_{ab}''(T)$, $\sigma_c''(T)$, $\rho_{ab}(T)$, and $\rho_c(T)$ curves over a wide range of concentrations and temperatures. The transport mechanism along the c axis has also not been established, and, in particular, it still remains unclear whether it can be metallic (of the Drude type) or whether the conductivity for any p is caused by the quasiparticle tunneling between the cuprate layers with scattering both within the layers and between them.

In this work, the anisotropy and evolution of temperature dependences of the conductivity components of $YBa_2Cu_3O_{7-x}$ with oxygen doping in the range $0.07 \le x \le 0.47$ were measured and the measurement results were analyzed. The crystal was grown in a $BaZrO_3$ crucible and had a rectilinear shape with sizes $1.6 \times 0.4 \times 0.1$ mm. Measurements were performed at a frequency $\omega/2\pi = 9.4$ GHz and temperatures $5 \le T \le 200$ K. The oxygen content in the sample changed through the controlled annealing in air at different temperatures $T \ge 500$°C (listed in the table). Measurements of the conductivity anisotropy were carried out for each of the five crystal states, in which the superconducting transition width, according to the susceptibility measurements at a frequency of 100 kHz, was 0.1 K in the optimally doped ($x = 0.07$) state and increased with x to reach 4 K at $x = 0.47$. The superconducting transition temperatures were $T_c = 92$, 80, 70, 57, and 41 K. The full cycle of microwave studies included (i) measurements of the temperature dependences of the Q value and the frequency shift for a superconducting niobium cavity with crystal samples in two, transverse and longitudinal, orientations about the microwave magnetic field; (ii) determination of the surface resistance $R_{ab}(T)$, reactance $X_{ab}(T)$, and conductivity $\sigma_{ab}(T)$ of the cuprate planes in the normal and superconducting states from the measurements in the first orientation; and (iii) determination of $\sigma_c(T)$, $X_c(T)$, and $R_c(T)$ using the data obtained for the longitudinal orientation. The entire measurement procedure for the optimally doped $YBa_2Cu_3O_{6.95}$ crystal is described in detail in [6]. The temperature dependences of the components of surface impedance of $YBa_2Cu_3O_{7-x}$ at different x were reported in our short communication [9].

The $\sigma_{ab}''(T)/\sigma_{ab}''(0)$ (light symbols) and $\sigma_c''(T)/\sigma_c''(0)$ (dark symbols) curves at $T \le T_c$ are presented in Fig. 1 for the $YBa_2Cu_3O_{7-x}$ crystal in the states with $T_c = 92$, 70, and 41 K. The field penetration depths $\lambda_{ab}(0)$ and $\lambda_c(0)$ at $T = 0$ are also given in the table. The overall temperature behavior of the $\sigma_{ab}''(T)/\sigma_{ab}''(0)$ curves changes only slightly upon varying p. A distinctive feature of the optimally doped $YBa_2Cu_3O_{6.93}$ state is that the temperature dependences $\sigma_{ab}''(T)/\sigma_{ab}''(0)$ and $\sigma_c''(T)/\sigma_c''(0)$ coincide to a good accuracy. This fact can be rigorously explained only in the theory of linear response of an anisotropic 3D superconductor [8]. As p decreases, the $\sigma_c''(T)/\sigma_c''(0)$ dependence at $T < T_c/3$ becomes noticeably weaker than $\sigma_{ab}''(T)/\sigma_{ab}''(0)$.

The model proposed in [10] is most suitable for a comparison with the experimental data of our work. In this model, the following contributions to the quasiparticle transport along the c axis in the superconducting and normal HTSC states are considered: (a) direct hopping between the cuprate planes and (b) hopping with inelastic scattering from impurities located between the planes. The conductivity within the cuprate planes is assumed to be of the Drude type:

$$\sigma_{ab} = \frac{e^2 \nu_{2D} D_{ab}}{d} = \frac{n_{2D} e^2 \tau}{md}, \qquad (2)$$

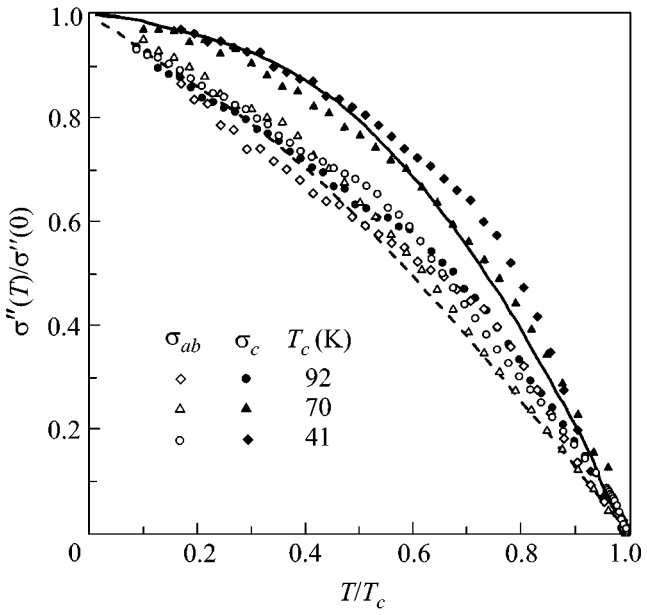

Fig. 1. The $\sigma''_{ab}(T)/\sigma''_{ab}(0)$ (light symbols) and $\sigma''_c(T)/\sigma''_c(0)$ (dark symbols) measured curves for three states of a $YBa_2Cu_3O_{7-x}$ crystal with T_c = 92, 70, and 41 K. The solid and dashed lines correspond, respectively, to the $\sigma''_c(T)/\sigma''_c(0)$ and $\sigma''_{ab}(T)/\sigma''_{ab}(0)$ dependences calculated in [10] for oxygen-deficient $YBa_2Cu_3O_{7-x}$.

where $\nu_{2D} = m/\pi\hbar^2$ is the two-dimensional density of states per unit area and $D_{ab} = v_F^2\tau/2$, v_F, τ, and $n_{2D} = k_F^2/2\pi$ are the diffusion coefficient, Fermi velocity, relaxation time, and two-dimensional quasiparticle density in the *ab* plane, respectively. The total Hamiltonian of the electron system in model [10] is the sum $\sum_m H_m$ of the Hamiltonians of individual (m) CuO_2 layers and the interplane Hamiltonian $H_\perp$, which is assumed to be small compared to $\sum_m H_m$. As a result, the second-order perturbative quasiparticle transport between the neighboring weakly bonded layers proves to be analogous to the tunneling through the *SIS* junction at $T < T_c$ and through the *NIN* junction at $T > T_c$. In this case, the *ab* component of electron momentum is conserved in process (a) (mirror tunneling) and is not conserved in process (b) (diffuse tunneling) [11].

The calculations of the anisotropy of the superconducting HTSC state were carried out in [10] using the BCS model with a *d*-symmetry order parameter in the CuO_2 layers. The $\sigma''_c(T)/\sigma''_c(0)$ curve numerically calculated with allowance for both processes (a) and (b) is shown in Fig. 1 by the solid line and the same for $\sigma''_{ab}(T)/\sigma''_{ab}(0)$ is shown by the dashed line. A comparison with the experimental data obtained at $T < T_c/2$ for $YBa_2Cu_3O_{7-x}$ with an oxygen deficiency $x > 0.07$ clearly demonstrates that the slopes of the $\sigma''_c(T)/\sigma''_c(0)$ curves strongly decrease with increasing x, while the $\sigma''_{ab}(T)/\sigma''_{ab}(0)$ curves change only slightly. The fact that the experimental curves at $T > T_c/2$ are steeper than the theoretical ones may be caused by the strong electron–phonon interaction [3], which was not taken into account in [10]. The dashed line in Fig. 1 coincides also with the $\sigma''_c(T)/\sigma''_c(0)$ curve calculated in [10] for the case where there is no diffuse tunneling (b) and the remaining mirror-tunneling regime (a) along the *c* axis becomes identical with the transport along *c* in an anisotropic 3D superconductor. This exceptional situation corresponds to the optimally doped $YBa_2Cu_3O_{6.93}$.

The real and imaginary parts of the surface impedance measured for the $YBa_2Cu_3O_{7-x}$ crystal at $T > T_c$ coincided with each other; i.e., $R_{ab}(T) = X_{ab}(T)$ and $R_c(T) = X_c(T)$ for each x from the table [9]. Because of this, the resistivities $\rho_{ab}(T)$ and $\rho_c(T)$ were derived from $R_{ab}(T)$ and $R_c(T)$ using the standard formulas for the normal skin effect: $\rho_{ab}(T) = 2R_{ab}^2(T)/\omega\mu_0$ and $\rho_c(T) = 2R_c^2(T)/\omega\mu_0$. The evolution of the $\rho_{ab}(T)$ and $\rho_c(T)$ curves with changing x is shown in Fig. 2 for the temperature range $T_c < T \le 200$ K, and the $(\rho_c/\rho_{ab})^{1/2}$ values at T = 200 K are given in the last column of the table. The $\rho_{ab}(T)$ and $\rho_c(T)$ dependences have a metallic character only in optimally doped $YBa_2Cu_3O_{6.93}$, and the ρ_c/ρ_{ab} ratio approximately corresponds to the anisotropy of charge-carrier effective masses $m_c/m_{ab} = \lambda_c^2(0)/\lambda_{ab}^2(0)$ in a pure 3D London superconductor, to which $YBa_2Cu_3O_{6.93}$ belongs. In all other $YBa_2Cu_3O_{7-x}$ states with a lower hole concentration, the resistivity $\rho_c(T)$ increases with temperature decreasing, demonstrating the nonmetallic behavior. In Fig. 3, the experimental $\sigma_c(T)$ dependences are compared with the $\sigma_{c,\min}^{3D}$ values calculated by Eq. (1) for three states of the $YBa_2Cu_3O_{7-x}$ crystal: T_c = 92 K (dashed line), T_c = 70 K (dotted line), and T_c = 41 K (dot-and-dash line). Over the entire temperature interval, the $YBa_2Cu_3O_{6.93}$ conductivity along *c* is the only one that exceeds the minimal metallic value of $\sigma_{c,\min}^{3D}$.

Thus, it is natural to assume that, as in the case of the superconducting state of $YBa_2Cu_3O_{7-x}$, a small decrease in the carrier concentration from its optimal level in the normal state leads to a crossover from the 3D metallic conduction to the 2D Drude conduction in the CuO_2 layers and tunneling conduction between the layers (3D–2D crossover). To analyze this assumption, it is convenient to again use model [10]. If $t_\perp$ is the hop-

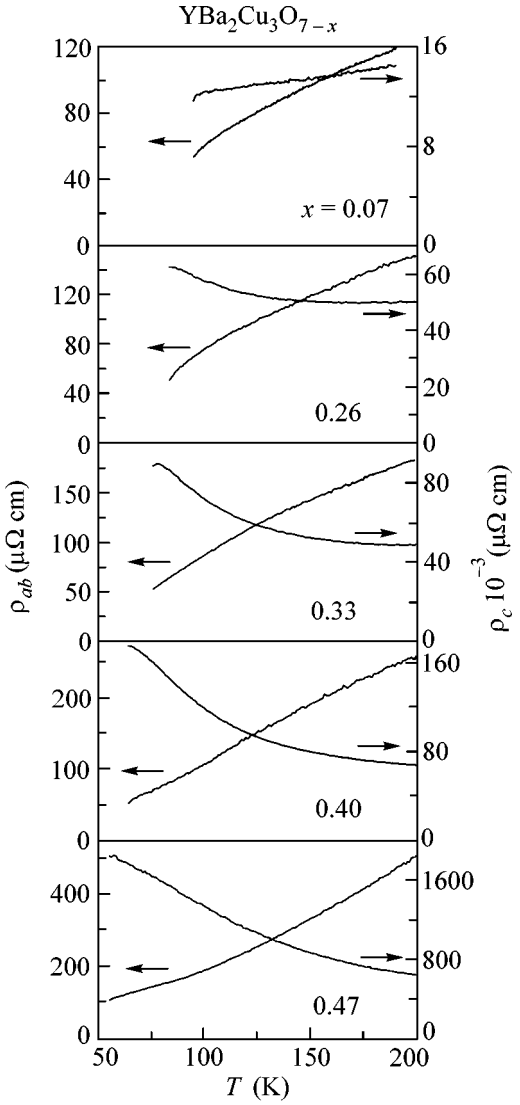

Fig. 2. Evolution of the $\rho_{ab}(T)$ and $\rho_c(T)$ dependences measured for $YBa_2Cu_3O_{7-x}$ with differing oxygen content.

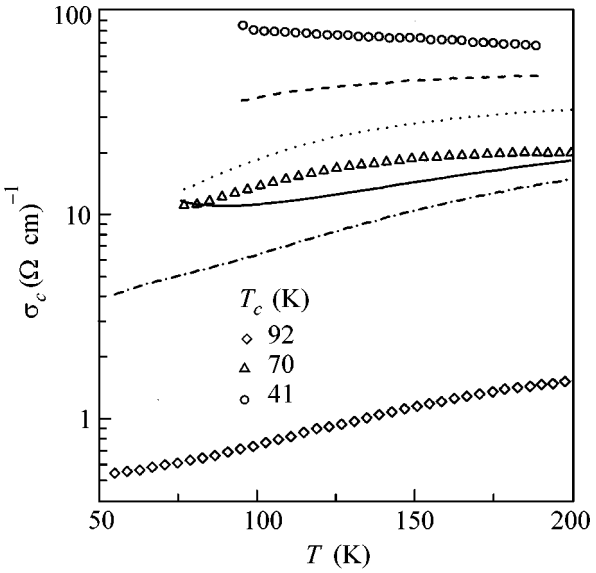

Fig. 3. Symbols correspond to the experimental $\sigma_c(T)$ dependences for three $YBa_2Cu_3O_{7-x}$ states with T_c = 92, 70, and 41 K. The dashed, dotted, and dot-and-dash lines are for the corresponding $\sigma^{3D}_{c,\min}(T)$ values obtained from Eq. (1) using the measured $\rho_{ab}(T)$ and $\rho_c(T)$ presented in Fig. 2. The solid line corresponds to $\sigma_c(T)$ calculated for $YBa_2Cu_3O_{6.67}$ by the formulas given in [10].

ping matrix element, the quasiparticle conductivity along *c* in process (a) will be [10–13]

$$\sigma_c^{\rm dir} = 2e^2\tau\nu_{2D}\left(\frac{t_\perp}{\hbar}\right)^2 = 4\sigma_{ab}\left(\frac{t_\perp d}{\hbar v_F}\right)^2, \qquad (3)$$

where $2\tau(t_\perp/\hbar)^2$ is the direct-tunneling rate between the neighboring CuO_2 planes and σ_{ab} is the conductivity along these planes (Eq. (2)). In this case, the characteristic hopping time $\hbar/t_\perp$ appreciably exceeds the in-plane relaxation time τ [11]: $\hbar/t_\perp \gg \tau$. In the reverse limit $\hbar/t_\perp \ll \tau$, the conductivity is of the Drude type in all directions, as in the case of an anisotropic 3D metal. The crossover occurs when $\hbar/t_\perp \approx \tau$. At this point, the tunneling conductivity along *c* (Eq. (3)) reaches its maximum $\sigma^{\rm dir}_{c,\max} = 2\sigma_{IR}\sqrt{\rho_{ab}/\rho_c}$, which is approximately equal to the minimal metallic conductivity $\sigma^{3D}_{c,\max}$ given by Eq. (1). In the case of diffuse quasiparticle tunneling (processes (b)) in model [10], the conductivity along the *c* axis equals [11, 14]

$$\sigma_c^{\rm diff} = \frac{e^2\nu_{2D}D_c}{d} = \frac{e^2\nu_{2D}d}{\tau_c}, \qquad (4)$$

where $D_c = d^2\tau_c$ is the diffusion coefficient and $1/\tau_c$ is the scattering probability between the cuprate planes. As in the preceding case, we find that $\sigma^{\rm diff}_{c,\max} = \sigma_{IR}\sqrt{\rho_{ab}/\rho_c} \approx \sigma^{3D}_{c,\min}$ for $\tau_c \approx \tau$, and, using Eqs. (2) and (4), we arrive at the following alternative form of the criterion for a 3D–2D crossover:

$$\sigma_{c,\max}\sigma_{ab} \approx \frac{n_{2D}}{\pi}\left(\frac{e^2}{\hbar}\right)^2. \qquad (5)$$

From Eq. (5) it follows that, at $n_{2D} = n/d \approx 10^{14}$ cm^{-2}, the 3D–2D crossover occurs upon reaching the value $\rho_c\rho_{ab} \approx 10^{-6}$ (Ω cm)^2. Returning to the data in Fig. 2, we make sure that the product $\rho_c\rho_{ab} \lesssim 10^{-6}$ (Ω cm)^2 only at $x = 0.07$, thereby substantiating the applicability of the anisotropic 3D Fermi-liquid model for explaining the properties of optimally doped $YBa_2Cu_3O_{6.93}$.

Equations (3) and (4) account for the basically different temperature dependences of the conductivity

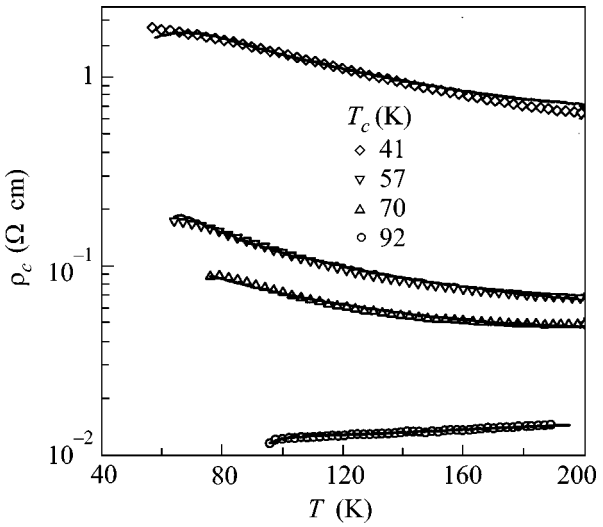

Fig. 4. Comparison of the (symbols) experimental and (solid lines) calculated (by formula (6)) $\rho_c(T)$ dependences for $YBa_2Cu_3O_{7-x}$.

along the *c* axis at $T \geq T_c$; for the direct tunneling, $\sigma_c^{\text{dir}}(T) \propto \sigma_{ab}(T)$ increases with increasing $\tau(T)$ as T approaches T_c, whereas $\sigma_c^{\text{diff}}(T)$ decreases with increasing $\tau_c(T)$. According to model [10], the total conductivity σ_c along the *c* axis is the sum of conductivities caused by each of the above-mentioned processes ((a) and (b)). Near the T_c temperatures, σ_c^{diff} is mainly due to the quasiparticle scattering from the impurities located between the cuprate planes and, hence, is independent of *T*, because the phonon contribution to σ_c^{diff} is frozen out. Quite the reverse, the phonon contribution becomes dominant at $T \gg T_c$. As a result, the temperature dependence of the conductivity $\sigma_c(T)$ takes an approximate form, $A/T + C + BT$ (*A*, *B*, and *C* are independent of *T*), that does not describe the experimental data; an example of $\sigma_c(T)$ calculated by the formulas given in [10] is shown by the solid line in Fig. 3 for the $YBa_2Cu_3O_{6.67}$ sample.

However, all $\rho_c(T)$ dependences shown in Fig. 2 can be described by the *c*-transport model that was recently proposed in [15]. Contrary to [10], where the electron–phonon effects appeared in the second-order of the perturbation theory, the model Hamiltonian [15] includes them through the canonical transformation [16], after which the interplane quasiparticle tunneling can be considered as a perturbation of the originally strongly coupled electron–phonon system. This approach applies if $\epsilon_F \gg \omega_0 \gg t_\perp$, where ϵ_F is the Fermi energy and ω_0 is the characteristic phonon energy. Both inequalities are fulfilled for the layered anisotropic HTSCs, in which, according to [15], an electron moving in the *c* direction is enveloped by a large number of phonons to form polaron [17] that only weakly affects the transverse *ab* transport. For the Einstein spectrum of *c*-polarized phonons, one has

$$\rho_c(T) \propto \rho_{ab}(T)\frac{\exp[g^2\tanh(\omega_0/4T)]}{\sqrt{\sinh(\omega_0/2T)}}, \qquad (6)$$

where *g* ($g > 1$) is the parameter characterizing the electron–phonon coupling strength. The comparison of the experimental data (symbols) with the $\rho_c(T)$ dependences calculated by Eq. (6) (solid lines) is demonstrated in Fig. 4. In the calculations, the data given for $\rho_{ab}(T)$ in Fig. 2 were used. The parameter *g* was almost identical ($g \approx 3$) for all curves in Fig. 4, and ω_0 increased from 110 K (75 cm^{-1}) to 310 K (215 cm^{-1}) upon decreasing the oxygen content ($7 - x$) in $YBa_2Cu_3O_{7-x}$ from 6.93 to 6.53. It seems not surprising that the anomalies of the optical *c* conductivity were observed for a $YBa_2Cu_3O_{7-x}$ crystal with oxygen deficiency just in the indicated range of frequencies ω_0 [18].

In summary, the anisotropy of microwave conductivity was measured for a $YBa_2Cu_3O_{7-x}$ crystal in which the hole concentration *p* was varied in the range $0.08 \leq p \leq 0.15$. An analysis of the temperature dependences of the imaginary parts of the conductivity tensor $\hat{\sigma}''(T)$ in the superconducting state and the resistivity $\hat{\rho}(T)$ in the normal state indicates that optimally doped $YBa_2Cu_3O_{6.93}$ is a three-dimensional anisotropic metal. A decrease in the carrier concentration leads to a crossover from the Drude-type to hopping conduction along the *c* axis. In order to quantitatively describe the evolution of the $\sigma_c''(T)$ and $\rho_c(T)$ dependences with changing *p*, the effects of strong electron–phonon interaction must be taken into account.

We are grateful to V.F. Gantmakher and A.F. Shevchun for helpful discussions. This work was supported by the Russian Foundation for Basic Research, project nos. 03-02-16812, 03-02-06386, and 02-02-08004.

REFERENCES

1. J. L. Tallon, C. Bernhard, H. Shaked, *et al.*, Phys. Rev. B **51**, 12911 (1995).
2. Y. B. Xie, Phys. Rev. B **45**, 11375 (1992).
3. M. R. Trunin and A. A. Golubov, in *Spectroscopy of High-T_c Superconductors. A Theoretical View* (Taylor and Francis, London, 2003), p. 159.
4. J. Mao, D. H. Wu, J. L. Peng, *et al.*, Phys. Rev. B **51**, 3316 (1995).
5. H. Srikanth, Z. Zhai, S. Sridhar, *et al.*, J. Phys. Chem. Solids **59**, 2105 (1998).
6. Yu. A. Nefyodov, M. R. Trunin, A. A. Zhohov, *et al.*, Phys. Rev. B **67**, 144504 (2003).
7. A. Hosseini, S. Kamal, D. A. Bonn, *et al.*, Phys. Rev. Lett. **81**, 1298 (1998).

8. T. Xiang, C. Panagapoulos, and J. R. Cooper, Int. J. Mod. Phys. B **12**, 1007 (1998).
9. Yu. A. Nefyodov and M. R. Trunin, Physica C (Amsterdam) (2003) (in press).
10. R. J. Radtke, V. N. Kostur, and K. Levin, Phys. Rev. B **53**, R522 (1996); R. J. Radtke and K. Levin, Physica C (Amsterdam) **250**, 282 (1995); R. J. Rojo and K. Levin, Phys. Rev. B **48**, 16861 (1993).
11. M. Turlakov and A. J. Legget, Phys. Rev. B **63**, 064518 (2001).
12. N. Kumar and A. M. Jayannavar, Phys. Rev. B **45**, 5001 (1992).
13. L. B. Ioffe, A. I. Larkin, A. A. Varlamov, *et al.*, Phys. Rev. B **47**, 8936 (1993).
14. M. J. Graf, D. Rainer, and J. A. Sauls, Phys. Rev. B **47**, 12089 (1993).
15. A. F. Ho and A. J. Schofield, cond-mat/0211675.
16. I. G. Lang and Yu. A. Firsov, Zh. Éksp. Teor. Fiz. **43**, 1843 (1962) [Sov. Phys. JETP **16**, 1301 (1962)]; Zh. Éksp. Teor. Fiz. **45**, 378 (1963) [Sov. Phys. JETP **18**, 262 (1963)].
17. T. Holstein, Ann. Phys. (N.Y.) **8**, 343 (1959).
18. T. Timusk and B. Statt, Rep. Prog. Phys. **62**, 61 (1999).

Translated by V. Sakun